

Durham E-Theses

*Analysis of the strong field approximation for
harmonic generation and multiphoton ionization in
intense ultrashort laser pulses*

Chirilă, Ciprian Constantin

How to cite:

Chirilă, Ciprian Constantin (2004) *Analysis of the strong field approximation for harmonic generation and multiphoton ionization in intense ultrashort laser pulses*, Durham theses, Durham University. Available at Durham E-Theses Online: <http://etheses.dur.ac.uk/10633/>

Use policy

The full-text may be used and/or reproduced, and given to third parties in any format or medium, without prior permission or charge, for personal research or study, educational, or not-for-profit purposes provided that:

- a full bibliographic reference is made to the original source
- a [link](#) is made to the metadata record in Durham E-Theses
- the full-text is not changed in any way

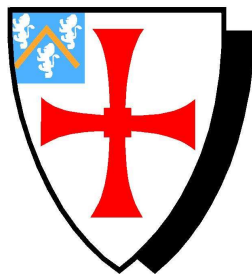
The full-text must not be sold in any format or medium without the formal permission of the copyright holders.

Please consult the [full Durham E-Theses policy](#) for further details.

**Analysis of the strong field
approximation
for harmonic generation and
multiphoton ionization
in intense ultrashort laser pulses**

Ciprian Constantin Chirilă

A thesis submitted in partial fulfilment
of the requirements for the degree of
Doctor of Philosophy



The University of Durham
Department of Physics
2004

Analysis of the strong field approximation for harmonic generation and multiphoton ionization in intense ultrashort laser pulses

Ciprian Constantin Chirilă

Abstract

We apply the strong field approximation (SFA) to the study of harmonic generation (HG) and above threshold ionization (ATI) in intense low-frequency laser fields. We review in a systematic way the SFA model from the literature to date, and fill in some gaps regarding its analytical and computational aspects. Special attention is devoted to the analysis of the saddle point method, which is widely used to calculate the highly oscillatory integrals describing the physical processes. Its accuracy is compared against the results from numerical integration; for the latter task, we propose two methods, which prove to be fast and reliable for all practical purposes. In the context of HG, we discuss non-dipole effects, using a non-dipole non-relativistic method. The use of a second, weaker laser pulse is shown to allow the emission enhancement of selected harmonics. We briefly discuss the importance of relativistic effects using the results of a fully relativistic calculation of Milošević *et al.*. In the context of ATI, quantitative comparisons are made with results obtained by integrating the exact static ionization rates over the pulse or, where possible, with *ab initio* results. Direct ionization in short pulses is extensively presented in the framework of a Coulomb-corrected version of the SFA, due to Krainov; interesting interference effects are shown to take place, in particular modulations in the angle-resolved ATI spectra depending strongly on the phase of the carrier. These modulations happen for pulses that are not too long, typically fewer than (9-10) optical cycles. As a consequence, the ATI peaks in the

angle-integrated spectra have a good resolution or are undistinguishable from the background, if the electric field component of the pulse is symmetrical or anti-symmetrical with respect to the pulse half duration, respectively. Partial conclusions are drawn regarding the applicability of the SFA to the study of the ionization process and possible ways to further improve the model are suggested.

*Dedicated to Professor Viorica Florescu,
for helping me with the first steps*

Declaration

I confirm that no part of the material offered has previously been submitted by me for a degree in this or in any other University. If material has been generated through joint work, my independent contribution has been clearly indicated. In all other cases material from the work of others has been acknowledged and quotations and paraphrases suitably indicated.

Ciprian Constantin Chirilă
Durham, 8th September 2004

The copyright of this thesis rests with the author. No quotation from it should be published without their written consent and information derived from it should be acknowledged.

Acknowledgements

I thank my supervisors, Niels Kylstra and Robert Potvliege for the time they invested in me and for their tuition. In particular, I thank Niels for supervision during my first year and for his constant encouragements. Also, I am grateful for his substantial help with interpreting some of the results for harmonic generation. To Robert, I am indebted for his patience, especially over the past two years, and for his careful reading and countless discussions over the content of this thesis. Many times they led to new interesting things appearing in places I never suspected. Moreover, some of his inspired ideas, like the use of a second weak field for harmonic generation, resulted in a whole chapter of this work.

Special thanks to Ifan Hughes for my unforgettable first year report discussion and numerous useful hints for writing-up. Not less appreciated is his humor, that went well with the coffee breaks during rainy days. Big thanks go to Charles Adams and David Flower who are also ‘responsible’ for creating a nice atmosphere in the AtMol group. Especially, I would like to thank Prof. David Flower for his prompt support on all occasions.

Furthermore, some interesting and animated games of ‘Risk’ were due to Nick Proukakis, whose friendship I enjoyed. As well, I want to thank all the students in the group for sharing this experience with me and for their friendship outside the office. Especially, to Nick Parker for being an excellent officemate all the way to the third year and for his good knowledge of English I sometimes took advantage of. I couldn’t finish without mentioning G’Dave – rumor has it that ‘G’ stands for ‘ginger’; I have never believed that–, and Griff, for his football dedication. Thanks to James, one of the best organizers of top weekends outside Durham, for sharing together some beautiful English sights.

To my friends at home, Claudiu and Radiana Gura, for their support with my travels through Bucharest and friendship, and to my old friend Cristi for always being himself.

Last, and far from the least, to my family.

Contents

Abstract	1
Declaration	4
Acknowledgements	5
List of Figures	9
List of Tables	16
1 Introduction	18
2 Harmonic generation. Non-dipole effects	24
2.1 Outline	24
2.2 Theoretical approach	25
2.3 Saddle-point integration	27
2.3.1 Exact saddle times	28
2.3.2 Approximate saddle times	30
2.4 Non-dipole effects in photon emission for stationary fields	35
2.5 Importance of relativistic effects	37
2.6 Harmonic generation in short pulses	39
2.7 Conclusions	41
3 ‘Undoing’ the non-dipole effects in harmonic generation	43
3.1 Outline	43
3.2 Adding a second electric field	44
3.3 Attosecond pulse generation	47
3.4 How to correct the non-dipole effects for a given harmonic order	49
3.5 Conclusions	52
4 Above threshold ionization in atomic systems	54
4.1 Outline	54
4.1.1 Historical overview	54
4.1.2 Theoretical methods	56

4.2	Direct ionization in a stationary field	58
4.2.1	The quantum-mechanical description	58
4.2.2	The classical model of ionization	61
4.2.3	Interferences of direct electrons	63
4.3	Rescattering	65
4.3.1	The classical theory	65
4.3.2	The quantum-mechanical description	66
4.3.3	Saddle point method. Quantum orbits	68
4.3.4	The saddle point uniform approximation	72
4.3.5	Direct- and rescattered-electrons interference	76
4.4	Conclusions	76
5	Strong Field Approximation (SFA)	78
5.1	Outline	78
5.2	The direct and re-scattering ionization amplitudes	80
5.3	Direct ionization amplitude	83
5.3.1	The length gauge direct amplitude	84
5.3.2	The velocity gauge direct amplitude	85
5.3.3	The Krainov Coulomb-corrected ionization amplitude	86
5.4	The case of the stationary field	88
5.4.1	Linearly polarized radiation	88
5.4.2	Circularly polarized radiation	90
5.5	Analytic results for the direct ionization (velocity gauge)	92
5.5.1	Elliptic polarization	92
5.5.2	Linear polarization	94
5.5.3	Circular polarization	94
5.6	Analytic results for the direct ionization (length gauge)	94
5.7	A modified velocity gauge amplitude	96
5.8	Study case: ionization of He^+ in a stationary field	100
5.9	Conclusions	102
6	Direct ionization in short pulses	104
6.1	Outline	104
6.2	Pulse form and classical energy cutoffs	105
6.3	Definitions of SFA angular and energy distributions	108
6.4	The accuracy of the saddle point method	110
6.5	Total ionization probabilities	113
6.6	Differential ionization probabilities	115
6.7	Mathematical analysis	119
6.7.1	The case of symmetrical electric field	121
6.7.2	The case of anti-symmetrical electric field	124
6.8	Influence of pulse parameters on direct ionization	126
6.8.1	Influence of the field phase	126

6.8.2	Influence of the intensity	127
6.8.3	Influence of pulse duration	129
6.8.4	Influence of the binding energy and pulse shape	131
6.9	Field-phase dependence of emission asymmetry	134
6.10	Comparison with <i>ab initio</i> results	136
6.11	Conclusions	141
7	Conclusions	144
A	The dipole Gordon-Volkov solution	147
B	Non-dipole non-relativistic Volkov solution	150
C	Singular asymptotics	152
D	Coulomb corrected ionization rates	154
D.1	Tunnelling ionization by linearly polarized radiation	154
D.2	Tunnelling ionization by circularly polarized radiation	158
E	Computational methods	161
E.1	Statement of the problem	161
E.2	Saddle point method	162
E.2.1	General introduction	162
E.2.2	Boundary terms	163
E.2.3	Comparison with exact results	166
E.3	Finding the saddle points	167
E.3.1	General considerations	167
E.3.2	Approximate saddle points	168
E.3.3	Exact saddle points	170
E.4	Improved saddle point method - the high intensity case	173
E.5	Numerical integration	176
E.5.1	Method I - using the saddle points	176
E.5.2	Method II - integration along real axis	178
E.6	Conclusions	180
	Bibliography	189

List of Figures

2.1	The saddle point trajectories [$\omega t_s(t)$ from Eq. (2.19)] in the complex plane for a He^+ ion irradiated by a two-cycle \sin^2 laser field, at 800 nm and peak electric field $E_0 = 0.4$ a.u. The full circles are the initial positions of the saddles at $t = 0$. The red curves represent the saddles contributing to the dipole moment $\mathbf{d}(t)$: $\text{Re}[t_s(t)] < \text{Re}(t)$	30
2.2	The magnitude squared of the Fourier transform of the dipole acceleration (in a.u.) as a function of the photon energy (in units of $\hbar\omega$), for a He^+ ion interacting with a two-cycle laser field of wavelength 800 nm. The peak electric field is $E_0 = 0.4$ a.u. and the photon emission is in the polarization direction. The black curve shows the exact results [numerical integration of Eq. (2.17)] and the red curve the results of the saddle point integration [Eq. (2.20)].	31
2.3	Photon emission in the polarization direction for a He^+ ion, irradiated by a two-cycle laser pulse, at 800 nm. The black curve shows the result of the exact saddle point integration and the red curve the approximated saddle integration [Eq. (2.32)].	34
2.4	The magnitude squared of the Fourier transform of the dipole acceleration (in a.u.) as a function of the photon energy (in units of $\hbar\omega$), for a Ne^{6+} ion interacting with a stationary laser field of wavelength 800 nm. Spectra for the emission of photons polarized along the laser polarization direction obtained in the dipole approximation ($\text{D}\epsilon$) and in the non-dipole non-relativistic approximation ($\text{ND}\epsilon$) are shown, as well as the non-dipole non-relativistic spectra for photon emission polarized along the laser propagation direction (NDk).	36

- 2.5 The magnitude squared of the Fourier transform of the dipole acceleration (in a.u.) as a function of the photon energy (in units of $\hbar\omega$). Spectra for a Ne^{6+} ion obtained in the dipole and non-dipole non-relativistic approximations are shown for the emission of photons polarized along the laser polarization direction. The ion is irradiated by a stationary laser field of peak intensities 0.7 and $1.4 \times 10^{17} \text{ W cm}^{-2}$, as indicated, and wavelength 1054 nm. The non-dipole results are compared with the relativistic results (R) of Milošević, Hu and Becker [1]. 38
- 2.6 The magnitude squared of the Fourier transform of the dipole acceleration (in a.u.) as a function of the photon energy (in units of $\hbar\omega$). Spectra for a Be^{3+} ion obtained in the dipole and non-dipole approximations are shown for the emission of photons polarized along the laser polarization direction ($\text{D}\epsilon$, $\text{ND}\epsilon$) for a 3-cycle pulse ($n=3$), a 4-cycle pulse ($n=4$) and a stationary field. The peak intensity is $3.6 \times 10^{17} \text{ W cm}^{-2}$ and $\lambda = 800 \text{ nm}$. 40
- 3.1 The configuration of the strong and weak laser pulses. 44
- 3.2 The magnitude squared of the Fourier transform of the dipole acceleration, in a.u., of Ne^{6+} as a function of the photon energy (in units of $\hbar\omega$). The laser pulse duration is two-cycles, with peak intensity $3.6 \times 10^{17} \text{ W cm}^{-2}$ and wavelength 800 nm. Dipole ($\text{D}\epsilon$) and non-dipole ($\text{ND}\epsilon$) spectra are shown. In plots (b) and (c), the non-dipole results are for the case in which the ion interacts with a second, weaker laser pulse polarized along the propagation direction of the intense pulse (see text). In plot (b), the time delay ($\tau_w = 62 \text{ a.u.}$) and intensity ($I_w = 4.8 \times 10^{15} \text{ W cm}^{-2}$) of the second pulse were chosen such that photon emission in the neighborhood of the 7500th harmonic is enhanced, while in plot (c), $\tau_w = -80 \text{ a.u.}$ and $I_w = 3.6 \times 10^{15} \text{ W cm}^{-2}$, leading to the enhancement of emission around the 30 000th harmonic. 46
- 3.3 The magnitude squared of the frequency-resolved dipole acceleration for photon emission centered about the 2500th harmonic of the driving field by a single Ne^{6+} ion interacting with a four-cycle Ti:Sapphire pulse of $3.6 \times 10^{17} \text{ W cm}^{-2}$ peak intensity. Shown are results obtained in the dipole approximation (a) and in the non-dipole non-relativistic approximation (b, c). Plot (c) shows the enhancement by a second laser pulse of photon emission at 3.4 laser periods. The peak intensity of the second pulse, I_w , is $2.2 \times 10^{14} \text{ W cm}^{-2}$ and the delay, τ_w , is 30.8 a.u. 48

3.4	The magnitude squared of the Fourier transform of the dipole acceleration of a single Ne^{6+} ion interacting with a four-cycle Ti:Sapphire pulse of $3.6 \times 10^{17} \text{ W cm}^{-2}$ peak intensity. Shown are results obtained in the non-dipole non-relativistic approximation, with the upper curve illustrating the enhancement of photon emission around $\Omega/\omega = 2500$ when the ion interacts with a second, weaker laser pulse having the same peak intensity and delay as in Fig. 3.3. The high energy part of the spectrum is not shown.	49
3.5	The return time t_r as a function of the detachment time t_i for a two-cycle \sin^2 laser field, with wavelength of 800 nm and intensity of $3.6 \times 10^{17} \text{ W/cm}^2$. The dashed curve shows the absolute value of the electric field during the pulse (in arbitrary units).	51
3.6	The initial speed [Eq. (3.4)] for two different field strengths, as a function of delay with respect to the driving field. From the first panel, one can see that the minimum weak field strength for the parameters chosen here (see text) can be as small as 0.15 a.u. The second panel shows results for the field amplitude chosen in Section 3.2 (the arrow points to the value of the delay chosen there); the delay can be chosen among many values for this case.	52
4.1	(a) Measured and (b) calculated photoelectron spectrum in argon for 800 nm, 120 fs pulses at the intensities given in TW/cm^2 in the figure ($10U_p = 39 \text{ eV}$). From Nandor <i>et al.</i> [2].	57
4.2	The saddle point trajectories in the complex plane for a He^+ ion irradiated by a stationary pulse with intensity $I = 10^{16} \text{ W cm}^{-2}$ and wavelength of 800 nm. The electron is emitted along the polarization axis. The dashed curve is the profile of the vector potential during one optical cycle. The circles represent the positions of the two saddles for $p=0$ and the end points of the trajectories correspond to $p = A_0$	60
4.3	The graphical solution for the ‘birth’ times $\{t_{01}, t_{02}\}$ for a stationary field, satisfying $p_{\parallel}/A_0 + \cos(\omega t) = 0$ with $p_{\parallel} = -0.5A_0$	61
4.4	Schematic picture of the origin of interference in electron emission from two laser-induced sources. The indices (1) and (2) correspond to the two positions as in Eq. (4.10).	64
4.5	The vertical curves satisfy (4.23a) with $I_p = 0$ and the horizontal ones (4.23b) ($\mathbf{k} \neq \mathbf{p}$). Therefore, the intersection points give the solutions for the trajectories corresponding to final drift momentum $\mathbf{p} = 0$ (left panel) and $\mathbf{p}^2/2 = 5.8U_p$ (right panel, with \mathbf{p} in the polarization direction).	70

4.6	Saddle points for scattering along the polarization axis for a Keldysh parameter $\gamma = 1.11$ and $\mathbf{p} = 0$. The labels refer to the fact that the pairs (1,2) and (9,10) are ordered as a function of the increasing travel time $t - t'$. The circles correspond to $p = 0$ and the trajectories end at $\mathbf{p}^2/2 = 10U_p$	71
4.7	Direct and rescattering amplitudes for a zero-range binding potential with $U_p/\omega = 3.58$, at 800 nm and a ground state energy $I_p = 0.5$. The spectrum is in the laser polarization direction and the pulse has a \sin^2 envelope with zero absolute phase. The circles correspond to the ATI peaks. For the rescattering plateau, only the first five pairs of saddle points have been included.	74
4.8	Scattering contributions for the first five saddle point pairs. The physical parameters are the same as in Fig. 4.7. The contributions have been displaced for visual convenience. The red curve shows the contribution of all the five pairs.	75
5.1	Graph of the modulating factor $\left \frac{\sin(Nx/2)}{\sin(x/2)} \right $, with $N = 20$	89
5.2	Rates of ionization of a hydrogen atom by a linearly polarized field at $\lambda=1064$ nm vs laser intensity. The (LG) and (VG) curves show the results predicted by the SFA model in the length gauge and velocity gauge. The other curves show the Floquet results (the red curve and filled circles), the A Becker <i>et al.</i> corrected version and the predictions of the Krainov Coulomb-corrected rate. The upper scale gives the Keldysh adiabaticity parameter.	97
5.3	Log-Log plot of the ionization rates for He^+ in a linearly polarized stationary field. The wavelength is 800 nm.	100
5.4	Same parameters as in Fig 5.3. The Krainov Coulomb corrected rates are shown for 800 nm and for 1064 nm.	101
6.1	Left panel: a 4-cycle \sin^2 pulse (black curve) and a sech pulse (red curve) with the same FWHM (in intensity). The phase is $\phi = \pi/2$. The right panel shows the same, only for identical FWHM in amplitude.	106
6.2	The cutoffs for the return (left panel) and rescattering (right panel) kinetic energy for a n -cycle \sin^2 pulse, with $A(t) \propto \sin(\omega t) \sin^2(\omega t/2n)$	107
6.3	The phase dependence of the maximal return (left panel) and rescattering (right panel) kinetic energy for a 4-cycle \sin^2 pulse, with $A(t) \propto \sin(\omega t + \phi) \sin^2(\omega t/8)$	109

- 6.4 Angle-resolved [Eq. (6.3)] ATI energy spectra for electron emission from He^+ along the polarization axis for an electric field amplitude $E_0 = 0.2$ a.u. (left panel) and $E_0 = 0.3$ a.u. (right panel). The wavelength is 800 nm and the pulse duration is four optical cycles with $\phi = 0$. The red curves show the exact integration result from which the first order boundary term (BT) has been subtracted and the black curves show the saddle point result. 112
- 6.5 Angular distributions in He^+ for electron energy of $0.1U_p$. The pulse parameters are the same as in Fig. 6.4. The red curves show the exact integration result from which the first order boundary term (BT) has been subtracted and the black curves show the saddle point result. 113
- 6.6 Total ionization probability for a He^+ ion irradiated by a four-cycle \sin^2 pulse, with $\phi = 0$. The results are given as a function of the peak intensity and originate for the usual and KSFA model. The other two estimates were calculated using the exact rate of ionization in a static electric field and the Landau and Lifshitz static tunneling rate, respectively. 115
- 6.7 Left panel: angle-resolved ATI spectra for different emission angles θ with respect to the polarization direction. Right panel: angle-integrated ATI spectra. The pulse is with a \sin^2 envelope, encompassing four optical cycles, with 800 nm wavelength. The electric field amplitude is $E_0 = 0.4$ a.u. The ion is He^+ 116
- 6.8 Left panel: angle-resolved ATI spectra for different emission angles θ with respect to the polarization direction. Right panel: angle-integrated ATI spectra. The parameters are the same as in Fig. 6.7, only the field phase is changed: $\phi = \pi/2$ 117
- 6.9 The differential ionization probability for constant electron energy as a function of the emission angle and the energy-integrated probability for He^+ irradiated by a four-cycle \sin^2 pulse with peak electric field $E_0 = 0.2$ a.u. Left panel: the field phase is $\phi = 0$, right panel: $\phi = \pi/4$. The wavelength is 800 nm. (The ponderomotive energy is $U_p = 0.77$ a.u.) 118
- 6.10 The case of a symmetrical electric field. 121
- 6.11 Angle-resolved ATI energy spectra at different emission angles for a He^+ irradiated by a \sin^2 pulse with $E_0 = 0.4$ a.u. and field phase $\phi = 0$. The wavelength is 800 nm. Only the contribution of the symmetrical pair of saddles is shown. The filled circles represent the predicted LATI peaks, from Eq. (6.9). 123

6.12	The saddle point contributions to the ionization probability of He^+ , for a 4-cycle \sin^2 pulse with symmetrical electric field. The pulse has 800 nm wavelength and the peak electric field is $E_0 = 0.4$ a.u.	124
6.13	The case of an anti-symmetrical electric field.	125
6.14	Angle-resolved LATI energy spectra. Only the contribution of the first pair is shown. The parameters are the same as in Fig. 6.11, only the electric field is anti-symmetrical: $\phi = \pi/2$. The filled circles are the predicted LATI peaks, from Eq. (6.10). The emission is along the polarization direction (left panel) and at an angle $\theta = \pi/10$ with respect to the polarization axis (right panel).	126
6.15	The angle-integrated ionization probability in He^+ for the same pulse as in Fig. 6.12, only for various field phases.	127
6.16	Angle-integrated ionization probability of He^+ for increasing intensity. The electric field is symmetrical with respect to the middle of the pulse. The rest of the pulse parameters are the same as in Fig. 6.18.	128
6.17	Angle-integrated ionization probability of He^+ for increasing intensity. The electric field has the phase $\phi = \pi/4$. The rest of the pulse parameters are the same as in Fig. 6.18.	128
6.18	Angle-integrated ionization probability per pulse duration in He^+ irradiated by a 4-cycle \sin^2 pulse with $E_0 = 0.2$ a.u. and $\phi = 0$	130
6.19	Angle-integrated ionization probability in He^+ for different duration \sin^2 pulses with $E_0 = 0.3$ a.u. and phase $\phi = 0.23$ rad. The rest of the parameters are the same as in Fig. 6.18.	130
6.20	Left panel: angle-integrated ionization probabilities for He^+ in a 800 nm, 4-cycle \sin^2 pulse and a sech pulse with identical FWHM (in amplitude). The peak electric field is $E_0 = 0.4$ a.u. The phase is $\phi = 0$. Right panel: the probability for different pulse phases for the sech pulse.	132
6.21	The same as in Fig. 6.20, but for a Gaussian pulse.	132
6.22	The same as in Fig. 6.20, but for helium, at intensity $I = 1 \times 10^{15}$ W/cm ² . (The Keldysh parameter $\gamma = 0.45$.)	133
6.23	The asymmetry for direct ionization in He^+ for a peak electric field $E_0 = 0.4$ a.u., at a wavelength of 800 nm. The field is a \sin^2 field, encompassing four optical cycles. The two curves show the KSFA results and the prediction of a simple model based on the exact ionization rates in a static electric field. . . .	134

- 6.24 The ionization probability for an ejection angle $\theta = 10^\circ$ with respect to the polarization direction for a He^+ ion irradiated by a two-cycle \sin^2 pulse, with $\phi = \pi/2$. The intensity is 10^{16} W/cm^2 and the carrier wavelength is 400 nm. The red curve gives the *ab initio* results and the black curve the KSFA results. 137
- 6.25 The ionization probability for an ejection angle $\theta = 10^\circ$ with respect to the polarization direction for a He^+ ion irradiated by a four-cycle \sin^2 pulse, with $\phi = \pi/2$. The intensity is 10^{16} W/cm^2 and the carrier wavelength is 400 nm. The red curve gives the *ab initio* results and the black curve the KSFA results. 138
- 6.26 Emission probability in hydrogen, for ejection of the electron along the polarization axis with momentum p_z and in the perpendicular plane with momentum p_n . The laser has a peak intensity of 1.3×10^{14} W/cm^2 , eight optical cycles and the wavelength is 800 nm. The electric field is symmetrical with respect to the middle of the pulse. The *ab initio* result is displayed in the upper panel [3], while the lower one shows the Coulomb-corrected SFA result. White lines in the top diagram are the predictions of the SFA in the velocity gauge [4]. 140
- 6.27 Angle-integrated ATI spectrum of He^+ irradiated by a 400 nm, 4-cycle \sin^2 laser pulse, with peak intensity of 1×10^{16} W/cm^2 . The field phase is $\phi = 0$. The *ab initio* result is compared to the KSFA result. 141
- 6.28 Comparison between the *ab initio* result and the KSFA result. The pulse parameters are the same as in Fig. 6.27, only the electric field is asymmetrical: $\phi = \pi/2$ 142
- E.1 Angle-resolved ATI energy spectrum generated by a 2-cycle \sin^2 pulse (left panel) and a 4-cycle one (right panel) with zero absolute phase, $\lambda=800$ nm and intensity $I = 5 \times 10^{15}$ W/cm^2 in He^+ . The electron is emitted along the laser polarization direction. Panel (a): the smooth curve (black) represents the saddle point result and the oscillating curve (red) the exact calculation from which the first order boundary term contribution has been subtracted. Panel (b): the two results are almost indistinguishable on the scale of the graph. 165
- E.2 Angle-resolved ATI energy spectrum calculated in the length gauge, generated by a 4-cycle \sin^2 pulse with zero absolute phase, $\lambda=800$ nm and intensity $I = 6 \times 10^{13}$ W/cm^2 in krypton ($I_p = 14$ eV). The electron is emitted along the laser polarization direction. The lower (black) curve shows the saddle results and the upper (red) curve shows the exact results. 167

E.3	Angle-resolved ATI energy spectrum calculated by using the Krainov Coulomb corrected ionization amplitude, generated by a 4-cycle \sin^2 pulse with zero absolute phase, $\lambda=800$ nm and intensity $I = 5.6 \times 10^{15}$ W/cm ² in He ⁺ . The electron is emitted along the laser polarization direction. The upper (black) curve shows the saddle results and the lower (red) curve shows the saddle simplified version results.	171
E.4	Some of the saddle points for the case of a He ⁺ ion irradiated by a 4-cycle laser, at an intensity of 10^{16} W/cm ² and wavelength 800 nm. The laser pulse is described by a \sin^2 envelope with zero absolute phase.	172
E.5	Exponential decay (gaussian) and gaussian with cubic oscillatory factor [see (E.18)].	174
E.6	The relative error of the differential ionization probability for emission along the polarization direction, in the case of a He ⁺ ion irradiated by a 800 nm, 4-cycle laser pulse, at an intensity of 8.8×10^{15} W/cm ² and zero absolute phase. The black curve shows the error made by using the usual saddle method and the red curve shows the resulting error when using the improved saddle method.	175
E.7	The deformation of the integration contour in the complex plane to avoid strong oscillatory behaviour along the real axis. The full curves represent the exponential decay of the integrand in the vicinity of the saddle points.	177
E.8	The integrand behaviour in the complex plane (lower panel) and along the real axis (upper panel). The letters correspond to the integration path in Fig. E.7. For simplicity, only a part of the real axis has been represented. The inset in the lower panel shows the integrand along the beginning of the BC path.	178

List of Tables

6.1	Cutoffs for return and rescattering energy for \sin^2 pulses with different number of cycles (see Fig. 6.2).	108
-----	--	-----

Chapter 1

Introduction

The area of atom-light interaction is of growing importance mainly due to unprecedented advances in laser technology and detection systems. Nowadays, powerful laser systems are available as table top devices, allowing for the experiments to be performed in a simpler manner than in the past. More precise detection systems have made it possible to observe energy-resolved spectra of ionized electrons with higher accuracy, leading, for example, to the observation of the re-scattering plateau in above threshold ionization. Also, a large number of known phenomena can be studied in entirely new regimes, using intense few-cycle laser pulses [5–8]. Such pulses can encompass as few as two or three optical cycles and have a peak intensity around or exceeding 10^{14} W/cm². This new working regime led to new features of the known processes to be discovered, as well as to new phenomena. The high laser intensity requires the development of new mathematical and computational tools, as the perturbational techniques break down. New physical models allow for a better understanding of most of the experimental results: the well-known Simpleman’s model gives a simple interpretation of a large number of atomic processes (such as above threshold ionization, harmonic generation, recollision-induced multiple ionization, . . .) in terms of classical trajectories of the free electron in the external laser field in conjunction with a quantal treatment of the tunneling through the potential barrier formed by the Coulomb potential and the external field. The

Simpleman's model forms the basis of our present understanding of processes occurring in low-frequency laser fields. It is remarkable that processes that appear to be complex at first sight, allow for an accurate qualitative description with simple, intuitive semi-classical models.

For example, atoms and ions interacting with intense infrared laser pulses emit high order harmonics of the driving field in the form of coherent attosecond pulses [5, 9–12]. The process can be understood within the Simpleman's model, whereby electrons are detached from the atomic core by quasi-static tunneling ionization, oscillate in the field and return to the core where they radiatively recombine [13–17]. A quantum version of this model has formed the basis of a vast number of theoretical investigations of high-order harmonic generation [16–18], and has been used successfully to analyze experiments (see, e.g., [19]). This theory relies on the strong field approximation (SFA), which assumes that the interaction of the electron with the core is much weaker than the interaction with the driving field, so the former can be neglected.

Nearly all the theoretical work to date on high-order harmonic generation in low frequency fields assumes the dipole approximation. At the Ti:Sapphire wavelength, the dipole approximation is expected to remain valid up to intensities of about 5×10^{16} to 1×10^{17} W/cm² (depending on the system, as will be seen). In the recent theoretical investigations of photon emission by ions interacting with intense near infrared laser pulses [1, 20–24], it was established the existence of a 'non-dipole non-relativistic' dynamical regime, in which the effect of the magnetic field component of the laser is too large for the dipole approximation to apply, but not so large that a relativistic description would become necessary. Only a few fully quantum calculations, all based on the SFA, have addressed the role of the magnetic drift in this context. Expressions for the dipole moment of an atom or ion in the non-dipole non-relativistic regime have been developed by Walser *et al.* [21] and, in another form, by Kylstra, Potvliege and Joachain [22, 25], and applied to photon emission in ultrashort pulses.

Unlike an infinitely extended monochromatic plane wave which can be fully characterized by its frequency and intensity, a finite pulse requires two additional parameters: its duration and the carrier-envelope relative phase, also referred to as the ‘absolute phase’, that is the relative phase between the maximum of the envelope and the closest peak of the carrier wave. The shape of the pulse crucially depends on these parameters and so do the physical processes they may induce. Recently, few-cycle pulses with stable absolute phase have been obtained for the first time [26], raising the question of finding a reliable way to measure the phase. The fact that the atomic ionization depends on the absolute phase was pointed out in [27, 28] and the measurement of the angular distribution of electrons was proposed as a method to determine the absolute phase in [29, 30]. Another important feature of ionization is the left-right asymmetry of above-threshold ionization (ATI) yields, used to obtain the first experimental evidence of absolute-phase phenomena in a ‘stereo-ATI’ experiment [31] with circularly polarized few-cycle laser pulses. Two detectors were used, positioned opposite in a plane perpendicular to the propagation direction of the laser beam. Depending on the value of the absolute phase, one detector registers more electrons than the other. The theoretical analysis of this experiment was presented in [32, 33]. The sensitivity of high-order ATI (HATI) is discussed in the paper of [34].

In this work, we study some aspects of harmonic generation and above threshold ionization in atomic systems, within the strong field approximation. In Chapter 2 we analyze harmonic generation using the non-dipole approach of Refs. [22, 25]. The saddle point analysis is applied to this model with the result of extending the Simpleman’s model to the non-dipole regime. The interpretation of the results becomes more transparent in terms of the classical electron trajectories, taking into account the effect of the magnetic field component of the laser pulse. General interference features of the so-called plateaus in the harmonic generation spectra are discussed and comparison is made between photon emission in short pulses and in stationary fields. In addition, the relevance of the relativistic effects is presented, in connection to the recent results

of Milošević, Hu and Becker [1, 32] who gave a relativistic formulation of harmonic generation in stationary fields, based on the Klein-Gordon equation. Chapter 3 presents a possible way to correct the non-dipole effects for a given harmonic order, by using a second, much weaker pulse whose role is to cancel the drift of the electron wavepacket due to the magnetic field, as it returns to the atomic core. The displacement of the wavepacket can greatly reduce the efficiency of the recombination process and consequently of the harmonic emission. Based on the saddle point approach, a simple and efficient computational method of the harmonic spectra is presented and its accuracy is proven to be very reliable when compared to the direct integration results.

In the context of the strong field approximation applied to the study of above threshold ionization, Chapter 4 gives a review of the relevant literature, presented in a compact way with details of less-discussed, more technical issues not developed in the original articles. We give a clear connection between the Keldysh-Faisal-Reiss approach to ionization, the saddle point method and the classical Simpleman's model. The uniform approximation for the saddle point method, important in the calculation of the rescattering plateau, is explained in detail and new ways to solve the equations for finding the saddle times in a straightforward manner are proposed.

A systematic presentation of up to date theoretical results for the strong field approximation is lacking from the current literature, as well as the analysis of the agreement, under general pulse characteristics, between SFA and *ab initio* results (apart from the case of negative ions, where there is good general agreement between SFA and experimental ATI spectra for low-energy ejected electrons: see, e.g., the case of H^- in Ref. [35] or F^- in Ref. [36]). Chapter 5 gives an extensive compilation of the relevant SFA formulae for direct ionization, in both the length and the velocity gauge. It completes the list of analytical expressions for direct ionization in the frame of the SFA model, encountered in the literature, and extends some of the analytical techniques used to calculate them to more general cases.

A Coulomb-corrected version of the SFA, as given by Krainov (KSFA), is analyzed together with the SFA results and compared to the quasi-static results obtained by integrating the exact ionization rates in a static field: it is shown that the agreement for the KSFA is much better than for the SFA formulation. The detailed calculation for the low-frequency limit of KSFA is presented in Appendix D, with the misprints from the original article corrected; it shows that in the low-frequency limit, the KSFA result reduces to the ADK formula [37], for both linear and circular polarization.

In Chapter 6 we apply the KSFA model to calculate direct ionization ATI spectra for short laser pulses. We give a simple analytical analysis of the electron interference patterns, based on the saddle point method and show the influence of different pulse parameters (such as pulse duration, intensity and phase) on the low-order ATI spectrum (LATI). The relevance of pulse phase effects is emphasized in connection to the pulse temporal length. The accuracy of the saddle point method is analyzed in detail and a new concept of ‘boundary terms’ is introduced, related to the fact that the pulse is finite in time, unlike the case of the stationary field. Considering the boundary terms is shown to be essential to obtaining correct physical results from the numerical integration of the ionization amplitudes. Appendix E presents in detail the calculation of the boundary terms, along with a more technical discussion of the computational aspects for the saddle point method. It is shown that for the laser parameters we use, the saddle point integration gives results in excellent agreement with the numerical integration results. We develop two simple methods to calculate by direct integration the oscillatory integrals giving the ionization amplitudes: one method is based on the use of the saddle points of the integrand and the other is an implementation of a method from the numerical literature. The latter was especially designed for oscillatory integrands and we adapted it successfully for our calculations, in order to reduce the computational time. The efficiency of such methods is essential in the study of a large group of atomic processes, including harmonic generation and above threshold ionization.

Also, total ionization probabilities in a short laser pulse, as given by KSFA, are compared to the results obtained by integrating the exact static ionization rates along the pulse; good agreement is found, in contrast to the results from the familiar SFA model (without the tunneling correction). In the last part of the chapter, we compare the predictions of the KSFA model with *ab initio* results in the form of a probability density plot in the momentum space. The main differences are discussed.

Conclusions and suggested further developments of the theory we employed in this work are given in Chapter 7.

Part of the results in this thesis were published in the following papers:

- *Nondipole effects in photon emission by laser-driven ions*, C C Chirilă, N J Kylstra, R M Potvliege and C J Joachain, Phys. Rev. A **66**(6), 063411 (2002).
- *Three-step processes with relativistic ions*, C C Chirilă, C J Joachain, N J Kylstra and R M Potvliege, Las. Phys. **14**(2), 190 (2004).

Chapter 2

Harmonic generation. Non-dipole effects

2.1 Outline

In the present chapter, we give a detailed account of the non-dipole SFA sketched in Ref. [22] and relate it to the theory of Walser *et al.* [21]. We also assess the importance of the relativistic effects neglected here by comparing with results obtained by Milošević, Hu and Becker [1]. We consider, in particular, the emission of photons by isolated He^+ , Be^{3+} and Ne^{6+} ions exposed to strong near-infrared pulses. Only multi-charged ions can withstand the intensities at which the non-dipole effects play a role; neutral species would ionize immediately. The importance of the non-dipole effects is investigated by comparing the non-dipole non-relativistic photon emission spectra with dipole spectra for long pulses (represented by stationary fields) as well as for few-cycle pulses. The numerical results are interpreted with the help of the recollision model, generalized to the non-dipole case. The trajectories we consider are real and obey the classical equations of motion. This approach complements the description of the electron's dynamics in terms of complex trajectories discussed in Ref. [1]; the two approaches lead to essentially the same physical picture. Unless otherwise indicated, atomic units are used.

2.2 Theoretical approach

This section presents the non-dipole approach developed in Ref. [22]. We assume that the vector potential describing the laser field can be written as

$$\mathbf{A}(\eta) = \hat{\boldsymbol{\epsilon}} (E_0/\omega) f(\eta) \sin(\eta), \quad (2.1)$$

with $\eta = \omega(t - \hat{\mathbf{k}} \cdot \mathbf{r}/c)$. The field has carrier wavelength $\lambda = 2\pi c/\omega$, field strength E_0 , is linearly polarized with polarization vector $\hat{\boldsymbol{\epsilon}}$ and propagates in the direction $\hat{\mathbf{k}}$. The function $f(\eta)$ describes the temporal profile of the pulse; $f(\eta) \equiv 1$ for a stationary field.

The influence of the magnetic field component of the laser on the electron dynamics can be accounted for in the long wavelength and non-relativistic regime considered here by expanding the vector potential to first order in $1/c$. Assuming the atom to be initially located at the origin leads to

$$\mathbf{A}(\eta) \simeq \mathbf{A}(\omega t) + \frac{1}{c} (\hat{\mathbf{k}} \cdot \mathbf{r}) \mathbf{E}(\omega t), \quad (2.2)$$

where $\mathbf{E}(\omega t) = -(d/dt)\mathbf{A}(\omega t) = -\hat{\boldsymbol{\epsilon}}(d/dt)A(\omega t) = \hat{\boldsymbol{\epsilon}}E(\omega t)$. The time-dependent Schrödinger equation

$$i \frac{\partial}{\partial t} \Psi(\mathbf{r}, t) = \left(\frac{1}{2} [-i\nabla + \mathbf{A}(\omega t)]^2 + \frac{1}{c} (\hat{\mathbf{k}} \cdot \mathbf{r}) [-i\nabla + \mathbf{A}(\omega t)] \cdot \mathbf{E}(\omega t) + V(r) \right) \Psi(\mathbf{r}, t), \quad (2.3)$$

is exact up to order $1/c$ in the atom-field interaction. The spin of the electron is neglected. The potential $V(r)$ describes the interaction of the electron with the ionic core. There are two non-dipole terms in the Hamiltonian: the first one, in $\nabla \cdot \mathbf{E}(\omega t)$, gives rise to electric quadrupole and magnetic dipole transitions. The second one, in $\mathbf{A}(\omega t) \cdot \mathbf{E}(\omega t)$, contributes to the drift in the propagation direction induced by the magnetic field component of the incident beam and has a large influence on the emission of photons by ions at high laser intensities.

At low frequencies, it is appropriate to transform the time-dependent Schrödinger

equation to the length gauge, with the result

$$i \frac{\partial}{\partial t} \Psi_L(\mathbf{r}, t) = \left(-\frac{1}{2} \nabla^2 + \left[\mathbf{r} - \frac{i}{c} (\hat{\mathbf{k}} \cdot \mathbf{r}) \nabla \right] \cdot \mathbf{E}(\omega t) + V(r) \right) \Psi_L(\mathbf{r}, t), \quad (2.4)$$

where $\Psi_L(\mathbf{r}, t) = \exp[i\mathbf{A}(\omega t) \cdot \mathbf{r}] \Psi(\mathbf{r}, t)$. By introducing the retarded Green's function associated with the Hamiltonian of Eq. (2.4), the wave function $\Psi_L(\mathbf{r}, t)$ can be obtained as the solution of a time-dependent Lippmann-Schwinger equation. In the SFA approach of Lewenstein and co-workers [9, 16], this Green's function is replaced by the Volkov Green's function associated with the Hamiltonian that describes a free electron in the laser field, $G_V^{(+)}(\mathbf{r}, t; \mathbf{r}', t')$. To account for the magnetic field component of the laser pulse at high intensities, we employ the non-dipole Volkov Green's function discussed in Appendix B. Neglecting continuum-continuum transitions [38], the dipole moment of the atom then reduces to

$$\begin{aligned} \mathbf{d}(t) &\simeq \int_{-\infty}^t dt' \int d\mathbf{r} d\mathbf{r}' \\ &\times \phi_0^*(\mathbf{r}, t) (-\mathbf{r}) G_V^{(+)}(\mathbf{r}, t; \mathbf{r}', t') H_i(t') \phi_0(\mathbf{r}', t') + \text{c.c.} \end{aligned} \quad (2.5)$$

The atom or ion is initially in its ground state and is described by the wave function $\phi_0(\mathbf{r}, t) = \phi_0(\mathbf{r}) \exp(iI_p t)$, I_p being the ionization potential of the state. $H_i(t')$ is the atom-field interaction Hamiltonian,

$$H_i(t') = \left[\mathbf{r} - \frac{i}{c} (\hat{\mathbf{k}} \cdot \mathbf{r}) \nabla \right] \cdot \mathbf{E}(\omega t'). \quad (2.6)$$

Eq. (2.5) can also be written in the form

$$\begin{aligned} \mathbf{d}(t) &\simeq 2\text{Im} \int_0^t dt' \int d\mathbf{p} \\ &\times \mathbf{d}_{\text{rec}}^*[\boldsymbol{\pi}(\mathbf{p}, t)] \exp[-iS(\mathbf{p}, t, t')] d_{\text{ion}}[\boldsymbol{\pi}(\mathbf{p}, t'), t'] \end{aligned} \quad (2.7)$$

where

$$\boldsymbol{\pi}(\mathbf{p}, t) = \mathbf{p} + \mathbf{A}(\omega t) + \frac{1}{c} \left[\mathbf{p} \cdot \mathbf{A}(\omega t) + \frac{1}{2} A^2(\omega t) \right] \hat{\mathbf{k}}, \quad (2.8)$$

$$S(\mathbf{p}, t, t') = \frac{1}{2} \int_{t'}^t dt'' [\boldsymbol{\pi}(\mathbf{p}, t'')]^2 + I_p(t - t'), \quad (2.9)$$

$$\mathbf{d}_{\text{rec}}(\mathbf{q}) = (2\pi)^{-\frac{3}{2}} \int d\mathbf{r} e^{-i\mathbf{q} \cdot \mathbf{r}} (-\mathbf{r}) \phi_0(\mathbf{r}), \quad (2.10)$$

and

$$d_{\text{ion}}(\mathbf{q}, t) = (2\pi)^{-\frac{3}{2}} \int d\mathbf{r} e^{-i\mathbf{q}\cdot\mathbf{r}} H_1(t) \phi_0(\mathbf{r}) . \quad (2.11)$$

The spectrum of the emitted photons is then obtained by calculating $|\hat{\mathbf{e}} \cdot \mathbf{a}(\Omega)|^2$, for emission polarized parallel to the polarization direction of the incident pulse, and $|\hat{\mathbf{k}} \cdot \mathbf{a}(\Omega)|^2$, for emission polarized along the direction of propagation of the incident pulse. In these expressions, Ω denotes the angular frequency of the emitted photon and $\mathbf{a}(\Omega)$ the Fourier transform of $\ddot{\mathbf{d}}(t)$. The ratio Ω/ω is an effective ‘harmonic order’. Results in the dipole approximation are obtained by setting $1/c = 0$. The depletion of the ground state can be neglected for the laser parameters and atomic systems considered here.

2.3 Saddle-point integration

The quasi-classical action $S(\mathbf{p}, t, t')$ is a rapidly varying function of \mathbf{p} , t and t' , and therefore the required integrations in equation (2.7) can be carried out using the saddle point method. We proceed by first using the relation

$$\begin{aligned} d_{\text{ion}}[\boldsymbol{\pi}(\mathbf{p}, t'), t'] &= -i \frac{d}{dt'} \int \frac{d\mathbf{r}}{(2\pi)^{\frac{3}{2}}} e^{-i\boldsymbol{\pi}(\mathbf{p}, t') \cdot \mathbf{r}} \phi_0(\mathbf{r}) \\ &= -i \frac{d}{dt'} \tilde{\phi}[\boldsymbol{\pi}(\mathbf{p}, t')], \end{aligned} \quad (2.12)$$

where

$$\begin{aligned} \tilde{\phi}[\boldsymbol{\pi}(\mathbf{p}, t')] &= \frac{(8I_p)^{\frac{5}{4}}}{8\pi} \frac{1}{[\boldsymbol{\pi}^2(\mathbf{p}, t')/2 + I_p]^2} \\ &= \frac{(8I_p)^{\frac{5}{4}}}{8\pi} \left[-\frac{\partial}{\partial t'} S(\mathbf{p}, t, t') \right]^{-2} \end{aligned} \quad (2.13)$$

is the Fourier transform of the ground state wave function of the ion. We have assumed that $V(r)$ is a Coulomb potential with effective nuclear charge $(2I_p)^{1/2}$. Equation (2.7) is then integrated by parts. Since $H_{\text{int}}(t' = 0) = 0$, the boundary term at $t' = 0$ is zero while the boundary term at $t' = t$ can be ignored; it corresponds to the process whereby the electron both ionizes and

recombines at time t . The new expression obtained for the dipole moment is simpler, allowing for a straightforward application of the saddle point method, described in the following subsection.

2.3.1 Exact saddle times

The saddle momentum \mathbf{p}_s depends on t and t' and is obtained by solving

$$\nabla_{\mathbf{p}} S(\mathbf{p}, t, t')|_{\mathbf{p}=\mathbf{p}_s} = 0 . \quad (2.14)$$

The calculations can be simplified even further by neglecting terms of order $1/c^2$ and higher in the saddle momentum. This means that the momentum $\boldsymbol{\pi}(\mathbf{p}_s, t)$ and the action $S(\mathbf{p}_s, t, t')$, respectively, will be correct to order $1/c$ and $1/c^2$. In this approximation

$$\begin{aligned} \mathbf{p}_s &= -\frac{\alpha_1(t, t')}{t-t'} \hat{\mathbf{e}} \\ &+ \frac{1}{c} \left[\frac{\alpha_1^2(t, t')}{(t-t')^2} - \frac{\alpha_2(t, t')}{2(t-t')} \right] \hat{\mathbf{k}}, \end{aligned} \quad (2.15)$$

where

$$\alpha_n(t, t') = \int_{t'}^t dt'' A^n(t''). \quad (2.16)$$

Next, the integral over \mathbf{p} is approximated using the saddle point method, with the result

$$\begin{aligned} \mathbf{d}(t) &\simeq 2\text{Im} \frac{(8I_p)^{\frac{5}{4}}}{8\pi} \int_0^t dt' C(\tau) \mathbf{d}_{\text{rec}}^*[\boldsymbol{\pi}(\mathbf{p}_s, t)] \\ &\times \exp[-iS(\mathbf{p}_s, t, t')] \left[\frac{\partial}{\partial t'} S(\mathbf{p}_s, t, t') \right]^{-1}. \end{aligned} \quad (2.17)$$

The factor

$$C(\tau) = (2\pi)^{\frac{3}{2}} \left((\varepsilon + i\tau)^3 \left[1 - \frac{1}{c^2} (\hat{\mathbf{e}} \cdot \mathbf{p}_s)^2 \right] \right)^{-\frac{1}{2}} \quad (2.18)$$

with $\tau = t - t'$ and ε a small positive parameter, can be understood physically as arising from wave packet spreading.

The form (2.17) of the dipole moment, obtained by using the properties of the Volkov wave function (see Appendix B), is most suited for the saddle point method; it explicitly shows that the time saddle point solution is also a first order pole in the pre-exponential factor. An adequate saddle point formula has to be used in this case (see Appendix C).

The integral over t' in Equation (2.17) is straightforward to evaluate numerically, but the integration must be repeated for each value of t , due to the dependence of the integrand on t . The total computational effort required for calculating the temporal variation of the dipole moment thus increases as the square of the laser pulse duration. For this reason, and because of the rapid oscillations of the exponential term, it is advantageous to calculate the integral using the saddle point method. The saddle times, t_s are complex and are determined by the equation

$$-\left. \frac{\partial}{\partial t'} S(\mathbf{p}_s, t, t') \right|_{t'=t_s} = [\boldsymbol{\pi}^2(\mathbf{p}_s, t')/2 + I_p] \Big|_{t'=t_s} = 0. \quad (2.19)$$

Figure 2.1 shows a typical case of the saddles' trajectories in the complex plane, for a two-cycle pulse.

Expanding the denominator in Eq. (2.17) in a Taylor series, retaining only the linear term, and noting that the integrand has a first-order pole at the saddle points (for the asymptotic formula in the case of an algebraic singularity at the saddle point, see Appendix C and Ref. [39]), the dipole moment is found to be

$$\begin{aligned} \mathbf{d}(t) \simeq & -2\text{Re} \frac{(8I_p)^{\frac{5}{4}}}{8} \sum_{t_s} C(t - t_s) \mathbf{d}_{\text{rec}}^*[\boldsymbol{\pi}(\mathbf{p}_s, t)] \\ & \times \exp[-iS(\mathbf{p}_s, t, t_s)] \left[\boldsymbol{\pi}(\mathbf{p}_s, t') \cdot \frac{\partial}{\partial t'} \boldsymbol{\pi}(\mathbf{p}_s, t') \right]_{t'=t_s}^{-1}. \end{aligned} \quad (2.20)$$

In all the cases considered, we have found that the spectra calculated using equation (2.20) are in very good agreement with those obtained by carrying out the integration over t' in equation (2.17) numerically. Typically, they differ by less than a factor of two, and the agreement improves as the laser intensity increases (see Figure 2.2).

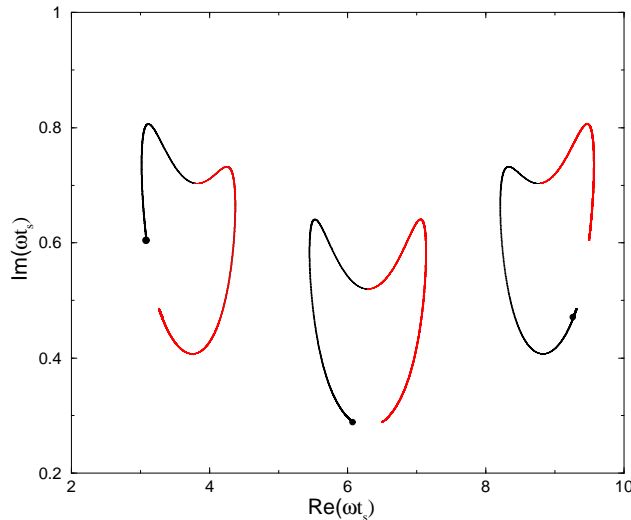


Figure 2.1: The saddle point trajectories $[\omega t_s(t)]$ from Eq. (2.19) in the complex plane for a He^+ ion irradiated by a two-cycle \sin^2 laser field, at 800 nm and peak electric field $E_0 = 0.4$ a.u. The full circles are the initial positions of the saddles at $t = 0$. The red curves represent the saddles contributing to the dipole moment $\mathbf{d}(t)$: $\text{Re}[t_s(t)] < \text{Re}(t)$.

2.3.2 Approximate saddle times

The saddle time can also be obtained using a semi-analytical approach, similar to the one described by Ivanov, Brabec and Burnett [40] for calculations in the dipole approximation. In this approach, the saddle time is expressed as $t_s = t_d + \Delta$, with t_d determined by solving

$$\pi_\epsilon(\mathbf{p}_s, t_d) = \hat{\epsilon} \cdot \boldsymbol{\pi}(\mathbf{p}_s, t_d) = 0. \quad (2.21)$$

The condition (2.21) for t_d states that the velocity of the electron along the polarization axis at the time of detachment is zero. Using Eq. (2.15), Eq. (2.21) reduces to

$$\int_{t_d}^t dt'' [\mathbf{A}(\omega t'') - \mathbf{A}(\omega t_d)] = 0, \quad (2.22)$$

thereby giving t_d in the dipole approximation.

The electron is assumed to start his motion in the continuum at time t_d in the origin, where the atomic core is located. Then, in terms of the electron's

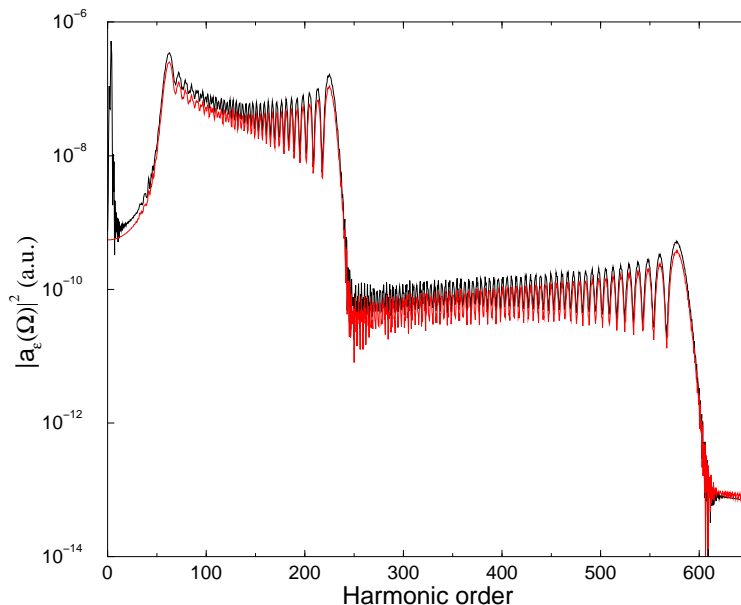


Figure 2.2: The magnitude squared of the Fourier transform of the dipole acceleration (in a.u.) as a function of the photon energy (in units of $\hbar\omega$), for a He^+ ion interacting with a two-cycle laser field of wavelength 800 nm. The peak electric field is $E_0 = 0.4$ a.u. and the photon emission is in the polarization direction. The black curve shows the exact results [numerical integration of Eq. (2.17)] and the red curve the results of the saddle point integration [Eq. (2.20)].

trajectory, Equation (2.14) can be interpreted as the condition for the canonical momentum \mathbf{p}_s such that the electron returns at the origin at time t (the recombination time). Using the Hamiltonian's expression for a free particle in an external electromagnetic field, one can re-write Eq. (2.14) in the form $\int_{t_d}^t dt' \nabla_{\mathbf{p}} H(\mathbf{p}, t, t') = 0$, as that the semiclassical action less the term depending on the ionization potential (which gives zero when differentiated over the canonical momentum) is the classical action of an electron moving freely in the electromagnetic field, with canonical momentum \mathbf{p} . As the classical action is the time-integral of the corresponding classical hamiltonian for the motion of a free electron in the external field, from the Hamilton's equations of motion, we have that the trajectory satisfies $d\mathbf{r}(t')/dt' = \nabla_{\mathbf{p}} H(\mathbf{p}, t, t')|_{\mathbf{p}=\mathbf{p}_s}$. Thus, Eq. (2.14) reads:

$$\int_{t_d}^t dt' d\mathbf{r}(t')/dt' = 0 \Leftrightarrow \mathbf{r}(t) = \mathbf{r}(t_d). \quad (2.23)$$

Using Eqs. (2.8), (2.15) and the condition (2.21) (where the later is coming from the saddle integration over time), one can now calculate the initial velocity in the direction of propagation, at the time of ‘birth’ in the continuum, t_d :

$$\begin{aligned}\pi_k(\mathbf{p}_s, t_d) &= \hat{\mathbf{k}} \cdot \boldsymbol{\pi}(\mathbf{p}_s, t_d) \\ &= -\frac{1}{2c(t-t_d)} \int_{t_d}^t dt'' |\mathbf{A}(\omega t'') - \mathbf{A}(\omega t_d)|^2 .\end{aligned}\quad (2.24)$$

This initial velocity is zero in the dipole approximation ($1/c = 0$), and non-zero in the non-dipole approach: in order to return at the origin, the electron must have an initial velocity at the time of detachment in order to compensate exactly the displacement imparted on it by the magnetic field component of the pulse [21]. Otherwise, it would miss the atomic core and the recombination process would be less effective.

To calculate the approximate saddle times, Eq. (2.19) is expanded in powers of $\Delta \equiv t_s - t_d$,

$$-\left. \frac{\partial}{\partial t'} S(\mathbf{p}_s, t, t') \right|_{t'=t_s} = s_0 + s_1 \Delta + \frac{1}{2} s_2 \Delta^2 + O(\Delta^3) . \quad (2.25)$$

Depending on the initial velocity component of $\boldsymbol{\pi}(\mathbf{p}_s, t_d)$ in the propagation direction, the first coefficient is

$$s_0 = I_p + \frac{1}{2} \pi_k^2(\mathbf{p}_s, t_d) . \quad (2.26)$$

Analytical expressions for s_1 and s_2 are lengthy, and in practice can be obtained numerically. Setting equation (2.25) to zero and solving for Δ , the dipole moment (2.20) is evaluated using

$$\begin{aligned}S(\mathbf{p}_s, t, t_s) &\simeq S(\mathbf{p}_s, t, t_d) - \\ & s_0 \Delta - \frac{1}{2} s_1 \Delta^2 - \frac{1}{6} s_2 \Delta^3\end{aligned}\quad (2.27)$$

and

$$\left[\boldsymbol{\pi}(\mathbf{p}_s, t') \cdot \frac{\partial}{\partial t'} \boldsymbol{\pi}(\mathbf{p}_s, t') \right]_{t'=t_s} \simeq s_1 + \Delta s_2 . \quad (2.28)$$

We have verified that this approach yields results that are for all practical purposes identical to those derived using Eqs. (2.19) and (2.20).

The coefficients s_1 and s_2 , to order $1/c^2$, are then found to be

$$s_1 = \frac{\pi_k^2(\mathbf{p}_s, t_d)}{t - t_d} \quad (2.29)$$

$$s_2 = E^2(\omega t_d) \left[1 + \frac{1}{c} \pi_k(\mathbf{p}_s, t_d) \right] + \frac{3s_1}{t - t_d}, \quad (2.30)$$

Note that all of the non-dipole corrections to the expansion coefficients s_i are of order $1/c^2$. Hence, consistent with the action being correct to order $1/c^2$, we set

$$s_1 = 0, \quad s_2 = E^2(\omega t_d). \quad (2.31)$$

The resulting dipole moment can be expressed as [21, 40]

$$\mathbf{d}(t) \simeq -2\text{Im} \sum_{t_d} \mathbf{a}_{\text{rec}}^*(t, t_d) a_{\text{pr}}(t, t_d) a_{\text{ion}}(t, t_d), \quad (2.32)$$

with the ionization, propagation and recombination amplitudes, respectively, given by

$$a_{\text{ion}}(t, t_d) = \frac{(8I_p)^{\frac{5}{4}}}{8(2s_0s_2)^{\frac{1}{2}}} \exp \left[-\frac{1}{3} \left(\frac{8s_0^3}{s_2} \right)^{\frac{1}{2}} \right], \quad (2.33)$$

$$a_{\text{pr}}(t, t_d) = C(t - t_s) \exp[-iS(\mathbf{p}_s, t, t_d)], \quad (2.34)$$

$$\mathbf{a}_{\text{rec}}^*(t, t_d) = \mathbf{d}_{\text{rec}}^*[\boldsymbol{\pi}(\mathbf{p}_s, t)]. \quad (2.35)$$

Note that the ionization amplitude $a_{\text{ion}}(t, t_d)$ from Eq. (2.33) depends exponentially on the initial velocity in the propagation direction $v_{\perp} \equiv \pi_k(\mathbf{p}_s, t_d)$ at the time of detachment t_d , through the quantity s_0 [given by Eq. (2.26)]:

$$a_{\text{ion}}(t, t_d) \propto \exp \left[-\frac{2}{3} \frac{(2I_p + v_{\perp}^2)^{\frac{3}{2}}}{|E(\omega t_d)|} \right]. \quad (2.36)$$

The bigger the effect of the magnetic field component on the electron's trajectory (thus bigger v_{\perp}), the smaller the ionization amplitude is.

We have evaluated the accuracy of the formula (2.32) by calculating $|\hat{\boldsymbol{\epsilon}} \cdot \mathbf{a}(\Omega)|^2$ and comparing with the results obtained using exact numerical complex saddle

times t_s in Eq. (2.20) (see Figure 2.3). The approximation given by equation (2.32) works extremely well: the spectra cannot be distinguished on the scales used in the diagrams. The agreement improves for higher intensities.

The expression of $\mathbf{d}(t)$ given by Walser *et al.* [21] is obtained by ignoring the non-dipole corrections in the pre-exponential factor in the ionization amplitude (2.33) and the recombination amplitude (2.35)¹. These additional approximations have no significant effect on the emission spectra for photons polarized along the laser polarization direction. Setting $1/c = 0$ in all three amplitudes in equation (2.32) leads to the formula obtained by Ivanov, Brabec and Burnett [40] in the dipole approximation.

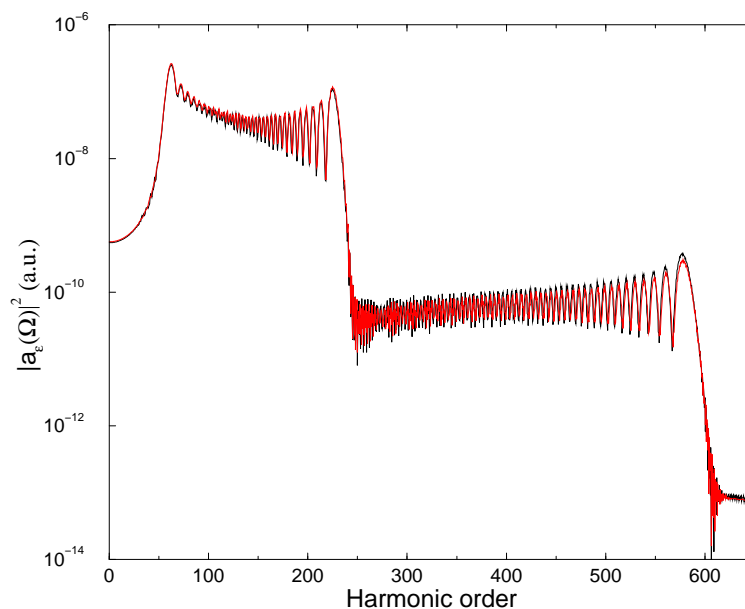


Figure 2.3: Photon emission in the polarization direction for a He^+ ion, irradiated by a two-cycle laser pulse, at 800 nm. The black curve shows the result of the exact saddle point integration and the red curve the approximated saddle integration [Eq. (2.32)].

¹In the notation of Ref. [21], $P_x(t, t_0)$ and $P_z(t, t_0)$ are identical, respectively, to $\hat{\mathbf{e}} \cdot \mathbf{p}_s$ and $\hat{\mathbf{k}} \cdot \mathbf{p}_s$, where \mathbf{p}_s is defined by Eq. (2.15), and $P_{zd} \equiv -\pi_k(\mathbf{p}_s, t_d)$. We take that the equation defining $S_m(t, t_0)$ in Ref. [21] should read $S_m(t, t_0) = (1/2m) \int_{t_0}^t dt' \{P_z(t, t_0) - e/(mc^2)[P_x(t, t_0)A(t') - e/(2c)A^2(t')]\}^2$.

2.4 Non-dipole effects in photon emission for stationary fields

Dipole (D ϵ) and non-dipole non-relativistic (ND ϵ , NDk) spectra are compared in Figure 2.4 for photon emission by multiply charged ions driven by a stationary 800 nm laser field. The modulus squared of the Fourier transform of the dipole acceleration is plotted against the effective harmonic order, Ω/ω . The Fourier transform of the dipole acceleration is defined as

$$\mathbf{a}(\Omega) = \frac{1}{(2\pi)^{\frac{1}{2}}} \int_T^{T+2\pi/\omega} dt \exp(-i\Omega t) \ddot{\mathbf{d}}(t), \quad (2.37)$$

where T is chosen large enough so as to include the long trajectories that contribute to the dipole moment. We use the notation $a_\epsilon(\Omega) = \hat{\boldsymbol{\epsilon}} \cdot \mathbf{a}(\Omega)$ and $a_k(\Omega) = \hat{\mathbf{k}} \cdot \mathbf{a}(\Omega)$ for the components of the acceleration.

The gradual breakdown of the dipole approximation with increasing intensity is illustrated in Fig. 2.4 for emission by a Ne⁶⁺ ion ($I_p = 207.3$ eV). Going from 0.5 to 4×10^{17} W cm⁻², the influence of the magnetic field component first manifests itself as a reduction in photon emission polarized along $\hat{\boldsymbol{\epsilon}}$ as compared to the dipole approximation, then to a ‘bending over’ of the plateaus, and finally to a marked suppression of emission at both ends of the spectrum and to the disappearance of the intermediate cutoffs which separate the plateaus in the dipole approximation. A small shift in the position of the cutoffs is also noticeable.

Non-dipole spectra for emission polarized parallel to the direction of propagation of the incident field are also shown in Fig. 2.4. Emission of photons polarized in this direction is forbidden in the dipole approximation. Emission polarized along the propagation direction is weaker compared to emission polarized along $\hat{\boldsymbol{\epsilon}}$, but the spectra are otherwise similar in most respects. The dip visible in the low-energy part of Figs. 2.4(a) and (b) also occurs when ions are driven by ultrashort pulses, and can be attributed to accidental cancellations between different terms contributing to the dipole moment [22]. In Fig.

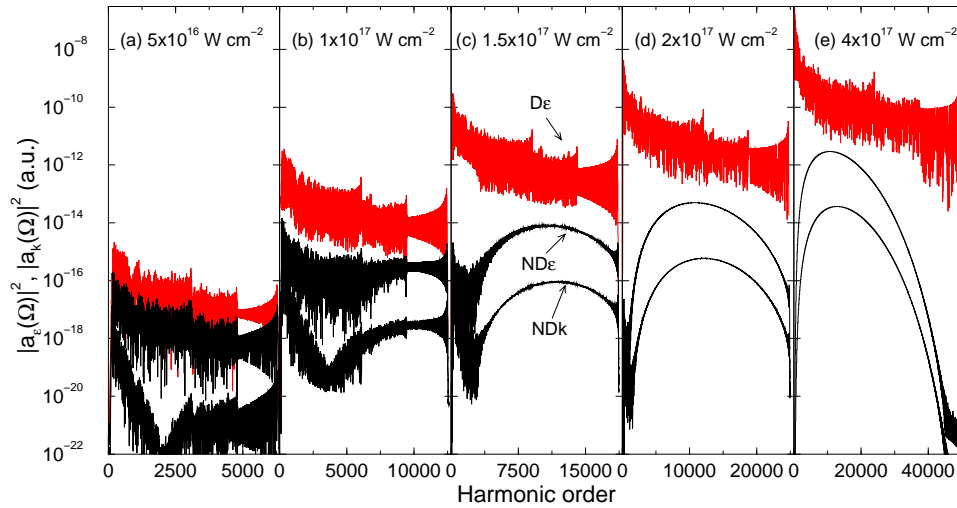


Figure 2.4: The magnitude squared of the Fourier transform of the dipole acceleration (in a.u.) as a function of the photon energy (in units of $\hbar\omega$), for a Ne^{6+} ion interacting with a stationary laser field of wavelength 800 nm. Spectra for the emission of photons polarized along the laser polarization direction obtained in the dipole approximation ($D\epsilon$) and in the non-dipole non-relativistic approximation ($ND\epsilon$) are shown, as well as the non-dipole non-relativistic spectra for photon emission polarized along the laser propagation direction (NDk).

2.4(a), we observe that $|a_e(\Omega)|^2$ is reduced by more than one order of magnitude compared to the predictions of the dipole approximation at the relatively weak intensity of $5 \times 10^{16} \text{ W cm}^{-2}$. This reduction contrasts with the smaller decrease found for a Li^{2+} ion irradiated by a two-cycle 800 nm pulse of $9 \times 10^{16} \text{ W cm}^{-2}$ peak intensity [22, 25], and the even smaller non-dipole effects found for a He^+ ion irradiated by a 5-fs 800 nm pulse of $5 \times 10^{16} \text{ W cm}^{-2}$ peak intensity [21]. The origin of the difference between the results of Fig. 2.4 and the results for He^+ and Li^{2+} can be attributed to the larger ionization potential of Ne^{6+} [see Eq. (2.36), where the binding potential appears together with the initial velocity v_{\perp} ; the larger I_p is, the stronger the non-dipole effects manifest themselves through the term v_{\perp}].

The strong dependence on I_p , and in fact all the major differences between the dipole and non-dipole spectra, can be understood within the framework of the recollision model. Only two quantities are relevant: the ionization amplitude

$a_{\text{ion}}(t, t_d)$ [proportional to the detachment rate when the electron is born, see Eq. (2.36)] and the kinetic energy of the electron when it returns to the core. Since the propagation and recombination amplitudes vary far less in magnitude than $a_{\text{ion}}(t, t_d)$ from trajectory to trajectory, the importance of the contribution to the spectrum of the different trajectories can be effectively gauged by the corresponding values of the ionization rates at the detachment times.

In the dipole approximation, a_{ion} is largest for the long trajectories, as electrons having short trajectories are detached at lower electric fields. Therefore, short trajectories tend to contribute less to the photon emission spectrum. However, when the magnetic field component of the laser field is taken into account, the opposite is true. This is due to the fact that $\pi_k(\mathbf{p}_s, t_d)$ is larger for the long trajectories than for the short ones. The exponential dependence of $a_{\text{ion}}(t, t_d)$ on the initial transverse velocity means that the ionization amplitude tends to be smaller for the long trajectories than for the short ones, and the latter end up dominating the spectrum over much of its range [1]. The secondary plateaus, which arise from interference between the longest trajectories, almost completely vanish. The oscillations evident in the dipole spectrum largely disappear because at most frequencies only one set of trajectories (the short ones) significantly contribute to emission. The spectrum ‘bends over’ as ionization is exponentially suppressed, due to the relatively small value of $|\mathbf{E}(t_d)|$ for the short trajectories that give rise to the lower harmonics and to the large initial transverse velocity for the short trajectories that produce the high harmonics.

2.5 Importance of relativistic effects

We now evaluate the importance of the relativistic effects neglected in our approach by comparing, in Fig. 2.5, the non-dipole non-relativistic results with relativistic results recently obtained by Milošević, Hu and Becker [1, 24]. The case of a Ne^{6+} ion interacting with a stationary field of wavelength 1054 nm and intensities 0.7×10^{17} and 1.4×10^{17} W cm⁻² is considered. Milošević’s,

Hu's and Becker's calculations are also done within the SFA but are based on the Klein-Gordon equation rather than on the Schrödinger equation. The relativistic results shown in the figure are the emission rates presented in Fig. 2 of Ref. [1], rescaled so as to facilitate comparison⁴.

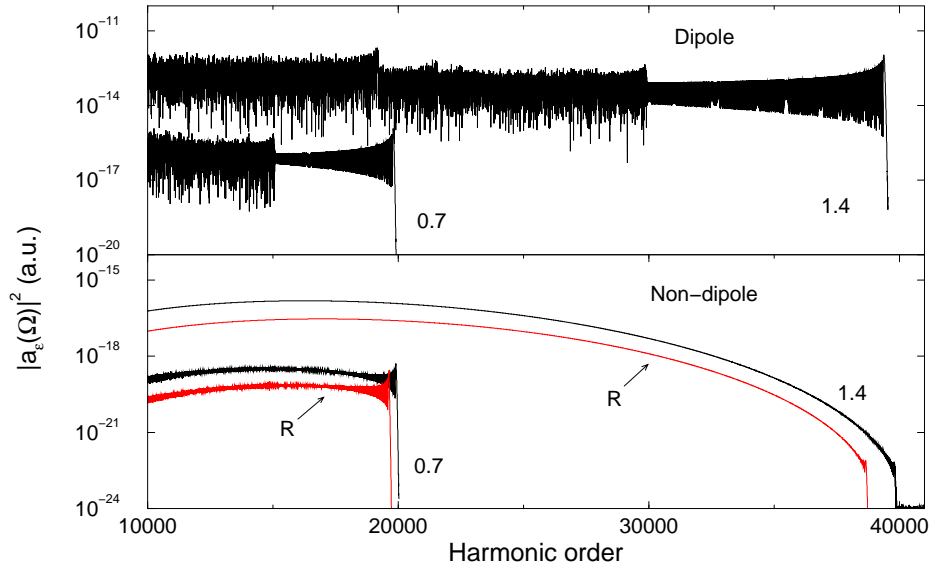


Figure 2.5: The magnitude squared of the Fourier transform of the dipole acceleration (in a.u.) as a function of the photon energy (in units of $\hbar\omega$). Spectra for a Ne^{6+} ion obtained in the dipole and non-dipole non-relativistic approximations are shown for the emission of photons polarized along the laser polarization direction. The ion is irradiated by a stationary laser field of peak intensities 0.7 and $1.4 \times 10^{17} \text{ W cm}^{-2}$, as indicated, and wavelength 1054 nm. The non-dipole results are compared with the relativistic results (R) of Milošević, Hu and Becker [1].

The large differences between the dipole and non-dipole results indicate a strong influence of the magnetic field component of the laser field for these parameters. As in Figs. 2.4 (d) and (e), the non-dipole spectrum is completely dominated by the short trajectories at $1.4 \times 10^{17} \text{ W cm}^{-2}$. At this inten-

⁴The rates of Ref. [1] are proportional to the square of the modulus of the Fourier transform of $\mathbf{d}(t)$ multiplied by the cube of the frequency of the emitted photon, Ω [private communication with D. B. Milošević (2002)]. In order to compare them with the values of $|a_\epsilon(\Omega)|^2$ we have obtained, the rates have been multiplied by Ω and an arbitrary numerical factor. (The same factor is used for both intensities.)

sity, the maximum velocity of the electron, v_{\max} , is at most 42 percent of the speed of light (i.e., $v_{\max}^2/c^2 = 0.18$) for any returning trajectory. The good agreement between our non-dipole non-relativistic spectra and the relativistic spectra, aside from an arbitrary overall factor, suggests that the relativistic effects that are not taken into account in our model are not important. The difference is largest for the highest harmonics, as could be expected since v_{\max}^2/c^2 grows linearly with the energy of the photon emitted at recombination for electrons following short trajectories. In the non-dipole non-relativistic calculation, compared to the spectra obtained in the dipole approximation, the cutoffs occur at a slightly higher photon energy. The origin of this effect is the additional kinetic energy the returning electron acquires due to its drift along the pulse propagation direction. The non-dipole non-relativistic calculation neglects other effects, such as the increase in the inertial mass, that contribute to the kinetic energy to order $1/c^2$. In the relativistic results, these additional effects lead to a small displacement of the cutoffs to lower energies. Finally, we note that v_{\max}^2/c^2 is less than 0.18 for the short trajectories responsible for the generation of photons below the harmonic order 30,000 at 800 nm wavelength, and is less than 0.10 for the short trajectories responsible for the strongest photon emission in Figure 2.4. The relativistic effects are therefore not expected to be significant at the intensities considered.

2.6 Harmonic generation in short pulses

We briefly discuss photon emission by ions driven by ultrashort pulses. Spectra for 3- and 4-cycle pulses are shown in the top and middle diagrams of Fig. 2.6. The field is described by Eqs. (2.1) and (2.2) with

$$f(\eta) = \sin^2\left(\frac{\eta}{2n}\right), \quad (2.38)$$

where n denotes the number of optical cycles of the pulse. The pulse is assumed to extend over all space. The corresponding Fourier transform of the dipole

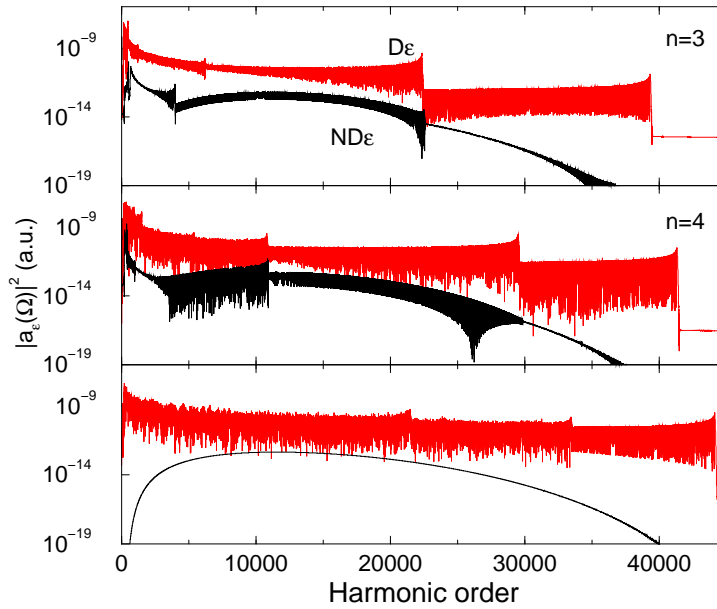


Figure 2.6: The magnitude squared of the Fourier transform of the dipole acceleration (in a.u.) as a function of the photon energy (in units of $\hbar\omega$). Spectra for a Be^{3+} ion obtained in the dipole and non-dipole approximations are shown for the emission of photons polarized along the laser polarization direction ($D\epsilon$, $ND\epsilon$) for a 3-cycle pulse ($n=3$), a 4-cycle pulse ($n=4$) and a stationary field. The peak intensity is $3.6 \times 10^{17} \text{ W cm}^{-2}$ and $\lambda = 800 \text{ nm}$.

acceleration is

$$\mathbf{a}(\Omega) = \frac{1}{(2\pi)^{\frac{1}{2}}} \int_0^{2\pi n/\omega} dt \exp(-i\Omega t) \ddot{\mathbf{d}}(t). \quad (2.39)$$

The integral extends over the entire duration of the pulse instead of just one optical cycle as in the case of a stationary field. Results for a stationary field of the same intensity are shown in the bottom diagram. The plateau structure of the spectra for few-cycle pulses largely originates from the temporal variation of the intensity rather than from the contribution of very long trajectories [41]. (For every half-cycle during an ultra-short pulse, the trajectories are detached with different probabilities and return with different kinetic energies.) Overall, the magnetic field component of an ultra-short pulse affects photon emission in a similar way as for stationary fields. However, for short pulses, photon emission is not as strongly suppressed at the low energy end of the spectrum, and plateau structures with oscillations are still visible. This indicates that

more than one electron trajectory is contributing to the emission of a particular harmonic in the largest part of the spectrum.

2.7 Conclusions

We have given a detailed account of the approach introduced in Refs. [21, 22] for describing photon emission by ions interacting with laser fields (stationary or pulsed) whose peak intensities are sufficiently high so that the dipole approximation is no longer applicable. This approach can be viewed as a non-dipole generalization of the SFA theory of Lewenstein and co-workers [9, 16]. It applies to the dynamical regime that lies between the usual non-relativistic dipole regime and the fully relativistic regime. Using the non-dipole non-relativistic Volkov wave functions (see Appendix B.4) and within the SFA, we have shown that the time-dependent dipole moment of the ion in the laser field, $\mathbf{d}(t)$, can be reduced to the simple form given by Eq. (2.20). Then through a series of approximations, none of which compromise the accuracy of the calculations in any significant way, we recover the expression for the dipole moment derived by Walser *et al.* [21], whereby $\mathbf{d}(t)$ is obtained as a sum over amplitudes arising from particular electron trajectories.

The trajectories satisfy two simple classical criteria. First, if the electron is detached at some earlier time t_d , its displacement along the polarization direction must be zero at time t . Second, at time t_d its velocity along the laser pulse propagation direction, v_{\perp} , must be non-zero in order to counter-act the drift due to the magnetic component of the field. One recognizes the language of the recollision model, modified so as to include the magnetic field effects on the detached electron. As in the intensity regime where the dipole approximation is applicable, it follows that the main features of photon emission spectra can be understood from two key quantities, namely the tunnel ionization rate when the electron is detached and the kinetic energy of the electron when it returns to the core. In contrast to the dipole approximation, the tunnel ionization

rates depend now strongly on v_{\perp} , and on particular on its magnitude relative to I_p and the magnitude of the electric field at the time of detachment. The overall effect of the dependence on v_{\perp} results, at sufficiently high intensities, in a strong suppression of photon emission. Only trajectories with $t - t_d$ and $|v_{\perp}|$ small contribute meaningfully to the emission spectrum. As was emphasized recently in Ref. [11], it is remarkable that multiphoton processes in atoms interacting with intense fields, despite their apparent complexity, can be largely understood in terms of classical trajectories of electrons that are detached and then return, driven by the external field, to their parent ion. Manipulation of the individual electron trajectories translates into an easy way to alter the atomic system's response to the external field, by controlling a relatively small number of parameters.

Chapter 3

‘Undoing’ the non-dipole effects in harmonic generation

3.1 Outline

At intensities where the dipole approximation is valid, the contribution of each electron trajectory to photon emission depends primarily on the electric field strength at the time of ionization. At higher intensities, the contribution of a particular trajectory can be drastically reduced by the drift induced by the magnetic component of the field. As discussed in detail in Chapter 2, to return at the nucleus the electron must be emitted with a non-zero velocity in the direction of the field propagation, and the probability for this is exponentially small in the tunnelling regime. At the intensities considered here, the Lorentz force acting on the electron has a magnitude comparable to that exerted by the electric field component of a relatively weak laser field. This suggests that the magnetic drift can be compensated, at least for certain trajectories, by irradiating the ion with a second, weak laser field, polarized along the propagation direction of the intense one. In Section 3.2, we show by an example that a selective compensation of the magnetic drift through this mechanism is indeed possible; consequences for single attosecond emission in the same context of non-dipole effects, are discussed in Section 3.3. The details of choosing the weak field’s parameters (such as its intensity and the time delay with respect

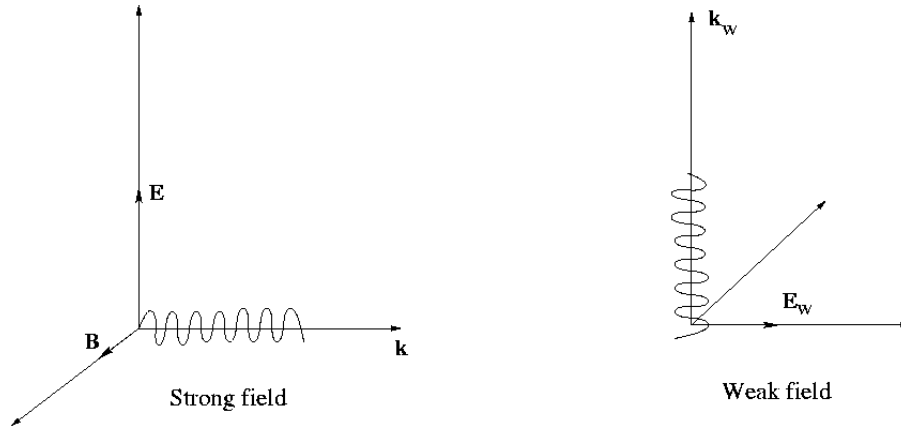


Figure 3.1: The configuration of the strong and weak laser pulses.

to the strong field) are described in Section 3.4.

Finally, conclusions and some suggestions for further applications are presented in Section 3.5.

3.2 Adding a second electric field

We consider the case of a Ne^{6+} ion irradiated by a combination of two ultra-short pulses, both with the same carrier wavelength (800 nm). The first pulse, with vector potential \mathbf{A} , propagates in the direction $\hat{\mathbf{k}}$ and has the polarization vector $\hat{\mathbf{e}}$. The second pulse has the vector potential \mathbf{A}_w and the polarization vector $\hat{\mathbf{e}}_w$, with $\hat{\mathbf{e}}_w \equiv \hat{\mathbf{k}}$ (see Fig. 3.1).

We assume that the second pulse is weak enough that it can be treated in the dipole approximation. Therefore, the Schrödinger equation governing the motion of the electron in the non-dipole non-relativistic approach reads

$$i\frac{\partial}{\partial t}\Psi(\mathbf{r}, t) = \left(\frac{1}{2}[-i\nabla + \mathbf{A}(\omega t) + \mathbf{A}_w(\omega t)]^2 + \frac{1}{c}(\hat{\mathbf{k}} \cdot \mathbf{r})[-i\nabla + \mathbf{A}(\omega t)] \cdot \mathbf{E}(\omega t) + V(r) \right) \Psi(\mathbf{r}, t),$$

with $\mathbf{E}(\omega t) = -(d/dt)\mathbf{A}(\omega t)$. Within the SFA, the dipole moment of the ion can be still be expressed as in Eqs. (2.17) and (2.20), with the saddle momen-

tum and the saddle times determined by Eqs. (2.14) and (2.19); however, we now have

$$\boldsymbol{\pi}(\mathbf{p}, t) = \mathbf{p} + \mathbf{A}(\omega t) + \left\{ A_w(\omega t) + \frac{1}{c} \left[\mathbf{p} \cdot \mathbf{A}(\omega t) + \frac{1}{2} A^2(\omega t) \right] \right\} \hat{\mathbf{k}}. \quad (3.1)$$

We assume that the two pulses have the same envelope, with the second pulse delayed a time τ_w with respect to the first one. We take, specifically,

$$\mathbf{A}(\omega t) = \frac{E_0}{\omega} \sin^2 \left(\frac{\omega t}{2n} \right) \sin(\omega t) \hat{\mathbf{e}}, \quad (3.2)$$

and

$$\mathbf{A}_w(\omega t) = \frac{E_{0w}}{\omega} \sin^2 \left(\frac{\omega t - \delta}{2n} \right) \sin(\omega t - \delta) \hat{\mathbf{k}}, \quad (3.3)$$

where $\delta = \omega \tau_w$ and n is the number of optical cycles encompassed by each pulse. In the classical model, an electron detached at a time t_d must have an initial velocity

$$\begin{aligned} \mathbf{v}_\perp = & -\frac{1}{t - t_d} \left\{ \int_{t_d}^t dt'' [A_w(\omega t'') - A_w(\omega t_d)] \right. \\ & \left. + \frac{1}{2c} \int_{t_d}^t dt'' [A(\omega t'') - A(\omega t_d)]^2 \right\} \hat{\mathbf{k}} \end{aligned} \quad (3.4)$$

to return at the nucleus at time t . The electric field amplitude of the second pulse, E_{0w} , and the time delay τ_w are chosen so that $\mathbf{v}_\perp \approx 0$ for a particular group of trajectories.

The left panel in Fig. 3.2 shows the magnitude squared of the Fourier transform of the dipole acceleration of Ne^{6+} as a function of the photon energy for a two cycle Ti:Sapphire pulse with $E_0 = 3.2$ a.u. acting alone ($E_{0w} = 0$). In order to illustrate more clearly the differences between the dipole and non-dipole results, the fast oscillations in the spectra have been averaged. Let us first consider the trajectory of an electron ‘born’ at time $t_d = 116$ a.u. during the laser pulse. If the Lorentz force was negligible, the electron would return to the nucleus at time $t \approx 190$ a.u., where it could recombine with emission of a photon of energy 7500ω . However, the Lorentz force is not negligible: in order to return the electron must have an initial velocity of about 2 a.u. opposite to

the direction of propagation of the pulse. Correspondingly, $|a_e(\Omega)|^2$ is much reduced, compared to its value in the dipole approximation [see Eq. (2.36) and the related discussion].

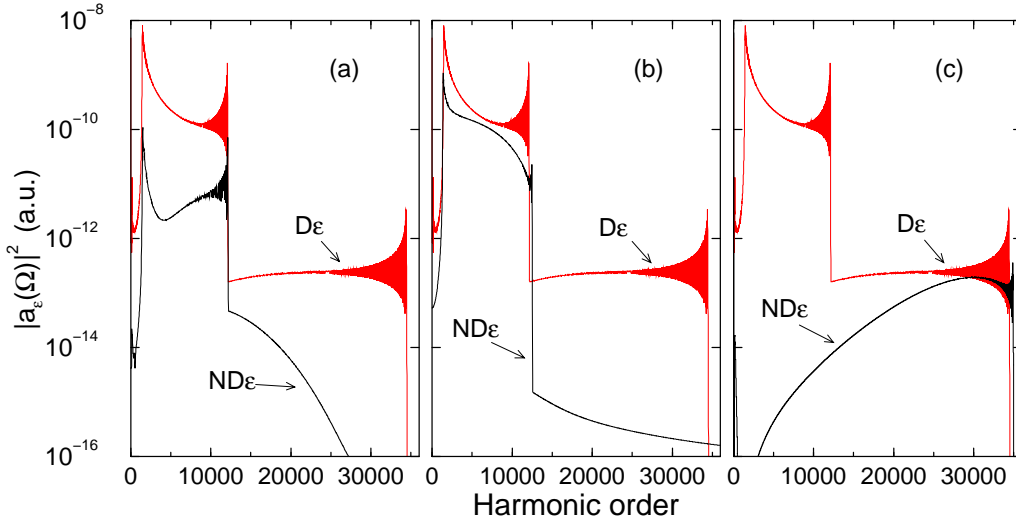


Figure 3.2: The magnitude squared of the Fourier transform of the dipole acceleration, in a.u., of Ne^{6+} as a function of the photon energy (in units of $\hbar\omega$). The laser pulse duration is two-cycles, with peak intensity $3.6 \times 10^{17} \text{ W cm}^{-2}$ and wavelength 800 nm. Dipole ($D\epsilon$) and non-dipole ($ND\epsilon$) spectra are shown. In plots (b) and (c), the non-dipole results are for the case in which the ion interacts with a second, weaker laser pulse polarized along the propagation direction of the intense pulse (see text). In plot (b), the time delay ($\tau_w = 62 \text{ a.u.}$) and intensity ($I_w = 4.8 \times 10^{15} \text{ W cm}^{-2}$) of the second pulse were chosen such that photon emission in the neighborhood of the 7500th harmonic is enhanced, while in plot (c), $\tau_w = -80 \text{ a.u.}$ and $I_w = 3.6 \times 10^{15} \text{ W cm}^{-2}$, leading to the enhancement of emission around the 30 000th harmonic.

If, in addition, the ion is irradiated by a second two-cycle pulse, of field strength $E_{0w} = 0.37 \text{ a.u.}$ and delayed by $\tau_w = 62 \text{ a.u.}$ with respect to the first pulse, the electron returns to the core if detached with zero velocity at time $t_d = 116 \text{ a.u.}$ In the centre panel in Fig. 3.2 we see that the magnitude of the non-dipole spectrum is now comparable to the spectrum obtained in the dipole approximation in the region of the 7500th harmonic. The small difference is due to the fact that the magnetic drift is compensated only for some of the trajectories that contribute to emission in this part of the spectrum, namely those with $t_d \approx 116 \text{ a.u.}$

Photon emission in the region of the cutoff of the second plateau can be enhanced in a similar manner, by choosing the delay and the strength of the second pulse to be $\tau_w = -80$ a.u. and $E_0 = 0.32$ a.u., respectively. The resulting spectrum is shown in the right panel of Fig. 3.2.

3.3 Attosecond pulse generation

Finally, we investigate how the magnetic field component of the laser pulse influences photon emission in the time domain. We calculate the frequency-resolved dipole acceleration for emission in a narrow frequency window centered about Ω , defined by [42]

$$a_e(t, \Omega) = \frac{1}{(2\pi)^{\frac{1}{2}}} e^{i\Omega t} \int_0^\infty d\Omega' e^{i(\Omega' - \Omega)t} F(\Omega' - \Omega) \hat{\mathbf{e}} \cdot \mathbf{a}(\Omega'), \quad (3.5)$$

where $F(\Omega' - \Omega)$ is a Gaussian window centered at $\Omega' = \Omega$. The transformation described in Eq. (3.5) is known as the Gabor transform [43]. The square modulus of $a_e(t, \Omega)$ is shown in Fig. 3.3, for Ne^{6+} interacting with a 4-cycle pulse of 3.6×10^{17} W cm $^{-2}$ peak intensity at 800 nm wavelength. We concentrate on emission of 3.9 keV photons ($\Omega = 2500\omega$).

The results calculated in the dipole approximation are shown in Fig. 3.3(a). Each spike in this diagram corresponds to a burst of emission of 3.9 keV photons. The spikes occur precisely at the instants where, in the recollision model, detached electrons return at the nucleus with the speed required for emission at this energy. Seven bursts are particularly strong and have all about the same intensity, showing that in the dipole approximation the emission is dominated by seven groups of trajectories.

However, the magnetic drift, when taken into account, changes this picture dramatically. The central part of the figure, where the non-dipole results are plotted, shows that all but one of the seven returns that contribute most in the dipole approximation are severely suppressed. The only significant emission event occurs towards the end of the pulse and dominates the spectrum.

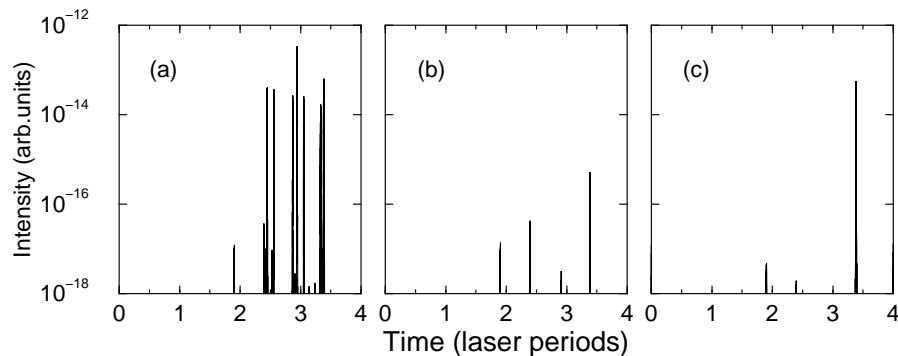


Figure 3.3: The magnitude squared of the frequency-resolved dipole acceleration for photon emission centered about the 2500th harmonic of the driving field by a single Ne^{6+} ion interacting with a four-cycle Ti:Sapphire pulse of $3.6 \times 10^{17} \text{ W cm}^{-2}$ peak intensity. Shown are results obtained in the dipole approximation (a) and in the non-dipole non-relativistic approximation (b, c). Plot (c) shows the enhancement by a second laser pulse of photon emission at 3.4 laser periods. The peak intensity of the second pulse, I_w , is $2.2 \times 10^{14} \text{ W cm}^{-2}$ and the delay, τ_w , is 30.8 a.u.

The width of the spike indicates that the duration of the burst is about 20 attoseconds. The other trajectories make a smaller contribution; their main effect is to induce, by interference, the oscillations in the non-dipole spectrum which are visible in the lower curve of Fig. 3.4.

In Fig. 3.3(c), we present $|a_e(t, \Omega)|^2$ calculated for a superposition of the same intense pulse with another Ti-Sapphire pulse, as discussed in Section 3.2. The electric field amplitude of the second pulse, E_{0w} , and the delay between the two pulses, τ_w , are chosen so as to compensate the magnetic drift for the trajectory giving rise to the strongest burst of emission in Fig. 3.3(b). As seen from the diagram, when the magnetic drift is compensated emission is as strong as in the dipole approximation. The other trajectories are further suppressed by the second pulse, with the consequence that a single attosecond pulse of X-ray photons is emitted. The same conclusions can be drawn from the corresponding spectrum, shown in Fig. 3.4. In fact, one sees from the spectrum that with the second pulse, emission is much more intense and occurs as a single burst

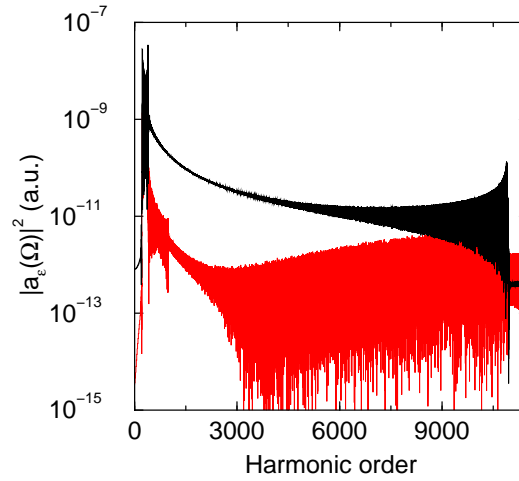


Figure 3.4: The magnitude squared of the Fourier transform of the dipole acceleration of a single Ne^{6+} ion interacting with a four-cycle Ti:Sapphire pulse of $3.6 \times 10^{17} \text{ W cm}^{-2}$ peak intensity. Shown are results obtained in the non-dipole non-relativistic approximation, with the upper curve illustrating the enhancement of photon emission around $\Omega/\omega = 2500$ when the ion interacts with a second, weaker laser pulse having the same peak intensity and delay as in Fig. 3.3. The high energy part of the spectrum is not shown.

(note the absence of oscillations), not only for $\Omega = 2500\omega$ but also in a large range of frequencies around this value.

3.4 How to correct the non-dipole effects for a given harmonic order

To enhance the emission of a certain harmonic order Ω , one needs to calculate the parameters of the weak field [its intensity and delay – see Eq. (3.3)]. These parameters have to be chosen such that to cancel the magnetic drift of a certain trajectory that contributes to the harmonic emission Ω .

First, we have to find all the emission times of the harmonic order we are interested in correcting. This can be accomplished by performing a Gabor transform, with the Gaussian window centered on the emitted frequency Ω . Figure 3.3 shows a typical output of the Gabor transform: in the left panel,

the dipole contributions are shown, while the centre panel displays the same contributions in the non-dipole calculation. The emission peaks are in the form of short bursts of radiation (as short as of the order of attoseconds). The attenuation due to the effect of the magnetic field component of the laser field is visible. From the Gabor transform of the dipole spectrum, we then choose a certain peak we want to enhance with the help of the second laser field. Once a particular emission time t_r is selected, we need to calculate the corresponding time t_d when the electron is ‘born’ in the field. This can be done within the Simpleman model [Eq. (2.22)], by searching for the electron trajectories returning to the nucleus along the polarization axis, at time t_r . With the two times calculated, we now turn to the expression of v_\perp from Eq. (3.4) and search for the second field’s amplitude and delay such that to cancel v_\perp (we assume here for simplicity that the second laser field has the same shape of the envelope as the strong driving field). This way, the emission of the harmonic order Ω due to the particular trajectory we enhanced will have the same order of magnitude as in the dipole approximation calculation.

In Fig. 3.2, discussed at the end of Section 3.2, to enhance the 7500th harmonic we chose the time of detachment $t_d = 116$ a.u. and the return time $t_r = 190$ a.u. for a particular electron trajectory contributing to the harmonic emission. Figure 3.5 shows the return times as a function of detachment times, calculated from the Simpleman model; knowing the return time from the Gabor analysis, one can calculate approximatively the emission time. The possible pairs $(\omega t_d, \omega t_r)$ are shown by filled circles, for $t_r = 190$ a.u. The detachment time chosen in Section 3.2 ($t_d = 116$ a.u., the third pair in Fig. 3.5) is seen to correspond to the biggest electric field $|E(\omega t_d)|$ at the time of emission.

With the trajectory known, we plot the velocity v_\perp from Eq. (3.4) for various weak field amplitudes as a function of the weak field’s delay (the only two parameters that need to be calculated). Figure 3.6 shows such a graph, for two different values for the weak field’s amplitude: the minimal value of $E_{0w} = 0.15$ a.u. for which the initial speed can be zero, and the one chosen in the

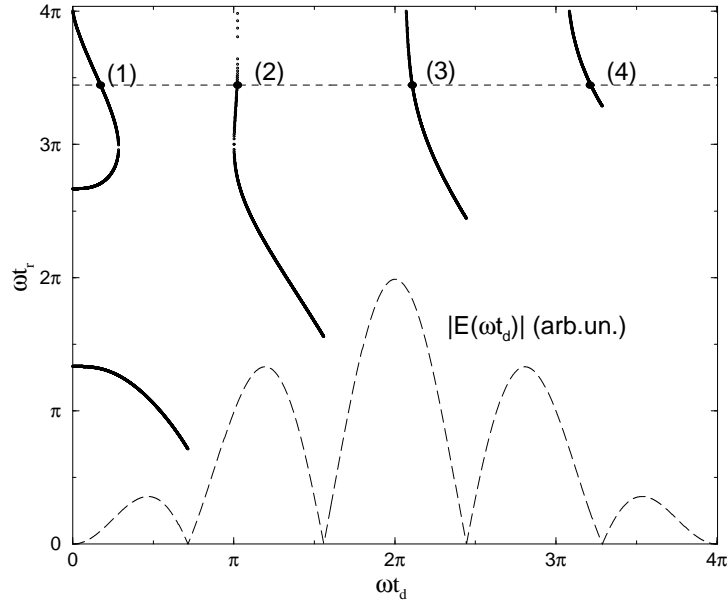


Figure 3.5: The return time t_r as a function of the detachment time t_i for a two-cycle \sin^2 laser field, with wavelength of 800 nm and intensity of 3.6×10^{17} W/cm². The dashed curve shows the absolute value of the electric field during the pulse (in arbitrary units).

analysis made at the end of Section 3.2. In the latter case, there are many possible values for the weak field’s delay; for each of these choices, the harmonic spectrum in the vicinity of the harmonic $\Omega = 7500$ is affected in a different way. Usually, enhancing a particular harmonic Ω results in enhancing a whole range of harmonics around Ω , if the non-dipole effects are not too large. This explains why in the left panel of Fig. 3.2, enhancing a single photon emission resulted in most of the high-energy plateau being enhanced.

The interplay between the field strength and phase of the weak field allows to select a certain trajectory among all contributing to the emission of the particular harmonic Ω and greatly reduce the contribution of the remaining ones. This way, the harmonic Ω is emitted in the form of a single attosecond pulse, which we discussed in the previous section.

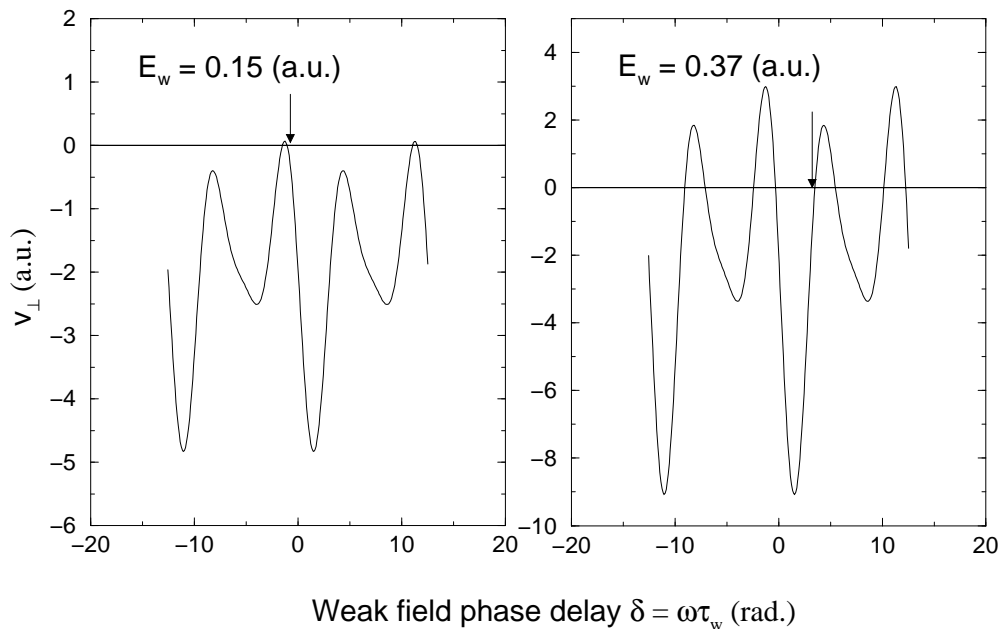


Figure 3.6: The initial speed [Eq. (3.4)] for two different field strengths, as a function of delay with respect to the driving field. From the first panel, one can see that the minimum weak field strength for the parameters chosen here (see text) can be as small as 0.15 a.u. The second panel shows results for the field amplitude chosen in Section 3.2 (the arrow points to the value of the delay chosen there); the delay can be chosen among many values for this case.

3.5 Conclusions

Typically, a number of electron trajectories contribute in a comparable way to photon emission in some frequency interval or to ATI spectra in some energy range. We have discussed a scheme whereby a second laser pulse can be used to control an individual electron trajectory: by the appropriate choice of the laser parameters, the effect of the drift induced by the magnetic field component of the pulse can be compensated for a selected trajectory, and enhanced for others, leading to the emission of a single attosecond pulse of high frequency photons. The scheme has similarities with the proposal by Corkum, Burnett and Ivanov for producing an isolated attosecond pulse, in which single returning trajectories are selected by a temporal variation of the ellipticity of the incident field [44].

Many of the issues regarding the consequences of the breakdown of the dipole approximation discussed here apply equally well to strong-field recollision processes leading to single and multiple ionization. For instance, the reduced recollision probability in the non-dipole non-relativistic regime means, as has recently been observed experimentally in nonsequential multiple ionization [45], that these processes are strongly suppressed at very high intensity. This could prohibit the experimental study of strong field recollision processes at intensities where relativistic effects become important. The selective compensation of the effect of the magnetic drift by a second laser pulse, as discussed above, may offer a way to alleviate this difficulty.

Another possible way is presented in Ref. [46], where a high-velocity beam of charged ions encounters a counter-propagating intense laser beam (this experimental setup will be available at GSI-Darmstadt where an accelerator complex will be built, capable of accelerating multi-charged ions to Lorentz factors up to about 30). Due to the high speed, in the frame reference of the ions the laser frequency increases, leading to much smaller non-dipole effects as a consequence of higher laser frequency. The effect would be the same for still ions in the laboratory frame, if higher-frequency intense laser beams would be available in practice.

Chapter 4

Above threshold ionization in atomic systems

4.1 Outline

4.1.1 Historical overview

This chapter intends to give a brief description of what is called Above Threshold Ionization (ATI) in connection to other aspects of the interaction between atoms and laser radiation. Excellent reviews on this subject, including other phenomena in intense laser fields, were given by Protopapas *et al.* [47], Joachain *et al.* [48] and, more recently, by Becker *et al.* [49].

We begin by mentioning the multiphoton (single) ionization (MPI), whereby an atom or an ion absorbs several photons from the laser field causing the weakly bound electron to ionize. In 1965, Voronov and Delone [50] observed this process using a ruby laser to induce seven-photon ionization of xenon.

In early experiments MPI was accurately modelled by the lowest-order perturbation theory (LOPT) (Fabre *et al.* [51], Petite *et al.* [52]), the n -photon ionization rate being given by

$$\Gamma_n = \sigma_n I^n$$

where n is the minimum number of photons needed for ionization, σ_n is the generalized cross section and I is the intensity of the incident light. Difficulties arise with the perturbative approach as the intensity of the incident light increases and therefore, due to strong coupling with the laser field, the atomic states can no longer be considered as unperturbed .

An important step in our understanding of MPI came along with improved experimental techniques, giving the possibility of detecting energy-resolved photoelectrons. It allowed Agostini *et al.* [53] to discover that the ejected electron could absorb photons in excess of the minimum required for ionization to occur. This became known as ‘above threshold ionization’ (ATI), and has been largely studied over the recent years.

A typical ATI photo-electron energy spectrum consists of several peaks, separated by the photon energy $\hbar\omega$. As the intensity I increases, peaks at higher energies appear, whose intensity dependence does not follow the power law according to lowest order perturbation theory (LOPT).

Another feature of ATI spectra in low frequency fields, is that as the intensity increases, the low-energy peaks reduce in magnitude, as the energies of the atomic states are Stark-shifted in the presence of the laser field. In the length gauge picture, the AC Stark shifts of the lowest bound states are smaller than those for the Rydberg and continuum states. Because the energies of the continuum states are shifted upwards relative to the lower bound states, there is a corresponding increase in the intensity-dependent ionization potential of the atom. This increase is essentially given by the electron ponderomotive energy U_p , which is the cycle-averaged kinetic energy of a quivering electron in a laser field of frequency ω . For non-relativistic velocities,

$$U_p = \frac{e^2 E_0^2}{4m\omega^2} \quad (4.1)$$

where e and m are the electron’s charge and mass, and E_0 is the electric field amplitude.

Novel structures in the ATI spectra have been identified in recent experiments.

Usually the angular distributions of electrons in the ATI spectrum produced by very intense laser fields are aligned along the axis of polarization of the applied laser field. Two groups (Yang *et al.* [54], Feldmann [55]) have shown that for noble gases a few high energy peaks may be highly structured, and in some cases feature rings 45° off the polarization axis. Theoretical investigations have shown that these rings may arise from the rescattering of the electron wavepacket from the parent ion (Kulander and Schafer [14], Paulus *et al.* [56], Lewenstein *et al.* [57]). The experiment of Paulus *et al.* [58] showed the existence of the rescattering plateau in the ATI spectrum and one- and three-dimensional theoretical simulations demonstrated that this effect is of single-atom nature. The connection with the high energy side lobes was given by Paulus, who found that the side lobes were restricted to the regions where the plateau begins.

4.1.2 Theoretical methods

The single-active-electron approximation (SAE) is widely used in atomic physics. It consists of modelling the atom in the laser field by a single electron that interacts with the laser field and is bound by an effective potential. This potential is optimized so as to reproduce the ground state and singly excited states.

In single ionization in strong fields, up to now, no effect has been identified that would reveal electron-electron correlation so that the ATI spectra are, in essence, not influenced by multi-electron correlation effects. This can be seen in a comparison made by Nandor *et al.* [2], where the experimental result is compared to the prediction of the three-dimensional time-dependent Schrödinger equation (TDSE). Very good agreement is found (see Fig. 4.1).

Although numerical solution of the one-particle TDSE in one dimension proved to be fruitful in early days to understand ATI, for further investigation the three-dimensional solution is needed. This is computationally very demand-

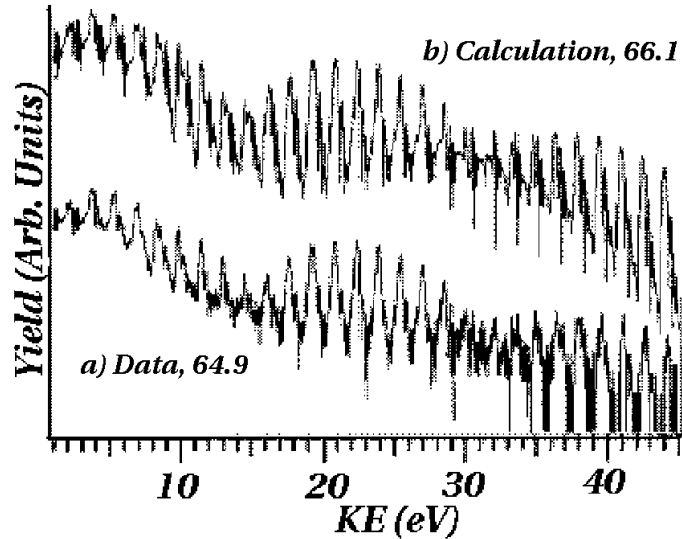


Figure 4.1: (a) Measured and (b) calculated photoelectron spectrum in argon for 800 nm, 120 fs pulses at the intensities given in TW/cm^2 in the figure ($10U_p = 39 \text{ eV}$). From Nandor *et al.* [2].

ing because of the large excursion amplitudes of free-electron motion in high-intensity low-frequency fields and therefore necessitates a large spatial grid.

The progress achieved in recent years in the intuitive understanding of the ATI is mainly due to the Simpleman's model and its refinements, a theory that analyzes the behavior of classical electron trajectories in an oscillating electric field of a laser. In its initial form [59], the Simpleman's model explains the photoelectron spectra of the so-called 'direct' electrons (electrons that don't rescatter off the atomic core) and predicts an upper limit of $2U_p$ for their kinetic energy in the case of short laser pulses. The validity of the model has been confirmed in microwaves experiments [60].

Along with new computational techniques being devised to complete the difficult numerical task, other analytic approaches apart from the Simpleman's model have been proposed. The starting point of the Keldysh-type theories, which gained a lot of attention, is the existence of an analytical solution for a free electron in a plane-wave laser field, the Volkov solution [61]. As the laser

field is of high intensity, the binding potential can be treated as a perturbation. The ground state is propagated with the operator of the laser field and projected onto the Volkov states. Further improvement of these theories include an additional interaction with the potential in order to describe the rescattering of the electron. Later, Lewenstein *et al.* decomposed the Keldysh rate into the contributions of the relevant trajectories in the spirit of Feynman's path integrals [57]. This showed that the Keldysh-type theories are related to the classical Simpleman's model picture, and indicated also that the mysterious dips in the ATI spectra are due to interference between electron's trajectories.

These methods are particularly useful for theoretical investigations in the case of stronger laser fields, longer pulses and low frequency, where a direct TDSE solution proves to be increasingly prohibitive.

4.2 Direct ionization in a stationary field

A stationary laser pulse is usually considered as a plane wave and modelled by the vector potential $\mathbf{A}(t) = A_0 \cos(\omega t)\hat{\epsilon}$, directed along the axis of polarization $\hat{\epsilon}$. The magnitude of the electric field is $E_0 = A_0/\omega$, where ω is the radiation frequency. The pulse has an infinite number of cycles with duration $T_p = 2\pi/\omega$. Because of this periodicity, we can define a rate of ionization as the ionization occurring per optical cycle. The cycle-averaged kinetic energy of an electron in such a field reads $U_p = A_0^2/4$, which is the equivalent of the expression (4.1) in atomic units.

4.2.1 The quantum-mechanical description

The transition amplitude for the direct electrons – electrons that leave the vicinity of the atom right after they have tunnelled into the continuum – is the well known Keldysh-Faisal-Reiss (KFR) amplitude [62–64]. This approximation neglects the binding potential in the propagation of the electron in

the continuum, and the laser field when the electron is bound. The transition amplitude reads [65]:

$$M_{\mathbf{p}}^{(0)} = -i \int_{-\infty}^{\infty} dt \langle \psi_{\mathbf{p}}^{Vl}(t) | V | \psi_0(t) \rangle, \quad (4.2)$$

where V denotes the atomic binding potential and the initial state is the usual hydrogenic ground state with atomic number Z and ionization energy $I_p = Z^2/2$:

$$\langle \mathbf{r} | \psi_0(t) \rangle = \frac{Z^{3/2}}{\sqrt{\pi}} e^{-Zr} e^{iI_p t}.$$

The final state is approximated with the Volkov state [see Appendix (A)] describing a charged particle with asymptotic momentum \mathbf{p} in the presence of a field with vector potential $\mathbf{A}(t)$. In the length gauge, we have:

$$\langle \mathbf{r} | \psi_{\mathbf{p}}^{Vl}(t) \rangle = \frac{e^{i\mathbf{r} \cdot [\mathbf{p} + \mathbf{A}(t)]}}{(2\pi)^{3/2}} \exp \left\{ i \int_t^{\infty} d\tau \frac{[\mathbf{p} + \mathbf{A}(\tau)]^2}{2} \right\}. \quad (4.3)$$

After some manipulations, which are detailed in Subsection 5.3.1, the integral in (4.2) can be written in the form:

$$M_{\mathbf{p}}^{(0)} = i \frac{Z^{5/2}}{\pi\sqrt{2}} \int_0^{T_p} dt \frac{\exp[iS(t)]}{S'(t)}, \quad (4.4)$$

where $T_p = n_p 2\pi/\omega$ is the duration of n_p optical cycles of the finite laser pulse. The time integration domain is changed compared to (4.2), which describes in fact a stationary field. For the stationary field case, the integral can be replaced by an integral over just one cycle of the field, with the additional condition of energy conservation; the conservation of energy for the ejected electron reads $E_p \equiv \mathbf{p}_n^2/2 = n\omega - (I_p + U_p)$, where n is the number of photons absorbed. It can be attributed to the interference of the contributions from different periods, i.e., the quantum interference is destructive, unless the energy is conserved.

We introduced, in Eq. (4.4), the quantity

$$S(t) = \frac{1}{2} \int_0^t d\tau [\mathbf{p} + \mathbf{A}(\tau)]^2 + I_p t, \quad (4.5)$$

which is the modified classical action of a free electron with conserved canonical momentum \mathbf{p} in the field. The dependence of the action S on the \mathbf{p} variable has been dropped here for clarity.

A valuable physical insight can be drawn from Eq. (4.4) when applying the saddle point method. To find the saddles, one has to solve the equation $dS(\mathbf{p}, t)/dt = 0$, which can be done analytically for the stationary field. There are only two solutions in each laser cycle, with positive imaginary parts. Their trajectories in the complex plane are shown in Fig. 4.2.

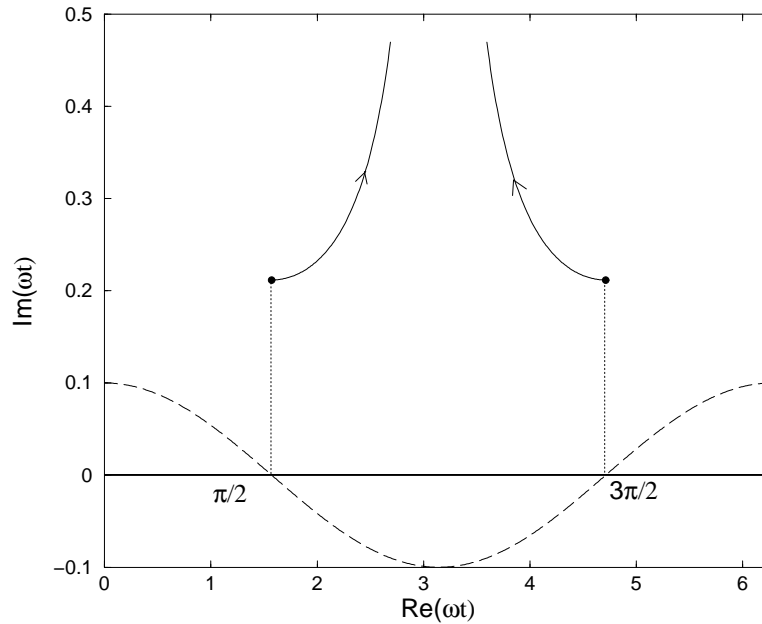


Figure 4.2: The saddle point trajectories in the complex plane for a He^+ ion irradiated by a stationary pulse with intensity $I = 10^{16} \text{ W cm}^{-2}$ and wavelength of 800 nm. The electron is emitted along the polarization axis. The dashed curve is the profile of the vector potential during one optical cycle. The circles represent the positions of the two saddles for $p=0$ and the end points of the trajectories correspond to $p = A_0$.

For low kinetic energy, the two saddles are close to the maximum of the electric field (or, alternatively, to the zeros of the vector potential) and with increasing kinetic energy, their imaginary part increases, causing the ionization amplitude to decrease exponentially. (We discuss later this aspect.)

The advantage of the saddle point method lays in the fact that the complicated integral that represents the amplitude of ionization can be reduced to a sum over just two terms. This simplification makes it easier to analyze ionization within our model, leading to a semiclassical model, which we describe in

Subsection (4.2.2).

While for the infinitely long monochromatic pulse, the ionization amplitude is invariant with respect to the transformation $\mathbf{p} \rightarrow -\mathbf{p}$, the backward-forward symmetry is no longer true for a finite pulse. This may help in determination of the absolute carrier phase (Dietrich *et al.* [66]).

4.2.2 The classical model of ionization

For a further detailed technical discussion of the amplitude integral, see Eqs. (E.1) and (E.14). The latter, which is derived by using the simplified version of the saddle point method, we reproduce below, with the appropriate pre-factors:

$$M_{\mathbf{p}}^{(0)} = -\frac{Z^{5/2}}{\sqrt{2}} \sum_{n_0=1,2} \frac{\pi \exp[iS(t_0)]}{(2I_p + p_{\perp}^2)^{1/2} |E(t_0)|} \exp \left[-\frac{1}{3} \frac{(2I_p + p_{\perp}^2)^{3/2}}{|E(t_0)|} \right]. \quad (4.6)$$

Here, p_{\perp} is the component of the electron's asymptotic momentum \mathbf{p} , perpendicular to the polarization axis. This expression provides an intuitive way

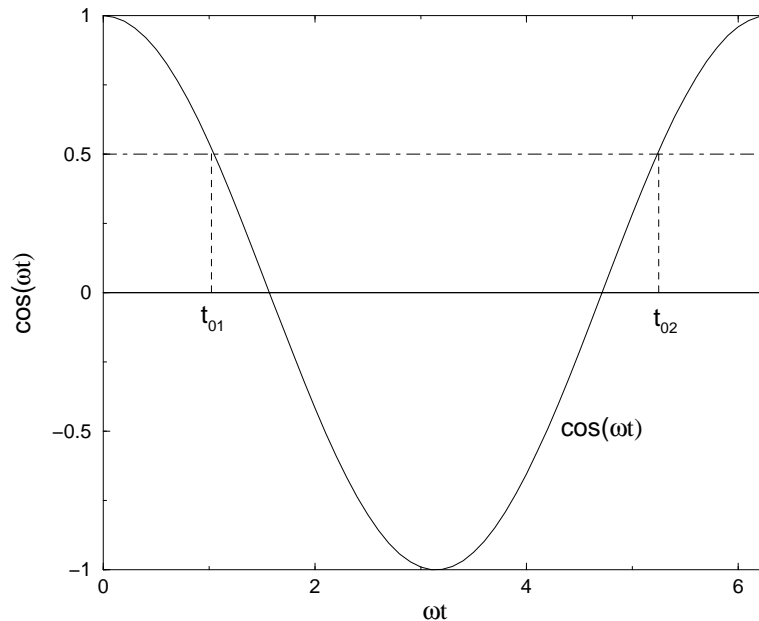


Figure 4.3: The graphical solution for the ‘birth’ times $\{t_{01}, t_{02}\}$ for a stationary field, satisfying $p_{\parallel}/A_0 + \cos(\omega t) = 0$ with $p_{\parallel} = -0.5A_0$.

to describe semiclassically the phenomenon of ionization in the Simpleman’s

model for direct ionization, in which the electron is ‘born’ in the continuum at real times t_0 given by $p_{\parallel} + A(t_0) = 0$. A graphical solution is presented in Fig. 4.3, for $p_{\parallel} = -0.5A_0$.

The condition states that the electron is ‘born’ with zero kinetic energy along the polarization axis and also sets a classical cutoff value for this energy: a solution t_0 exists only if $p_{\parallel} \leq A_0 \rightarrow E_{p_{\parallel}} \equiv \mathbf{p}_{\parallel}^2/2 \leq A_0^2/2$.

After ionization, the second step of the classical model is the evolution of the electron in the laser field. As the electron’s oscillation amplitude is much larger than the atomic distances, the influence of the binding potential can be ignored. For a given vector potential $\mathbf{A}(t)$ and a canonical momentum \mathbf{p} , which is conserved, the electron’s velocity reads:

$$\mathbf{v}(t) = \mathbf{p} + \mathbf{A}(t). \quad (4.7)$$

The velocity consists of a constant term $\mathbf{p} = -\mathbf{A}(t_0)$, which is the drift momentum measured at the detector, and an oscillating term. The kinetic energy of the electron, averaged over a laser field period T_p , is:

$$E_p \equiv \frac{\langle \mathbf{v}^2(t) \rangle_{T_p}}{2} = \frac{\mathbf{p}^2}{2} + \frac{\langle \mathbf{A}^2(t) \rangle_{T_p}}{2} \equiv E_{drift} + U_p. \quad (4.8)$$

The ponderomotive energy is often employed to characterize the laser intensity. Now, we can re-write the classical cutoff for the energy of direct electrons as $E_p \leq 2U_p$. In the quantal model, this bound is softened. However, it is useful as a guideline in the analysis of experimental spectra.

Of the two electrons, born at times t_{01} or t_{02} as depicted in Fig. 4.3, one keeps moving directly away from the atom, never crossing the atomic core, while the other starts moving in the opposite direction, turns around at a later time crossing the atomic core, to acquire in the end the same drift momentum as the first electron. The two different types of trajectories could relate to the ‘direct’ and ‘indirect’ wavepackets of de Bohan *et al.* in Ref. [4]. The emission of the electron at each of the two ionization times t_0 is weighted with a probability

containing the real exponential factor

$$\exp \left[-\frac{1}{3} \frac{(2I_p + p_\perp^2)^{3/2}}{|E(t_0)|} \right].$$

The factor decreases with p_\perp , so that the probability of ejection with high velocities in a direction perpendicular to the polarization direction is exponentially small. This term was derived by Delone and Krainov [67].

We note that the terms in the sum (4.6) are in the form of a real amplitude (containing the exponentially decreasing factor) and a complex phase factor $\exp[iS(t_0)]$. Because of the symmetry of the pulse, the real factors are the same for the two birth times and they can be factorized; this way, the phase terms add and become responsible for interference in the energy spectrum, creating a beat pattern. Because of its sensitive dependence on the laser intensity, which is not very well controlled in an experiment, the beat pattern is usually washed out.

Apart from the exponentially decreasing term, the other real pre-factors can differ from one expression for the ionization amplitude to another (depending on whether we use the length gauge or velocity gauge). What is common to all these formulations is the exponentially decreasing term and the phase factor.

4.2.3 Interferences of direct electrons

For a stationary field, during one optical cycle, there are two saddle points corresponding to a drift momentum \mathbf{p} . For small momenta, the two satisfy the approximate relation :

$$\cos(\omega t_{s1,2}) = \pm i\gamma, \quad (4.9)$$

where $\gamma \equiv \sqrt{2I_p}/A_0$ is the Keldysh parameter. Both complex saddles have the real part close to the moments in time when the electric field reaches the maximum value, at $T_p/4$ and $3T_p/4$ (here T_p is the duration of one laser period). The classical trajectory for an electron starting at the origin with zero initial kinetic energy is $\mathbf{r}(t) = (\mathbf{A}_0/\omega) \sin(\omega t)$. Hence, we can find the electron

positions at the two instants of detachment $t_{s1,2}$. Although the detachment times are complex, the positions are real:

$$\mathbf{r}_{1,2} \equiv \mathbf{r}(t_{s1,2}) = \pm \frac{\mathbf{A}_0}{\omega} \sqrt{1 + \gamma^2}. \quad (4.10)$$

From here, as discussed by Gribakin and Kuchiev [68], appears an intuitive two-slit interference picture for the ionization spectrum at low energies. According to this picture, the angular distribution of photoelectrons, emitted at an angle θ with respect to the polarization direction, is determined by the interference of two plane waves of wavevector $\mathbf{k} = \mathbf{p}$ emitted with a time delay $T_p/2$ from two sources separated by the distance $\mathbf{r}_1 - \mathbf{r}_2$. These points are located at the opposite sides of the atomic particle and emit the waves at an angle θ with respect to the polarization direction (see Fig. 4.4).

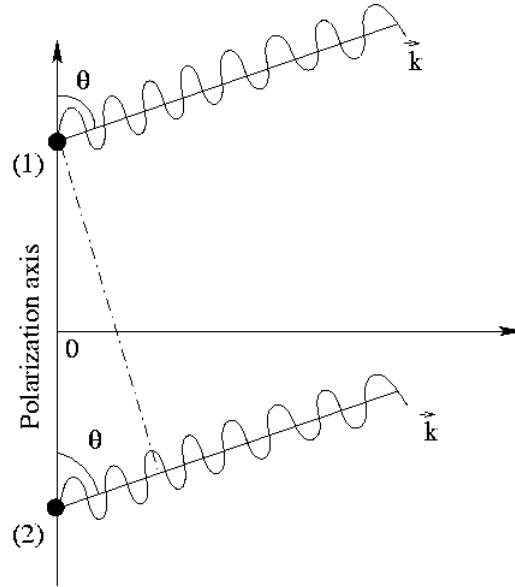


Figure 4.4: Schematic picture of the origin of interference in electron emission from two laser-induced sources. The indices (1) and (2) correspond to the two positions as in Eq. (4.10).

The phase difference is obtained by multiplying the distance between the two points by the projection of the electron momentum on the direction of the field $p \cos \theta$. As a result, one obtains for the interference term $2 \frac{A_0}{\omega} p \cos \theta \sqrt{1 + \gamma^2}$. It is remarkable that this term is identical to the one obtained from Eq. (4.6) when doing the explicit calculation [see Eq. (D.9)].

4.3 Rescattering

So far, we have presented calculations for the ‘direct’ electrons, which after the first step of ionization leave the laser focus without any additional interaction with the atomic core. In this section, we will consider the consequences of such an encounter.

4.3.1 The classical theory

The classical model becomes richer if rescattering effects are taken into account. To find the electron trajectory, we integrate its velocity [Eq. (4.7)]:

$$\mathbf{r}(t) = \int_{t_0}^t \mathbf{A}(\tau) d\tau - \mathbf{A}(t_0)(t - t_0). \quad (4.11)$$

The condition for the electron to return at a later time $t_1 > t_0$ to the atomic core is given by

$$\mathbf{r}(t_1) \equiv \int_{t_0}^{t_1} \mathbf{A}(\tau) d\tau - \mathbf{A}(t_0)(t_1 - t_0) = 0. \quad (4.12)$$

For linear polarization, it simply states that the electron moves along the polarization axis towards the origin. When it returns, one of the following can happen (Corkum, 1993 [15]):

- The electron may recombine with the core, emitting its energy plus the ionization energy as one photon. This process is responsible for the plateau of high-order harmonic generation.
- The electron may scatter inelastically off the core and dislodge a second electron. This process is now believed to be the dominant contribution to the non-sequential double ionization.
- The electron may scatter elastically, so that it can acquire drift energies much bigger than otherwise.

The kinetic energy of the electron at the time of return is

$$E_{ret} = \frac{1}{2}[A(t_1) - A(t_0)]^2. \quad (4.13)$$

Maximizing this energy together with the condition (4.12), one gets for a stationary field $E_{ret,max} = 3.17U_p$.

With the mechanism of elastic rescattering, where the energy is conserved, but the velocity can change direction, the drift energy increases. The maximal energy is obtained when the electron backscatters by 180° . A rescattering at different angle gives less gain in energy, as part of the maximal energy of the returning electron goes into motion transverse to the polarization axis. Let us assume that at the time of collision with the core the electron has the speed $v(t_1 - 0) = A(t_1) - A(t_0)$ along the polarization direction and after $v(t_1 + 0) = -[A(t_1) - A(t_0)]$. Then, from (4.7) we obtain the drift energy upon backscattering:

$$E_{bs} = \frac{1}{2}[2A(t_1) - A(t_0)]^2 \quad (4.14)$$

Maximizing (4.14) under the condition (4.12) yields $E_{bs,max} = 10.007U_p$. It is important to note that for a given final energy smaller than the cutoff energy of $10U_p$, there are two return times t_1 within one optical cycle. The two trajectories can be distinguished by the flight time of the electron.

4.3.2 The quantum-mechanical description

The generalized transition amplitude, which includes one act of rescattering, is given by [69]:

$$M_{\mathbf{p}} = - \int_{-\infty}^{\infty} dt \int_{-\infty}^t dt' \langle \psi_{\mathbf{p}}^{Vl}(t) | V U^{Vl}(t, t') V | \psi_0(t') \rangle \quad (4.15)$$

where V denotes the atomic binding potential and $U^{Vl}(t, t')$ is the Volkov time-evolution operator, describing the evolution of an electron in the presence of the laser field only. In the limit $t \rightarrow t'$, the rescattering amplitude (4.15) goes into (4.2). Hence, they must not be added. Close versions of the rescattering amplitude have been used by several authors [70–74].

Inserting the expansion of the Volkov propagator in terms of Volkov states,

$$U^{Vl}(t, t') = \int d^3\mathbf{k} |\psi_{\mathbf{k}}^{Vl}(t)\rangle \langle \psi_{\mathbf{k}}^{Vl}(t')| \quad (4.16)$$

into Eq. (4.15), the rescattering transition amplitude can be rewritten as

$$M_{\mathbf{p}} = - \int_{-\infty}^{\infty} dt \int_{-\infty}^t dt' \int d^3\mathbf{k} e^{iS_{\mathbf{p}}(t, t', \mathbf{k})} V_{\mathbf{p}\mathbf{k}} V_{\mathbf{k}\mathbf{0}}, \quad (4.17)$$

with the corresponding action given by

$$\begin{aligned} S_{\mathbf{p}}(t, t', \mathbf{k}) &= -\frac{1}{2} \int_t^{\infty} d\tau [\mathbf{p} + \mathbf{A}(\tau)]^2 \\ &\quad - \frac{1}{2} \int_{t'}^t d\tau [\mathbf{k} + \mathbf{A}(\tau)]^2 + I_p t'. \end{aligned} \quad (4.18)$$

The expressions are useful if the form factors

$$\begin{aligned} V_{\mathbf{p}\mathbf{k}} &= \langle \mathbf{p} + \mathbf{A}(t) | V | \mathbf{k} + \mathbf{A}(t) \rangle \\ &= \frac{1}{(2\pi)^3} \int d^3\mathbf{r} \exp[-i(\mathbf{p} - \mathbf{k}) \cdot \mathbf{r}] V(\mathbf{r}) \end{aligned} \quad (4.19)$$

and

$$\begin{aligned} V_{\mathbf{k}\mathbf{0}} &= \langle \mathbf{p} + \mathbf{A}(t') | V | 0 \rangle \\ &= \frac{1}{(2\pi)^3} \int d^3\mathbf{r} \exp[-i(\mathbf{k} + \mathbf{A}(t')) \cdot \mathbf{r}] V(\mathbf{r}) \psi_0(\mathbf{r}) \end{aligned} \quad (4.20)$$

can be calculated in analytical form. This is the case for the Yukawa potential $V(r) = -Z \exp(-\alpha r)/r$, when we have:

$$V_{\mathbf{p}\mathbf{k}} = -\frac{Z}{2\pi^2} \frac{1}{(\mathbf{p} - \mathbf{k})^2 + \alpha^2} \quad (4.21)$$

and

$$\begin{aligned} V_{\mathbf{k}\mathbf{0}} &= -\frac{\sqrt{2}}{\pi} \frac{Z^{5/2}}{(Z + \alpha)^2 + [\mathbf{k} + \mathbf{A}(t')]^2} \\ &= -\frac{\sqrt{2}}{\pi} \frac{Z^{5/2}}{(Z + \alpha)^2 - 2I_p}. \end{aligned} \quad (4.22)$$

The Coulomb form factors can be retrieved from Eqs. (4.21) and (4.22) in the limit $\alpha \rightarrow 0$. Since for this case $I_p = Z^2/2$, this leads to the well-known

divergence of the Coulomb form factor (4.22), when used together with the saddle point condition (4.23a).

The interpretation of the amplitude (4.17) can now be given in terms of the form factors. Firstly, the electron tunnels out from the ground state to an intermediate scattering state with free momentum \mathbf{k} [the corresponding matrix element is $V_{\mathbf{k}\mathbf{0}}$ in (4.20)]. Once in the continuum, the electron scatters under the influence of the bounding potential from the scattering state with momentum \mathbf{k} to the final state with asymptotic momentum \mathbf{p} [the matrix element is $V_{\mathbf{p}\mathbf{k}}$ in (4.19)]. The resulting amplitude is summed over all the possible intermediate momenta \mathbf{k} and integrated along the pulse duration.

Equation (4.17) simplifies by restricting the integration over the rescattering time t to only one laser cycle together with imposing the conservation of energy condition. The latter is a consequence of the interference of contributions to the ionization amplitude coming from different laser cycles, which is characteristic to the stationary field.

4.3.3 Saddle point method. Quantum orbits

For the rescattering amplitude, the saddle point equations for the integration variables t, t' and \mathbf{k} in Eq. (4.17) are:

$$[\mathbf{k} + \mathbf{A}(t')]^2 = -2I_p \quad (4.23a)$$

$$[\mathbf{p} + \mathbf{A}(t)]^2 = [\mathbf{k} + \mathbf{A}(t)]^2 \quad (4.23b)$$

$$\int_{t'}^t d\tau [\mathbf{k} + \mathbf{A}(\tau)] = 0. \quad (4.23c)$$

Their solution determine the ionization time t' , the rescattering time t , and the drift momentum \mathbf{k} of the electronic orbit between those two times, such that in the end the electron acquires the asymptotic momentum \mathbf{p} . Equations (4.23a) and (4.23b) are related to the energy conservation at the ionization time and rescattering time, respectively, and equation (4.23c) determines the intermediate electron momentum.

If we let $I_p = 0$ in Eqs. (4.23), all the variables are real and we obtain the same equations as in the Simpleman's model [75]. One very important feature of the solution for (t', t) is that they come in pairs. If we denote the 'travel time' by $\tau \equiv t - t'$, we find that for a given asymptotic momentum \mathbf{p} and for the n th travel-time interval $nT_p/2 \leq \tau \leq (n+1)T_p/2$ ($n = 1, 2, \dots$), there are two solutions having slightly different travel times. A solution (t', t, \mathbf{k}) describes an electron that starts from the origin of the binding potential at time t' with drift momentum \mathbf{k} , returns to the atomic core due to the laser field at time t , rescatters and subsequently moves away in the laser field with drift momentum \mathbf{p} . For increasing electron energy, the two solutions in a pair approach each other to finally become identical. The energy when this happens is the cutoff energy of the pair and it represents the maximum kinetic energy an electron starting with zero velocity can gain classically. (For a more detailed discussion, see [76].)

Numerically solving the system of non-linear equations (4.23) is not an easy task as the numerical routines available require a good initial guess which then they refine to the exact solution. To find this guess, one needs to systematically search the region of the plane (t', t) we are interested in. If we allow for I_p to be non-zero, the times become complex and we have to consider two extra dimensions, the imaginary parts of both times. This makes our task even more difficult.

We have been able to find a simple way to identify the real solutions for a given electron energy \mathbf{p} . We look for the return times occurring in the same cycle $\omega t \in [0, 2\pi]$ and for ionization times in all the precedent cycles $\omega t' \in [-(n+1)2\pi, -n2\pi]$, $n = 0, 1, \dots$. The solutions can be visualized graphically by using the `ImplicitPlot` command available within Mathematica [77]. In Fig. 4.5 we plot the two implicit curves given by Eqs. (4.23a) and (4.23b) with $I_p = 0$ and for two increasing values of the drift momentum \mathbf{p} ; the increasing of the momentum makes the solutions to approach each other, until they eventually coalesce at the cutoff.

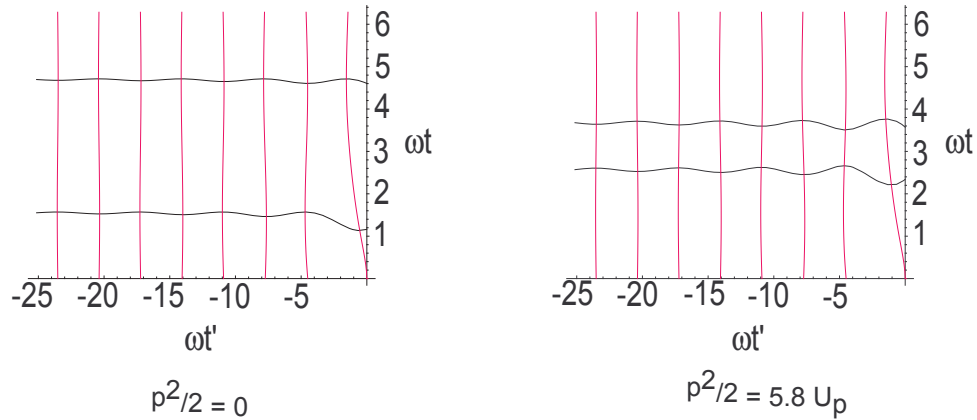


Figure 4.5: The vertical curves satisfy (4.23a) with $I_p = 0$ and the horizontal ones (4.23b) ($\mathbf{k} \neq \mathbf{p}$). Therefore, the intersection points give the solutions for the trajectories corresponding to final drift momentum $\mathbf{p} = 0$ (left panel) and $p^2/2 = 5.8U_p$ (right panel, with \mathbf{p} in the polarization direction).

It is obvious from Eq. (4.23a) that as long as $I_p \neq 0$, the times t, t' and the momentum \mathbf{k} are complex. Physically, the fact that t' is complex means that the ionization takes place via a tunneling process. Regardless of the electron energy, the orbits are now complex. These are often called quantum orbits or quantum trajectories. Unlike their real counterparts, after the cutoff they do not disappear, but their real parts remain essentially frozen and the imaginary parts quickly increase. Two typical pairs of quantum orbits are displayed in Fig. 4.6.

Both ionization and rescattering times depend on the ionization energy and the photo-electron momentum \mathbf{p} , but not on the shape of the potential $V(r)$, which enters the transition amplitude only by the form factors (4.21) and (4.22). It is to be expected that for high energy electrons, their spectrum would not be much influenced by the binding potential. This was confirmed by the numerical experiments within the SFA.

Within the saddle-point approximation, the amplitude (4.17) can be approxi-

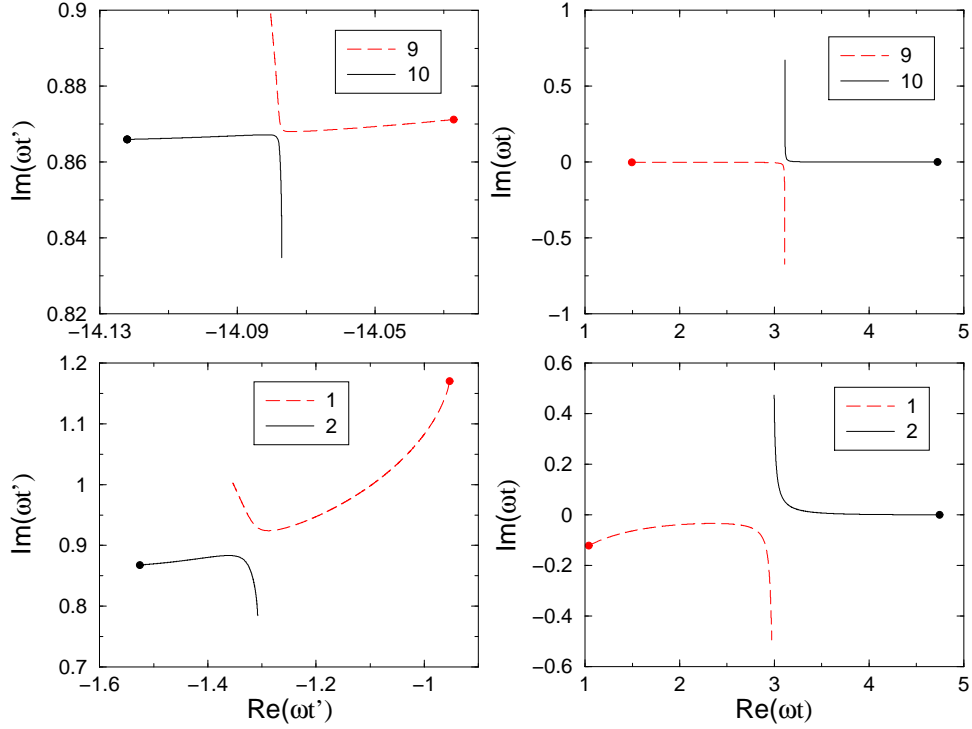


Figure 4.6: Saddle points for scattering along the polarization axis for a Keldysh parameter $\gamma = 1.11$ and $\mathbf{p} = 0$. The labels refer to the fact that the pairs (1,2) and (9,10) are ordered as a function of the increasing travel time $t - t'$. The circles correspond to $p = 0$ and the trajectories end at $\mathbf{p}^2/2 = 10U_p$.

ated by:

$$M_{\mathbf{p}} \approx \sum_s A_s \exp(iS_s) \quad (4.24a)$$

$$S_s = S_{\mathbf{p}}(t_s, t'_s) \quad (4.24b)$$

$$A_s = (2\pi i)^{5/2} \frac{V_{\mathbf{p}\mathbf{k}}(t_s, t'_s) V_{\mathbf{k}(t_s, t'_s)0}}{\sqrt{|\det S''_{\mathbf{p}}(t, t')|_s}}, \quad (4.24c)$$

where the index s runs over the relevant saddle points and $\det S''_{\mathbf{p}}(t, t')|_s$ is the five-dimensional matrix of the second derivative of the action (4.18) evaluated at the solutions of the saddle point equations (4.23). To avoid including the contribution of the direct electrons, we choose to sum only those pairs of solutions for which the travel time is bigger than half of the laser period. This way, we select only the rescattering trajectories.

The saddle point method allows one to calculate the rescattering amplitude,

avoiding the five dimensional integral present in its definition, which is a considerable simplification. This comes at the expense of solving a system of non-linear, complex equations and dealing with the so-called Stokes transition phenomenon encountered when applying the saddle point method. The Stokes transition is described in the following.

4.3.4 The saddle point uniform approximation

Upon approach to the classical cutoff, the two solutions that make up a pair come very close to each other. As an example, this is illustrated in Fig. 4.6. On the other hand, the saddle point approximation (4.23) treats different saddles as independent. As mentioned in [65] and the references therein, this leads to a qualitative breakdown of the standard saddle point approximation near the cutoff of any pair of solutions, mainly for two reasons: (i) This approximation can overestimate the saddle contribution to the transition amplitude by several orders of magnitude (and can actually diverge if both saddle coalesce). (ii) The usual procedure to avoid the problems described in (i) is to drop, after the cutoff, the spurious saddle (the saddle whose contribution increases exponentially after the cutoff – this is the Stokes phenomenon) by requiring a minimal discontinuity of the transition amplitude. Still, a discontinuity remains visible in the spectrum and it can still affect quantitatively the results in an undesirable manner.

The remedy offered by the asymptotic expansion theory comes in the form of the uniform approximation. To improve the expansion of the action function in the neighborhood of the two saddles in the pair, one needs to include higher orders in the coordinate dependence and to take the resulting integrals as the collective contribution of both saddles. The final expression can be cast in a simple form, which uses the same information as the simple saddle point method and this has been done in [65]. The uniform approximation for the case of two close saddles i and j using the Airy function and its derivative

reads:

$$M_{i+j} = (6\pi S_-)^{1/2} \exp(iS_+ + i\pi/4) \times \left[\frac{A_-}{\sqrt{z}} \text{Ai}(-z) + i \frac{A_+}{z} \text{Ai}'(-z) \right], \quad (4.25)$$

where $z = (3S_-/2)^{2/3}$ and the other quantities are:

$$\begin{aligned} 2S_{\pm} &= S_i \pm S_j \\ 2A_{\pm} &= A_i \pm iA_j. \end{aligned} \quad (4.26)$$

The subscript i denotes the first saddle in the ordered pair, whose contribution does not increase after the Stokes transition. The uniform contribution given in (4.25) appears as given in [78]. Another, equivalent version, using the Bessel functions is given in [65]. It can be shown that for $|S_-|$ large (i.e., the saddle points can be treated as independent), (4.25) reduces to (4.24). Also, due to the asymptotic properties of the Airy function for large arguments, the Stokes transition at the classical cutoff is automatically built into the uniform approximation. Notably, the uniform approximation is of the same simplicity as the usual saddle point formula.

By using the uniform approximation, we calculate here the rescattering amplitude for the case of a zero-range potential (see [65], Section VI). We choose the parameters such that we have $U_p/\omega = 3.58$, $\omega = 0.05695$ (800 nm) and a ground-state energy of $E_0 = -0.5$ a.u. The calculation is done for emission along the polarization axis.

The output of the calculation is shown in Fig. 4.7, where we can compare the relative magnitudes of the direct ionization and rescattering term with respect to the full amplitude; the difference can be as much as four orders of magnitude. Also, it is important to note that there is an energy interval (between $5U_p$ and $6U_p$) where the direct contribution is of the same order of magnitude as the rescattering, so that interference effects can occur.

One other aspect is the cutoff region in the rescattering spectrum, which is around the value of $10U_p$ in electron drift energy, after which the magnitude

decreases exponentially. This comes as a confirmation of the intuitive results obtained in the classical model of the rescattering discussed in Subsection 4.3.1.

Had we used the usual saddle point method, due to the Stokes transition not being taken into account properly, cusps would have appeared in the spectrum, with up to an order of height in magnitude, thus significantly altering the spectrum. For more details see Fig. 2(a) in [65], where the authors also compare the saddle point results to the exact results and find very good agreement.

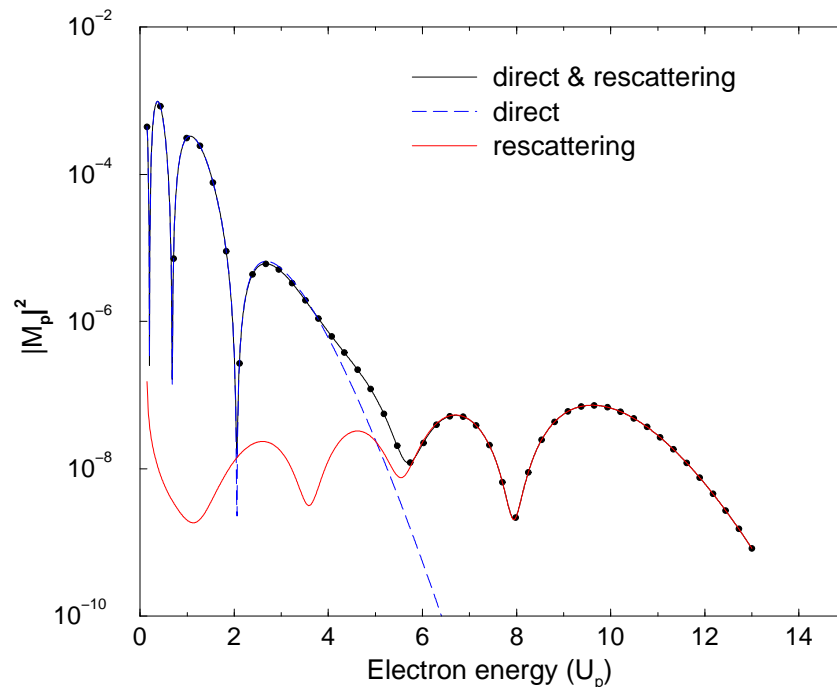


Figure 4.7: Direct and rescattering amplitudes for a zero-range binding potential with $U_p/\omega = 3.58$, at 800 nm and a ground state energy $I_p = 0.5$. The spectrum is in the laser polarization direction and the pulse has a \sin^2 envelope with zero absolute phase. The circles correspond to the ATI peaks. For the rescattering plateau, only the first five pairs of saddle points have been included.

To assess the importance of each pair of trajectories, we plotted in Fig. 4.8 the squared amplitude for the first five pairs. The (1,2) pair's contribution comes from the saddles whose trajectories are depicted in Fig. 4.6. This electron trajectories described by this pair have the smallest travel time. The cutoff for this pair is about $10U_p$ and this is the only pair contributing for the end

of the high energy plateau. The other pairs have smaller cutoffs and they contribute to different energy intervals with a decreasing magnitude. Note that the interference pattern for each pair has a different characteristic scale and that in the total contribution this interference effects average over, giving a much smoother interference pattern.

The last pair considered here is (9,10) and its saddles trajectories are shown in Fig. 4.6. Because of the longer travel time for this pair, the contribution to the rescattering plateau is the smallest compared to the other pairs.

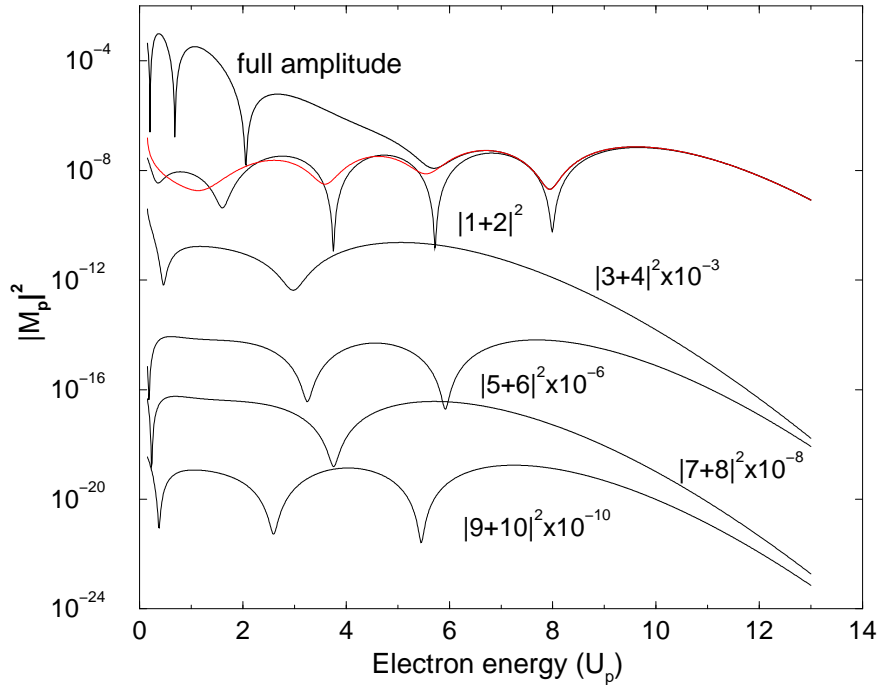


Figure 4.8: Scattering contributions for the first five saddle point pairs. The physical parameters are the same as in Fig. 4.7. The contributions have been displaced for visual convenience. The red curve shows the contribution of all the five pairs.

The Stokes phenomenon is well represented for the (1,2) pair if one looks at the high energy part, around $10U_p$. If before the cutoff there is still an interference pattern given by the two saddles contributing together to the pair amplitude, after the cutoff one of the saddles has to be dropped, and the contribution shows a smooth decay, as it originates now from only one saddle.

4.3.5 Direct- and rescattered-electrons interference

For linear polarization, in the tunneling regime there is a short energy interval where direct and rescattered electrons are emitted with comparable yields and hence can interfere with significant contrast. For elliptical polarization, the yield of rescattered electrons decreases faster while the yield of the direct electrons is less dependent on ellipticity. Consequently, the energy range for interfering can be broader. For more details, see the review of Kopold and Becker [79]. The interferences have been observed experimentally [80].

4.4 Conclusions

This chapter gives a brief introduction to the theoretical treatment of Above Threshold Ionization (ATI) within the Strong Field Approximation (SFA) model. The relevant approaches along these lines encountered in the literature are presented and illustrated with specific study cases.

We focus separately on describing the direct ionization both quantum-mechanically and classically. The classical description relies on the Simpleman's model and its success in developing an intuitive physical picture is underlined and sustained with experimental proofs. Especially, it predicts the cutoff for the kinetic energy of an ejected electron. The quantum description belongs to the widely used Keldysh-type expressions. Here, we show a particular version of it and a more general discussion is presented in the next chapter. Although we analyze the case of a stationary laser field, many features extend also to finite pulses, like the interference patterns due to beating among the different quantum trajectories.

The second part of the present review concerns the phenomenon of rescattering of the electron off the atomic core. The quantum treatment is an extension of the Keldysh-like amplitude by taking into account one more interaction of the ejected electron with the core. This is shown to explain the rescattering

plateau in the ejected electron energy spectra, seen in experiments.

The rescattering amplitude can be approximated by using the saddle point method. This leads formally to a description in terms of complex quantum orbits, much similar to Feynman's path integral. It seems however that there is a lot of physical reality associated with these trajectories. Their real parts are almost identical to the real classical trajectories of the Simpleman's model. The predictive power of this model is remarkable. For example, it has been demonstrated in the case of two-color harmonic generation by comparing the results from an integration of time-dependent Schrödinger equation with the Simpleman's model [81]. The return times predicted by the Simpleman's model exactly reflects in the temporal structure of the harmonic spectrum. The same kind of agreement holds also in the case of ATI in the way that one can identify groups of electron trajectories contributing to the ionization spectrum in a certain energy range.

Another advantage of the quantum orbits approach is that it allows for quick quantitative results, unlike solving the Schrödinger equation numerically, which for high intensities can reach today's computational limits. To be able to run quick simulations means that one can study a broad domain of intensities or laser frequencies and draw conclusions for further research or analysis of experiments.

The biggest advantage of the quantum orbits description is that it allows us to describe an otherwise difficult phenomenon in terms of a few electron trajectories. The interferences between these trajectories are responsible for the interference patterns in the ATI spectra, observed experimentally. An important conclusion is that manipulation of quantum orbits opens the gate to control spectral features.

Chapter 5

Strong Field Approximation (SFA)

5.1 Outline

Whereas the previous chapter presents the Keldysh theory [62–64] as the backbone of a compact theoretical description of ionization giving some insights of the process. In this chapter, we focus more on the theoretical aspects of this approximation, with the purpose to set the basis for the work on ionization in short pulses presented in Chapter 6.

The usual Keldysh amplitude satisfactorily accounts for a multitude of features of the electron spectra of ATI for low electron energies. Within the strong field approximation (SFA), good agreement has been found with experimental data of strong field ionization of helium [82, 83]. This data did not extend to sufficiently high electron energies to display the rescattering plateau, nor did the up to date theory include the rescattering. The new experimental techniques allowed for a dramatic improvement of the electron counting statistics and, as a result, measurements were able to detect ejected electrons with energies exceeding $10U_p$ (the classical cutoff of the electron energy spectrum owing to rescattering [75]).

The rescattering has been measured for helium at a laser intensity around 10^{15}

W/cm^2 by Walker *et al.* [84]. The data showed on a logarithmic scale the presence of an extended plateau at high electron energies, not described by the initial Keldysh theory. The next step in modifying the Keldysh theory to include the rescattering was made by Lohr *et al.* [69], whose model explained the rescattering plateau and was found to be in good agreement with the measured experimental data.

In the next sections, expressions for the ionization amplitude encountered in the literature are reviewed and their theoretical justification is highlighted. As emphasized in the previous chapter, the literature mainly discusses the case of a stationary laser field. However, the case of the short pulses requires the consideration of other aspects of the calculation, such as boundary terms (BT), directly linked to the way the turn on and off of the laser electric field is modelled by the theory (see Appendix E.2.2). When they are not properly treated, the BT are shown to induce spurious features in the description of ionization.

To summarize, Section 5.2 extends the Keldysh theory by including the rescattering term, following the work of Lohr *et al.* in [69]. In Section 5.3 we present the Keldysh expression in the context of short laser pulses by introducing the boundary terms. The importance of their correct treatment in calculations is illustrated with specific examples and the first order BT are calculated. We propose here a simplification of the Keldysh ionization amplitude, based on the properties of the Volkov solutions for which we find a unified way to write them for both the velocity (V) and length (L) gauge [Appendix A, Eq. (A.5)]. The general expressions of the Keldysh ionization amplitude are then particularized for the velocity and length gauge. An important remark on the proper definition of the vector potential $A(t)$ is made in Subsection 5.3.2.

The improved version of the Keldysh amplitude, given by Krainov [85], is examined in Subsection 5.3.3 and its detailed application to the stationary field presented in Section 5.4. These expressions are further calculated analytically in Section 5.5 (for the velocity gauge form) and in Section 5.6 (for the length

form). Although the techniques are the ones commonly used in the literature for such integrals, we give here their complete form, including the correct pre-factors of the integrals; the latter are often skipped by many authors, on the basis that the main dependence of the ionization integrals lies in the exponential dependence and the pre-factors are important only for the actual numerical calculation of the rates. Some of the methods used in other context (e.g., for harmonic generation, see Appendix A in [86]) are adapted here to calculate analytically the ionization amplitudes, where possible [Eq. (5.42)].

Finally, we present a new way to analyze the validity domain for a modified version of the velocity gauge (V) amplitude, used by A Becker *et al.* [87] to successfully reproduce experimental data.

In the last section, we compare the predictions for the ionization rate for all the amplitudes discussed previously and show their agreement relative to the cycle averaged exact static rates. The relevance of the Keldysh adiabaticity parameter γ is illustrated.

5.2 The direct and re-scattering ionization amplitudes

We proceed following the familiar Keldysh approach. The matrix element for ionization from the ground state $|\psi_0(t)\rangle$ of an atom with binding potential V into a scattering state $|\psi_{\mathbf{p}}(t)\rangle$, with asymptotic momentum \mathbf{p} is:

$$M_{\mathbf{p}} = \lim_{t \rightarrow \infty, t' \rightarrow -\infty} \langle \psi_{\mathbf{p}}(t) | U(t, t') | \psi_0(t') \rangle, \quad (5.1)$$

where the limit process has been extended to $\pm\infty$, keeping in mind the case of a stationary laser pulse. For the temporally finite pulses, the limit process is unnecessary, and the values for t' and t correspond to the beginning and the end of the pulse.

The operator $U(t, t')$ is the time-evolution operator of the atom in the presence of the external laser field. It satisfies an integral equation which yields an

expansion with respect to the interaction hamiltonian $H_i(t)$ with the external field:

$$U(t, t') = U_a(t, t') - i \int_{t'}^t d\tau U(t, \tau) H_i(\tau) U_a(\tau, t'). \quad (5.2)$$

The interaction hamiltonian for an electron with an external field has different forms, depending on the gauge one uses. For the length gauge, it reads:

$$H_i(t) = \mathbf{E}(t) \cdot \mathbf{r}, \quad (\text{length gauge})$$

and for the velocity gauge:

$$H_i(t) = -i \nabla \cdot \mathbf{A}(t) + \frac{\mathbf{A}^2(t)}{2} \quad (\text{velocity gauge}).$$

The $U_a(t, t')$ term in (5.2) is the time-evolution operator for an electron interacting with the nucleus, with the hamiltonian:

$$H_a = -\frac{\nabla^2}{2} + V \equiv H_0 + V.$$

(We denote by H_0 the hamiltonian of a free particle.)

Using the integral equation for $U(t, t')$, one gets for the ionization matrix element:

$$M_{\mathbf{p}} = \lim_{t \rightarrow \infty, t' \rightarrow -\infty} [\langle \psi_{\mathbf{p}}(t) | \psi_0(t) \rangle - i \int_{t'}^t d\tau \langle \psi_{\mathbf{p}}(t) | U(t, \tau) H_i(\tau) | \psi_0(\tau) \rangle] \quad (5.3)$$

and due to the orthogonality of the scattering state and the ground state, the matrix element becomes:

$$M_{\mathbf{p}} = -i \lim_{t \rightarrow \infty, t' \rightarrow -\infty} \int_{t'}^t d\tau \langle \psi_{\mathbf{p}}(t) | U(t, \tau) H_i(\tau) | \psi_0(\tau) \rangle. \quad (5.4)$$

In addition, we have another integral equation for $U(t, t')$, written as an expansion in terms of the binding potential V :

$$U(t, t') = U_f(t, t') - i \int_{t'}^t d\tau U_f(t, \tau) V U(\tau, t'). \quad (5.5)$$

The $U_f(t, t')$ operator is the time-evolution operator for a free electron in an external field, also referred to as the Volkov operator. It can be expanded

over the Volkov wavefunctions base, as in Eq. (4.16), and its corresponding hamiltonian is

$$H_f(t) = H_0 + H_i(t).$$

So far, no approximation has been made. In the strong field picture, one uses the expansion (5.5) with the binding potential as the expansion parameter. Substituting the first order term for $U(t, t')$ from (5.5) into (5.4) and replacing the exact scattering state $|\psi_{\mathbf{p}}(t)\rangle$ with the Volkov plane wave $|\psi_{\mathbf{p}}^V(t)\rangle$, gives the usual Keldysh amplitude for direct ionization:

$$M_{\mathbf{p}}^{(0)} = -i \lim_{t \rightarrow \infty, t' \rightarrow -\infty} \int_{t'}^t d\tau \langle \psi_{\mathbf{p}}^V(\tau) | H_i(\tau) | \psi_0(\tau) \rangle. \quad (5.6)$$

Further manipulations using the relation that $H_i(t) = H_f(t) - H_a + V$ yield:

$$\begin{aligned} M_{\mathbf{p}}^{(0)} &= -i \lim_{t \rightarrow \infty, t' \rightarrow -\infty} \int_{t'}^t d\tau \langle \psi_{\mathbf{p}}^V(\tau) | H_f(\tau) - H_a + V | \psi_0(\tau) \rangle \\ &= -i \lim_{t \rightarrow \infty, t' \rightarrow -\infty} \int_{t'}^t d\tau \langle \psi_{\mathbf{p}}^V(\tau) | -i \overleftarrow{\frac{\partial}{\partial \tau}} + i \overrightarrow{\frac{\partial}{\partial \tau}} + V | \psi_0(\tau) \rangle, \end{aligned} \quad (5.7)$$

which, up to a boundary term, gives the equivalent of (5.6):

$$M_{\mathbf{p}}^{(0)} = -i \lim_{t \rightarrow \infty, t' \rightarrow -\infty} \int_{t'}^t d\tau \langle \psi_{\mathbf{p}}^V(\tau) | V | \psi_0(\tau) \rangle. \quad (5.8)$$

This particular form is most suited for calculations involving short range potentials, because the potential V explicitly appears in the matrix element. A thorough investigation of this type of expansion, involving the binding potential, is done in [88].

Using the integral equation (5.5), with $U(t, t')$ in the right term replaced by the free field time-evolution operator $U_f(t, t')$, the next order correction to the ionization matrix element in terms of the binding potential V is:

$$M_{\mathbf{p}}^{(1)} = - \lim_{t \rightarrow \infty, t' \rightarrow -\infty} \int_{t'}^t d\tau \int_{\tau}^t d\tau_1 \langle \psi_{\mathbf{p}}(\tau_1) | V U_f(\tau_1, \tau) H_i(\tau) | \psi_0(\tau) \rangle \quad (5.9)$$

The ionization matrix element reads now

$$M_{\mathbf{p}} \approx M_{\mathbf{p}}^{(0)} + M_{\mathbf{p}}^{(1)}.$$

In what follows, we drop the limit process in (5.9). The limit process applies only to a stationary laser field for which, along with the conservation of energy condition, the rescattering time t can be restricted to the interval $[0, T_p]$. Here, T_p is the field period. For a finite pulse, we take the integration over t in the interval $[0, T_p]$ and for the ionization time $t' \in [0, t]$; T_p is the pulse temporal duration. (We assume that the pulse lasts from the time $t_i = 0$ to a time $t_f = T_p$, such that the magnetic vector potential $\mathbf{A}(t)$ and the electric field $\mathbf{E}(t)$ are both negligible for $t \leq t_i$ and $t \geq T_p$.)

5.3 Direct ionization amplitude

From Eq. (5.6) and using the explicit form of the Volkov solution (A.4), we obtain after an integration by parts:

$$M_{\mathbf{p}}^{(0)} = -\langle \psi_{\mathbf{p}}^V(\tau) | \psi_0(\tau) \rangle \Big|_0^{T_p} + i \int_0^{T_p} d\tau \langle \psi_{\mathbf{p}}^V(\tau) | I_p + \frac{[\mathbf{\Pi}_{\mathbf{p}}^V(\tau)]^2}{2} | \psi_0(\tau) \rangle. \quad (5.10)$$

The $\mathbf{\Pi}_{\mathbf{p}}^V(t)$ is the momentum eigenvalue of the Volkov solution

$$\langle \mathbf{r} | \psi_{\mathbf{p}}^V(t) \rangle = (2\pi)^{-3/2} \exp \left\{ i \mathbf{\Pi}_{\mathbf{p}}^V(t) \cdot \mathbf{r} - \frac{i}{2} \int^t [\mathbf{p} + \mathbf{A}(\tau)]^2 d\tau \right\}.$$

For a hydrogenic ground state $|\psi_0(t)\rangle$ with ionization energy I_p , we have for the matrix element:

$$\langle \psi_{\mathbf{p}}^V(t) | \psi_0(t) \rangle = \frac{(2I_p)^{5/4}}{\pi\sqrt{2}} \frac{\exp[iS(t)]}{[\mathbf{\Pi}_{\mathbf{p}}^V(t)^2/2 + I_p]^2}, \quad (5.11)$$

with $S(t)$ the modified classical action (4.5), depending also on the asymptotic momentum \mathbf{p} present in the definition of $\mathbf{\Pi}_{\mathbf{p}}^V$. Finally, we write the direct ionization amplitude as:

$$M_{\mathbf{p}}^{(0)} = i \frac{(2I_p)^{5/4}}{\pi\sqrt{2}} \left(i \frac{\exp[iS(\tau)]}{[\mathbf{\Pi}_{\mathbf{p}}^V(\tau)^2/2 + I_p]^2} \Big|_0^{T_p} + \int_0^{T_p} d\tau \frac{\exp[iS(\tau)]}{\mathbf{\Pi}_{\mathbf{p}}^V(\tau)^2/2 + I_p} \right) \quad (5.12)$$

and by extracting the first boundary contribution from the integral [see (E.2.2)], we can write the first order boundary term of the direct ionization amplitude

as:

$$b^{(0)} = \frac{(2I_p)^{5/4}}{\pi\sqrt{2}} \frac{\exp[iS(\tau)]}{\mathbf{\Pi}_p^V(\tau)^2/2 + I_p} \left(\frac{1}{dS(\tau)/d\tau} - \frac{1}{\mathbf{\Pi}_p^V(\tau)^2/2 + I_p} \right) \Big|_0^{T_p} \quad (5.13)$$

or, by replacing the action's derivative:

$$b^{(0)} = \frac{(2I_p)^{5/4}}{\pi\sqrt{2}} \frac{\exp[iS(\tau)]}{\mathbf{\Pi}_p^V(\tau)^2/2 + I_p} \left(\frac{1}{[\mathbf{p} + \mathbf{A}(\tau)]^2/2 + I_p} - \frac{1}{\mathbf{\Pi}_p^V(\tau)^2/2 + I_p} \right) \Big|_0^{T_p}. \quad (5.14)$$

The importance of the boundary terms is discussed in (E.2.2), and it will be further detailed for specific gauges in the following sections.

5.3.1 The length gauge direct amplitude

To analyze the direct ionization amplitude in the length gauge, we replace in (5.12) (the integral term only, we leave the boundary term for a separate discussion) the Volkov momentum eigenvalue $\mathbf{\Pi}_p^V(t)$ [see Eq. (A.5) for the definition of the Volkov momentum] with its expression in the length gauge and obtain:

$$M_{\mathbf{p}}^{(0)} = i \frac{(2I_p)^{5/4}}{\pi\sqrt{2}} \int_0^{T_p} d\tau \frac{\exp[iS(\tau)]}{[\mathbf{p} + \mathbf{A}(\tau)]^2/2 + I_p}. \quad (5.15)$$

A detailed analysis based on the saddle point method and the physical interpretation of the asymptotic results are given in Appendix E [see Eq. (E.1)]. From now on, the form of the ionization amplitude (5.15) is going to be referred to as the length gauge (L) form.

For short pulses, the boundary terms can no longer be ignored, as is possible for the case of the stationary field due to the conservation of electron energy condition. The first order boundary term (5.14) cancels in the length gauge, so we are left with next order boundary terms. These can be shown to depend on the electric field and its derivatives at the beginning and the end of the pulse. The condition for the amplitude to be well approximated by the asymptotic contribution of the saddle points only is to have the boundary contribution much smaller. This requires smooth turn-on and off of the electric field. If this condition is not satisfied, one needs to extract the boundary terms explicitly

from the numerical value of the integral. Avoiding the effects of the boundary terms has the physical content that the ionization amplitude cannot be influenced by the turn-on and off of the field. In reality, the turn-on and off is done very smoothly, unlike it is modelled by the theory used in the Keldysh approach.

5.3.2 The velocity gauge direct amplitude

Using the same path as for the length gauge, we can write the direct ionization amplitude [Eq. (5.12) – the integral term only] in the velocity gauge (less the boundary terms) by using the Volkov eigenvalue momentum given in Eq. (A.5):

$$M_{\mathbf{p}}^{(0)} = i \frac{(2I_p)^{5/4}}{\pi\sqrt{2}} \frac{1}{\mathbf{p}^2/2 + I_p} \int_0^{T_p} \exp[iS(\tau)] d\tau. \quad (5.16)$$

We are going to refer to this form as the velocity gauge form (V), discussed in detail from the asymptotic point of view in Appendix E [see Eq. (E.2)]. The first order boundary term reads:

$$b^{(0)} = \frac{(2I_p)^{5/4} \exp[iS(t)]}{\pi\sqrt{2}} \left(\frac{1}{[\mathbf{p} + \mathbf{A}(t)]^2/2 + I_p} - \frac{1}{\mathbf{p}^2/2 + I_p} \right) \Big|_0^{T_p}. \quad (5.17)$$

We note that the boundary term contribution decreases with increasing electron energy and the condition for it to cancel is $A(0) = A(T_p) \equiv 0$. In this way, we are left with next order contributions which are negligible compared to the saddle point contribution provided the electric field turns on and off smoothly at the beginning and the end of the pulse. The origin of the equality $A(0) = A(T_p)$ can be related to the condition that the electric field should have no dc component:

$$\int_0^{T_p} E(\tau) d\tau = -[A(T_p) - A(0)] = 0.$$

The other condition, that the vector potential is zero at the pulse temporal boundaries, simplifies the equations and gives some numerical advantages by cancelling the first order boundary term. This is the convention we use in our calculations. If the vector potential is nonzero at the end of the pulse, in

order for the asymptotic momentum \mathbf{p} used in the (L) and (V) form of the ionization amplitude to really describe an electron with final momentum \mathbf{p} at the detector, one has to make the substitution $\mathbf{p} \rightarrow \mathbf{p} - \mathbf{A}(T_p)$ (see Milošević *et al.* in [34]). This particular choice would make the first order BT term to be non-zero, as opposite to the more convenient choice $A(T_p) = 0$.

5.3.3 The Krainov Coulomb-corrected ionization amplitude

The Coulomb correction is calculated (see Krainov, [85]) in the framework of quasiclassical perturbation theory with respect to the Coulomb potential $V(r) = -Z/r$ (Z is the electric charge of the atomic or ionic core) by including an extra factor in the Volkov wave function:

$$I = \exp(-i \int V dt). \quad (5.18)$$

From the classical equations of motion for an electron in an external field, we have:

$$dt = dr/p = (Z^2 - 2E_0 r)^{-1/2} dr,$$

with p the electron momentum, E_0 the amplitude of the electric field amplitude and the binding energy $I_p = -Z^2/2$. The centrifugal energy, as well as the contribution of the Coulomb potential energy to the electron momentum p , are neglected. The upper limit of integration over r is the classical turning point where $p(r_0) = 0$. The lower limit of integration is the arbitrary radial coordinate, large enough compared to the radius of the atomic system considered, and where the external electromagnetic field is negligible with respect to the strength of the Coulomb interaction. This way, an asymptotic expression for the atomic wave function of the initial unperturbed state can be used.

The approach of Krainov is based on the idea of considering the Coulomb potential as a small perturbation and the motion of the electron in the sub-barrier region governed by the external field only. The correction is position-

dependent and is singular at the origin; in the amplitude (5.20), this singularity leads to an analytical result after integrating over the electron's coordinates.

In a slightly different form, the same technique was used by Perelomov and Popov in [89], whereby the authors give a correction independent of electron's position. They solve the problem of singularity by employing a matching procedure between the wavefunction close to the end of the barrier, where the semiclassical considerations apply, and the wavefunction close to the origin. Near the origin, because the external field is negligible, the wavefunction can be well approximated by that of a free atom.

After calculating the integral in (5.18), the correction reads:

$$I = \frac{2Z^2}{E_0 r}. \quad (5.19)$$

The result (5.19) is the same for linear and circular polarization of the electromagnetic field, and it is proportional to the Coulomb potential $V(r)$. This factor multiplies the Volkov wavefunction in the expressions for the direct ionization. We now obtain from (5.6):

$$M_{\mathbf{p}}^{(0)} = -i \frac{2\sqrt{2I_p}}{E_0} \int_0^{T_p} d\tau \langle \psi_{\mathbf{p}}^V(\tau) | H_i(\tau) V | \psi_0(\tau) \rangle. \quad (5.20)$$

The boundary terms are not included, in view of the previous discussions. Making use of the explicit form of the Volkov solution (Appendix A), we get:

$$M_{\mathbf{p}}^{(0)} = -i \frac{2\sqrt{2I_p}}{E_0} \int_0^{T_p} d\tau \langle \psi_{\mathbf{p}}^V(\tau) | \psi_0(\tau) \rangle [\mathbf{\Pi}_{\mathbf{p}}^V(\tau)^2/2 + I_p]^2, \quad (5.21)$$

and the final form:

$$M_{\mathbf{p}}^{(0)} = -i \frac{\sqrt{2}}{\pi E_0} (2I_p)^{7/4} \int_0^{T_p} d\tau \exp[iS(\tau)]. \quad (5.22)$$

This ionization amplitude, which includes the Coulomb correction, is going to be referred from now on as the Krainov (K) form, and the integral in its definition is the same as the integral (E.2), thoroughly analyzed in Appendix E.

One remarkable feature of Eq. (5.22) is that it does not depend on the Volkov momentum eigenvalue (A.5), and therefore is the same in both the length gauge and the velocity gauge, considered here. This is consistent with the general property that the ionization matrix elements must be invariant under gauge transformations.

In [85], Krainov shows that for a stationary field, the tunneling limit ($\gamma \rightarrow 0$, where γ is the Keldysh parameter) for the ionization rate based on Eq. (5.22), in the case of a stationary laser field, goes to the expressions of the ADK tunneling ionization rates [90], both for linear and circular polarization (note that the correct expressions of ADK tunneling rates can be found in Ref. [91], where all misprints from the original paper were corrected). The calculations are presented in detail in Appendix (D), correcting some misprints from the original article [85].

5.4 The case of the stationary field

In this section, we present the result of applying the (K) expression (5.22) for direct ionization, for a stationary field, treating explicitly the pre-factors, which are sometimes not present in the literature.

5.4.1 Linearly polarized radiation

For this, we take the external electric field of the form $\mathbf{E}_0 \cos \omega t$, whereas the magnetic vector potential is equal to $\mathbf{A}(t) = -\mathbf{E}_0 \sin \omega t / \omega$. Then Eq. (4.5) reads

$$S(t) = (p^2/2 + E_0^2/4\omega^2 + I_p)t + (p_{\parallel} E_0/\omega^2) \cos(\omega t) - (E_0^2/8\omega^3) \sin(2\omega t).$$

Here, the quantity p_{\parallel} is the electron's momentum projection along the direction of the electric field \mathbf{E}_0 . It can be easily seen that:

$$S(t + k\frac{2\pi}{\omega}) = S(t) + \frac{2\pi}{\omega} k(p^2/2 + E_0^2/4\omega^2 + I_p) \equiv S(t) + kS_0, \quad (5.23)$$

which shows that the action is a periodical function, up to a term that increases linearly with time; after k cycles, the value of the action is the same as in the first cycle plus kS_0 , with S_0 is defined in (5.23).

Taking $M_{\mathbf{p}}^{(0)}$ as the contribution to the transition amplitude of only one period of the driving field (5.22), the transition amplitude after N periods can be written as [see Eq. (5.23)] :

$$\begin{aligned} M_{\mathbf{p}}^{(0)}(N) &= M_{\mathbf{p}}^{(0)} \{1 + \exp(iS_0) + \exp(2iS_0) + \dots + \exp[i(N-1)S_0]\} \\ &= M_{\mathbf{p}}^{(0)} [1 - \exp(NiS_0)] / [1 - \exp(iS_0)]. \end{aligned} \quad (5.24)$$

Hence, the squared transition amplitude after N periods is given by:

$$W_N = |M_{\mathbf{p}}^{(0)}|^2 \left[\frac{\sin(NS_0/2)}{\sin(S_0/2)} \right]^2 \quad (5.25)$$

When $N \gg 1$, the modulating factor in (5.25) looks like in Fig. 5.1. The

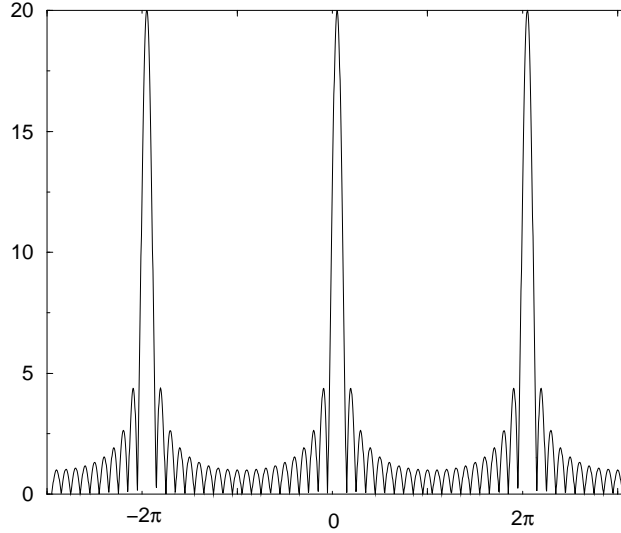


Figure 5.1: Graph of the modulating factor $\left| \frac{\sin(Nx/2)}{\sin(x/2)} \right|^2$, with $N = 20$

quantity W_N is maximal only for $S_0 = 2k\pi$, with k an arbitrary integer, and goes quickly to zero otherwise. Hence, to avoid destructive interference, we must have $S_0 = 2k\pi$, which is the same as the condition of energy conservation for the ejected electron. In this way, the conservation of energy arises because

for any other value of the electron energy not satisfying it, we would have destructive interference coming from the summed contributions of all laser cycles. With the condition satisfied, we rewrite one of the ratios of the two ‘sin’ functions as equal to $N = t/(2\pi/\omega)$ (N field periods) and use for the second identical ratio that:

$$\delta(x) = \frac{1}{2\pi} \lim_{N \rightarrow \infty} \frac{\sin(Nx/2)}{\sin(x/2)}.$$

From Eq. (5.25) we get the density of probability for ionization:

$$W_N = |M_{\mathbf{p}}^{(0)}|^2 (\omega^2 t / 2\pi) \delta(p^2/2 + E_0^2/4\omega^2 + I_p - N\omega). \quad (5.26)$$

The Dirac δ -function ensures the energy-conservation for the absorption of N photons. Dividing by time t, multiplying by the density of the final states $d^3\mathbf{p}$ and integrating over the electron momentum \mathbf{p} , we obtain the general expression for the energy and angular distribution of the electrons ejected by the ionization of the linearly polarized electromagnetic field after absorption of N photons:

$$\frac{dw_N}{d\Omega_{\hat{p}}} = \frac{Z^7 \omega^2}{E_0^2 \pi^3} p_N \left| \int_0^{2\pi/\omega} dt \exp[iS(t)] \right|^2. \quad (5.27)$$

Thus, we have obtained the general formula for the ionization rate of a linearly polarized field for arbitrary values of the field strength E_0 , in the Krainov Coulomb corrected formulation [Eq. (5.22)]; it takes into account the Coulomb correction in the tunneling stage.

5.4.2 Circularly polarized radiation

The difference from the case of linear polarization is the different expression of the action due to changing the expression of the vector potential:

$$\mathbf{A}(t) = \frac{E_0}{\omega} (\hat{\mathbf{e}}_x \cos \omega t + \hat{\mathbf{e}}_y \sin \omega t),$$

with $\hat{\mathbf{e}}_x$ and $\hat{\mathbf{e}}_y$ the unit vectors in the polarization plane of the electromagnetic field. Following Krainov [85], we take the momentum \mathbf{p} at an angle θ with the

polarization axis Oz and its projection onto the polarization plane coincides with axis Ox .

From Eq. (4.5) we obtain:

$$S = \left(\frac{p^2}{2} + \frac{E_0^2}{2\omega^2} + I_p \right) t + \frac{pF \sin \theta}{\omega^2} \sin \omega t$$

Further, with N_0 the minimum number of photons required to allow a transition to continuum $N_0 = [(E_0^2/2\omega^2 + I_p)/\omega] + 1$, the action exponentiated reads:

$$\exp[iS(t)] = \sum_{N=N_0}^{N=\infty} J_N \left(\frac{pF \sin \theta}{\omega^2} \right) \exp(i f_N t), \quad (5.28)$$

where $f_N = (p^2 - p_N^2)/2$ and $p_N = \sqrt{2(N\omega - E_0/2\omega^2 - I_p)}$. For the integral, we have

$$\begin{aligned} \int_{-\infty}^t dt \exp[iS(t)] &= \sum_N J_N \left(\frac{pF \sin \theta}{\omega^2} \right) \int_{-\infty}^t dt' e^{(i f_N + \eta)t'} = \\ &= \sum_N J_N \left(\frac{pF \sin \theta}{\omega^2} \right) \frac{e^{(i f_N + \eta)t}}{i f_N + \eta}. \end{aligned} \quad (5.29)$$

Here, $\eta \rightarrow 0$ is introduced to ensure convergence for integration in (5.29). The modulus squared differentiated with respect to time, as needed in transition amplitude per unit time, reads:

$$\frac{d}{dt} \left| \int_{-\infty}^t dt \exp[iS(t)] \right|^2 = \sum_N J_N^2 \left(\frac{pF \sin \theta}{\omega^2} \right) \frac{2\eta}{f_N^2 + \eta^2} e^{2\eta t} + \text{osc. terms} \quad (5.30)$$

Averaged over one period of the field, the oscillating terms give no contribution, and using

$$\lim_{\eta \rightarrow 0} \frac{2\eta}{x^2 + \eta^2} = 2\pi \delta(x)$$

we can write:

$$\frac{d}{dt} \left| \int_{-\infty}^t dt \exp[iS(t)] \right|^2 = 2\pi \sum_N J_N^2 \left(\frac{pF \sin \theta}{\omega^2} \right) \delta \left(\frac{p^2 - p_N^2}{2} \right). \quad (5.31)$$

Now we have all we need to derive the ionization probability per unit time averaged over one cycle from the time derivative of (5.22) and from (5.31):

$$\frac{d}{dt} |M_{\mathbf{p}}^{(0)}|^2 = \frac{4Z^7}{\pi E_0^2} \sum_{N \geq N_0} J_N^2 \left(\frac{pF \sin \theta}{\omega^2} \right) \frac{\delta(p - p_N)}{p_N}.$$

Multiplying with the density of the electron states $d^3\mathbf{p}$, we get for the ionization rate in a fixed solid angle for a circularly polarized field:

$$\frac{dw}{d\Omega_{\hat{p}}} = \frac{4Z^7}{\pi E_0^2} \sum_{N \geq N_0} p_N J_N^2 \left(\frac{p_N E_0 \sin \theta}{\omega^2} \right). \quad (5.32)$$

Going into the tunneling regime, one needs to calculate the limit of the sum in (5.32) over all the multiphoton orders. This is presented in detail in Appendix (D.2).

5.5 Analytic results for the direct ionization (velocity gauge)

This section concerns the analytical forms of the Keldysh direct ionization amplitude in the length gauge [(L) form, Eq. (5.15)] and velocity gauge [(V) form, Eq. (5.16)]. Although we discuss here the case of a stationary field, most of the methods presented can be applied to more general fields.

5.5.1 Elliptic polarization

Some calculations in this section follow the ones appearing in [87], with minor corrections [such as missing the $\text{sgn}(p_1)$ factor in Eq. (5.33)]. We consider, as in [87], a general elliptically polarized laser field described by the vector potential in the dipole approximation:

$$\mathbf{A}(t) = A_0[\hat{\epsilon}_1 \cos(\xi/2) \cos(\omega t) - \hat{\epsilon}_2 \sin(\xi/2) \sin(\omega t)],$$

where the propagation direction is chosen perpendicular to the unit polarization vectors and the ellipticity of the field ξ is in the interval $[0, \pm\pi/2]$. The signs $+/-$ correspond to right/left helicity.

The action [Eq. (4.5)] and its derivative read, after some manipulations :

$$\begin{aligned} \frac{dS(t)}{dt} = & \left(\frac{p^2}{2} + U_p + I_p \right) + U_p \cos \xi \cos(2\omega t) + \\ & + \text{sgn}(p_1) A_0 \sqrt{\left(p_1 \cos \frac{\xi}{2} \right)^2 + \left(p_2 \sin \frac{\xi}{2} \right)^2} \cos(\omega t + \chi), \end{aligned} \quad (5.33)$$

where $U_p = A_0^2/4$ is the ponderomotive energy, $\tan \chi = (p_2/p_1) \tan(\xi/2)$ and $\text{sgn}(p_1)$ is the sign of p_1 .

The action $S(t)$ can be easily obtained by integrating its derivative given by (5.33):

$$\begin{aligned} S(t) = & \left(\frac{p^2}{2} + U_p + I_p \right) t + \frac{U_p}{2\omega} \cos \xi \sin(2\omega t) + \\ & + \text{sgn}(p_1) \frac{A_0}{\omega} \sqrt{\left(p_1 \cos \frac{\xi}{2} \right)^2 + \left(p_2 \sin \frac{\xi}{2} \right)^2} \sin(\omega t + \chi). \end{aligned} \quad (5.34)$$

To simplify the expressions, we use the conservation of energy condition:

$$\frac{p_N^2}{2} + U_p + I_p = N\omega, \quad N > N_0 \quad (5.35)$$

(N_0 is the threshold number of photons) and the Jacobi-Anger expansion to get:

$$\exp[iS_N(t)] = \sum_{n=-\infty}^{\infty} \sum_{k=-\infty}^{\infty} J_n(a) J_k(b) e^{i(2n+k+N)\omega t} e^{ik\chi}, \quad (5.36)$$

with $a = \frac{U_p}{2\omega} \cos(\xi)$, $b = \text{sgn}(p_1) A_0/\omega \sqrt{\left(p_1 \cos \xi/2 \right)^2 + \left(p_2 \sin \xi/2 \right)^2}$ and $J_n(x)$ the Bessel function of the first kind.

The easiest analytical result for the transition amplitude in the case of absorption of N photons can be written in the velocity gauge [see Eq. (5.16)], by using the expansion from (5.36), in which case its integral over one cycle is zero unless $2n + k + N = 0$, so the double infinite sum is replaced by one sum:

$$M_{\mathbf{P}}^{(0)} = \frac{z^{5/2}}{\pi\sqrt{2}} \frac{(-1)^N}{p_N^2/2 + I_p} \frac{2\pi}{\omega} \sum_{n=-\infty}^{\infty} J_n(a) J_{2n+N}(b) e^{-i(2n+N)\chi} \quad (\text{velocity gauge.}) \quad (5.37)$$

In the next two subsections, we particularize Eq. (5.37) for linear and circular polarization.

5.5.2 Linear polarization

Taking $\xi = 0$ (the laser field is linearly polarized along the Ox_1 axis) in (5.37), we have for the absorption of N photons:

$$M_{\mathbf{p}}^{(0)} = \frac{z^{5/2}}{\pi\sqrt{2}} \frac{(-1)^N}{p_N^2/2 + I_p} \frac{2\pi}{\omega} \sum_{n=-\infty}^{\infty} J_n\left(\frac{U_p}{2\omega}\right) J_{2n+N}\left(\frac{A_0 p_1}{\omega}\right). \quad (5.38)$$

5.5.3 Circular polarization

With the choice $\xi = -\pi/2$ in $A(t)$, for the circularly left polarized field, the amplitude for direct ionization reads:

$$M_{\mathbf{p}}^{(0)} = \frac{z^{5/2}}{\pi\sqrt{2}} \frac{(-1)^N}{p_N^2/2 + I_p} \frac{2\pi}{\omega} J_N\left(\frac{A_0 p_{\perp} \text{sign}(p_1)}{\omega\sqrt{2}}\right) e^{-iN\chi} \quad (5.39)$$

($p_{\perp} \equiv \sqrt{p_1^2 + p_2^2}$ is the momentum perpendicular to the laser propagation direction and $\tan \chi = -p_2/p_1$). The expression (5.39) differs from the case of linear polarization (5.38), by having no summation over the Bessel functions; therefore, one expects less interference effects in the ionization spectrum for circularly polarized radiation. We show that this is indeed the case.

5.6 Analytic results for the direct ionization (length gauge)

In the length gauge, one has to deal with integrals of type (5.15), where the exponential can be written in the form of (5.36). Therefore, it remains to calculate analytically integrals of the type:

$$I_N(r) = \int_0^{2\pi/\omega} dt \frac{\exp(ir\omega t)}{[\mathbf{p}_N + \mathbf{A}(\omega t)]^2/2 + I_p}, \quad (5.40)$$

i.e., a Fourier transform [the index N refers to the conservation of energy condition (5.35)]. This could be done either numerically, based on the fact

that the Fourier components decrease exponentially with the order r (as it will be proven below), or analytically, following an idea given in the context of harmonic generation from the article of Antoine *et al.* (Appendix A in [86]).

By doing the substitution $\exp(i\omega t) = z$, the integral can be rewritten as:

$$I_N(r) = -\frac{i}{\omega} \oint \frac{z^{r-1}}{[\mathbf{p}_N + \mathbf{A}(z)]^2/2 + I_p} dz, \quad (5.41)$$

where the integration contour in the complex plane is the unit circle going around the origin counter-clockwise. In the expression of the potential, all the trigonometric functions have been expressed as a function of $e^{i\omega t}$, using the fact that $\cos x = (e^{ix} + e^{-ix})/2$ and the corresponding relation for the ‘sin’ function. From the residue theorem (with $r \geq 0$, so $z = 0$ is not a pole), the integral is :

$$I_N(r) = \frac{2\pi}{\omega} \sum_{\substack{k \\ |z_k| < 1}} \text{Res}[z_k, f(z)].$$

The function $f(z)$ is just the integrand in (5.41) and the poles are the roots of the equation:

$$\frac{dS}{dt}(z_k) = [\mathbf{p}_N + \mathbf{A}(z_k)]^2/2 + I_p = 0.$$

For general elliptical polarization, the equation is a polynomial of order four in z_k (which can be factorized for linear polarization in two second order equations); the roots can be found, but the expressions are intricate. Usually, only two roots have their modulus smaller than unity. However, for more complicated cases, reliable numerical routines are available for solving polynomial equations.

For circular polarization, the equation for finding the poles is quadratic. Using the energy conservation (5.35) and taking $\xi = -\pi/2$ in (5.33), we obtain:

$$\frac{dS}{dt}(z) = N\omega + \text{sgn}(p_1) \frac{A_0}{\sqrt{2}} p_\perp \frac{z \exp(i\chi) + \exp(-i\chi)/z}{2},$$

where $p_\perp \equiv \sqrt{p_1^2 + p_2^2}$ is the momentum perpendicular to the direction of the propagation of the laser. Another form is:

$$\frac{dS}{dt}(z) = \frac{b}{2z} (z - z_1)(z - z_2),$$

with $a = N\omega$, $b = \text{sgn}(p_1) \frac{A_0}{\sqrt{2}} p_\perp$ and:

$$z_{1,2} = \left(-\frac{a}{b} \pm \sqrt{\left(\frac{a}{b}\right)^2 - 1} \right) e^{-i\chi}.$$

Because either $|z_1| < 1$ and $|z_2| > 1$ (if $\frac{a}{b} > 1$) or $|z_2| < 1$ and $|z_1| > 1$ (if $\frac{a}{b} < -1$):

$$I_N(r) = \frac{4\pi}{b\omega} \frac{z_l^r}{z_l - z_{3-l}}, \quad r \geq 0$$

with $l = 1$ or $l = 2$ such that $|z_l| < 1$. The integral decreases exponentially with increasing r , as $\lim_{r \rightarrow \infty} z_l^r = 0$. For $r < 0$, we use analytic continuation and taking the complex conjugate of (5.40), we find :

$$I_N(r) = \frac{4\pi}{b\omega} \frac{z_l^{|r|}}{z_l - z_{3-l}}.$$

Combining (5.15) with the expansion for the action (5.36) and the result for $I_N(r)$, we obtain the ionization amplitude for a circularly polarized stationary field, in the length gauge (L):

$$M_{\mathbf{p}}^{(0)} = i \frac{(2I_p)^{5/4}}{\pi\sqrt{2}} \sum_{k=-\infty}^{\infty} J_k[\text{sgn}(p_1) \frac{A_0}{\sqrt{2}} p_\perp] I_N(k + N) e^{ik\chi}, \quad (5.42)$$

with $\tan \chi = -p_2/p_1$.

5.7 A modified velocity gauge amplitude

In [87], A Becker *et al.* used a simplified version of the Coulomb correction proposed by Krainov [85]. The simplification, which is shown to successfully describe a large set of experimental results, is simply a multiplicative correction by the factor

$$C^2(Z, I_p, E_0) = \left(\frac{2k_B I_p}{E_0} \right)^{2Z/k_B}$$

applied to the ionization rates given by the SFA model in the velocity gauge [(V) form, see Eq. (5.16)]. The parameters are $I_p = k_B^2/2$, Z is the core

charge and E_0 is the peak field strength. We note that for all the short-ranged potentials ($Z = 0$) the correction factor reduces to unity and it is independent on the polarization state of the laser. In particular, the correction factor has an inverse dependence on the electric field, so it amplifies the low intensity part of the SFA and lowers the high intensity one.

Comparisons are made in [87] with the predictions of the *ab initio* Floquet calculation and SFA model for a H atom in a linearly polarized laser field. We have repeated the calculation, adding the results predicted by the SFA in the length gauge [(L) form, see Eq. (5.15)] and extending the intensity range. Fig. 5.2 shows the comparison¹.

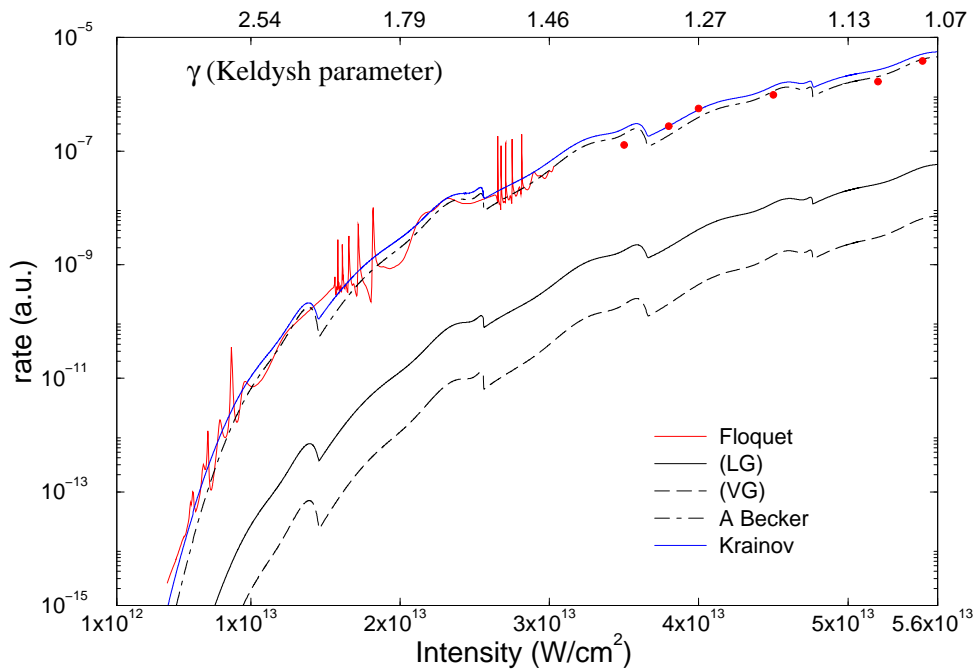


Figure 5.2: Rates of ionization of a hydrogen atom by a linearly polarized field at $\lambda=1064$ nm vs laser intensity. The (LG) and (VG) curves show the results predicted by the SFA model in the length gauge and velocity gauge. The other curves show the Floquet results (the red curve and filled circles), the A Becker *et al.* corrected version and the predictions of the Krainov Coulomb-corrected rate. The upper scale gives the Keldysh adiabaticity parameter.

¹The dot-dashed curve in Fig. 5.2 makes use of Eq. (2) from Ref. [87]. Nonetheless, the curve in Fig. 1 of [87], which would correspond to our dot-dashed curve, agrees very well with the calculation based on the Krainov correction (the blue line in Fig. 5.2).

We note that the biggest difference of about 3 orders of magnitude comes with the results in the SFA velocity gauge. The length gauge is roughly two orders of magnitude smaller than the Floquet results and the Krainov and the A Becker *et al.* corrections are in excellent agreement with the exact results. The A Becker *et al.* predictions are slightly smaller than those given by the Krainov formula.

In Ref. [87], another comparison is made with results from the direct integration of the Schrödinger equation and very good quantitative agreement is found (see Fig. 4 of [87]). Also, an extensive comparison for a number of laser wavelengths and atomic species is done with experimental results, and all show the same remarkable overall agreement (Fig. 6 in [87]).

The domain of validity for the WKB correction proposed by A Becker *et al.* is examined in the article of Reiss [92]. The author establishes lower and upper bounds on the intensity and shows that the correction is essentially a low-frequency one. Also, the author compares an energy resolved single ionization spectrum for helium, obtained experimentally, with the prediction of the SFA model in the velocity gauge and the A Becker *et al.* corrected SFA; it is shown that because the correction lowers the transition rate with increasing intensity, the agreement with the experiment (which is qualitatively well reproduced by SFA expression) is poor for the high energy tail of the spectrum. Therefore, the correction is useful only to calculate the total ionization rates.

We propose another way to analyze the applicability domain of the correction, by using the asymptotic expressions presented in Appendix (D) (thus implicitly assuming a low frequency of the laser field).

To calculate the ratio between the rates of ionization in the Krainov Coulomb corrected version (5.22) and in the velocity gauge (5.16) for a linearly polarized field, we follow the steps described in Subsection 5.4.1 and in the low-frequency limit, by summing over all multiphoton orders as done in Appendix (D), we

obtain:

$$\left(\frac{w_K}{w_V}\right)^2 = \left(\frac{Z^3}{E_0}\right)^2 \frac{\int_0^\infty \exp[-(\gamma^3/3\omega)p^2] dp}{\int_0^\infty \exp[-(\gamma^3/3\omega)p^2]/[(p/Z)^2 + 1]^2 dp}. \quad (5.43)$$

Apart from the ratio of the two integrals, the rates are identical up to a factor which is the same as the one used by A Becker *et al.*. The validity of the approximation requires then that the two integrals should have similar values. One of the integrals is a decaying exponential and the other has the same exponential and an extra factor in the denominator. For the two to have close values, the extra factor should be of order of unity, in the range of the integration variable where the exponential is still contributing to the value of the integral. So, we ask that $p/Z \ll 1$ within the decaying range for the exponential, $p < \sqrt{3\omega/\gamma^3}$. Combining the two conditions, we arrive at

$$Z\sqrt{\gamma^3/3\omega} \gg 1.$$

Typically, values of $Z\sqrt{\gamma^3/3\omega}$ bigger than 3 assure that the relative difference between the Krainov rate w_K and the corrected velocity gauge rate, as given by Eq. (5.43), is smaller than 10%. For the Fig. 5.2, the value is between 19 at low intensity and 3 at upper range of intensity, but the field frequency should be lower for our estimates to become more accurate. The conditions given in [92] are:

$$\omega Z\sqrt{2} \ll E_0 \ll Z^3,$$

and they refer to general conditions (specifically, the left inequality) under which SFA can be applied; thus, they do not state when the Krainov correction agrees with the A Becker *et al.* correction. The Reiss conditions are not satisfied in Fig. 5.2, with E_0 being up to 6 times *smaller* than the lower limit $\omega Z\sqrt{2}$. Thus, a qualitative and quantitative agreement should not to be expected at the intensities and field frequency employed here; despite the conditions not being satisfied, there is good general agreement with the Floquet results, as can be seen from Figure 5.2.

5.8 Study case: ionization of He^+ in a stationary field

We apply the Coulomb corrected rates in the case of He^+ for linearly polarized stationary field, with wavelength of 800 nm. For comparison, we use the exact DC rates [93], cycle averaged:

$$w(E_0) = \frac{2}{\pi} \int_0^{\pi/2} dt \Gamma(|E_0 \cos t|)$$

with $\Gamma(E_0)$ the DC rate at electric field amplitude E_0 .

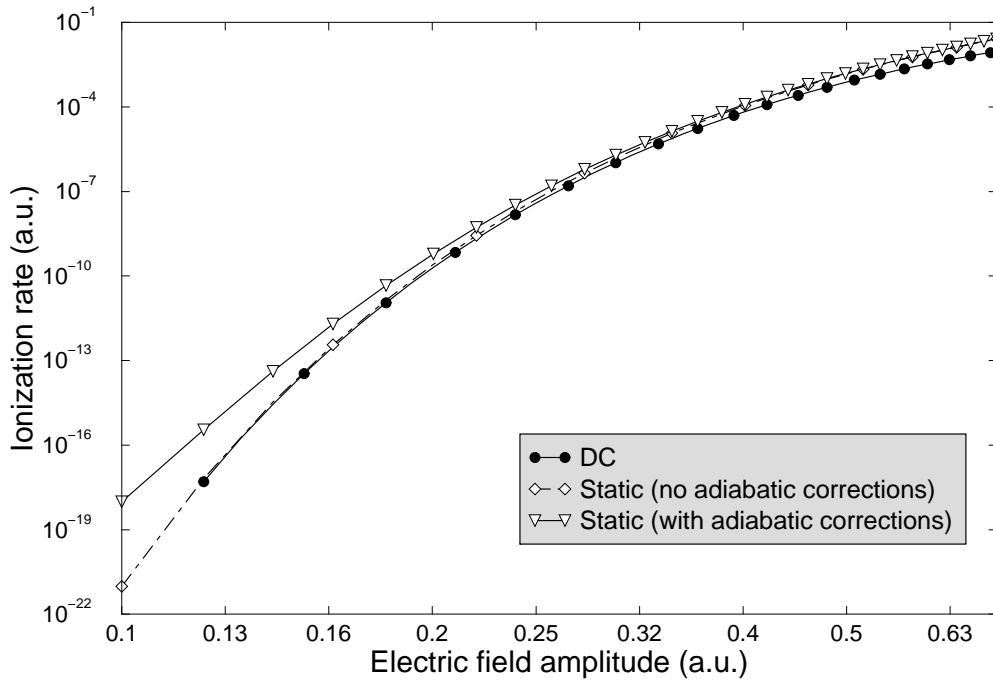


Figure 5.3: Log-Log plot of the ionization rates for He^+ in a linearly polarized stationary field. The wavelength is 800 nm.

Fig. 5.3 shows the averaged DC rates together with the adiabatically corrected static rates (D.12) [this is an approximation to the Krainov Coulomb corrected rate (5.22) in the tunneling limit] and the usual static rates (no adiabatic correction, namely $\gamma = 0$ in D.12). First thing to note is that the DC rate overlaps with the static rate at low field amplitudes. For high intensity, the adiabatically corrected static rate overlaps with the static rate; this is expected,

since the Keldysh adiabatic parameter decreases with increasing intensity, so the two rates become identical.

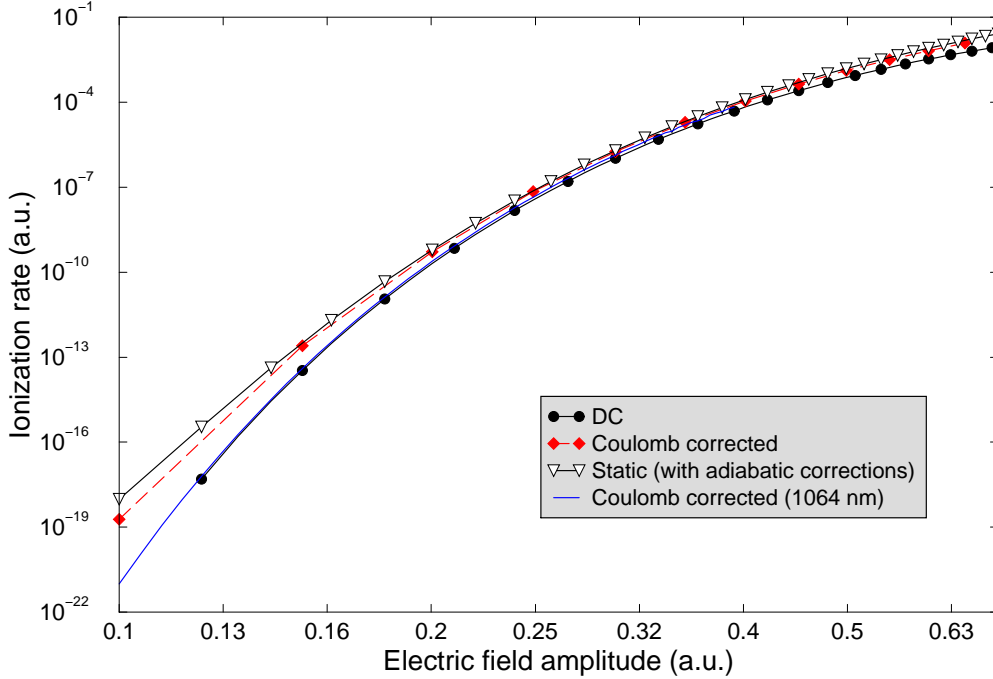


Figure 5.4: Same parameters as in Fig 5.3. The Krainov Coulomb corrected rates are shown for 800 nm and for 1064 nm.

Fig. 5.4 shows results from the Krainov Coulomb corrected rate both for 800 nm and for 1064 nm. The adiabatic corrected rate is closer to the Krainov result than the static rate, and all three approach each other at high intensity (where the Keldysh parameter γ is small). The case of a Nd:YAG laser (1064 nm) is presented because γ is lower than for 800 nm radiation; therefore, it almost overlaps with the results for the static rate even at small intensities, and at the upper intensity range, it approaches the results for the 800 nm.

After getting closer to the static rate at an intensity of approximately 2.2×10^{15} W/cm², the DC rate starts departing slowly from it with increasing intensity, showing that the exact static ionization rate cannot be approximated well by the usual static rate formula in this region.

The results presented confirm the validity of the asymptotic expressions deduced in Appendix D in the limit of low γ . It also shows the role of the

adiabatic correction to the static ionization rate, by analyzing its effects in different regimes of intensity and frequency of the laser field.

5.9 Conclusions

We have presented the main results from the literature concerning the Keldysh transition amplitude for the direct ionization along with the next order correction term, the latter being able to predict the rescattering plateau in the energy spectra of the ejected electrons.

Starting from the general formalism, we then discuss the direct ionization amplitude in the context of short laser pulses, with special attention devoted to the boundary terms and their correct treatment in numerical calculations. The boundary terms are calculated in both the length gauge and the velocity gauge and then related to the proper choice for the vector potential $A(t)$, which can simplify the final results is suitably chosen.

The Coulomb correction is introduced as given by Krainov and it is proven that the amplitude is the same in both velocity and length gauge. A simplified version of this correction [87] is examined and conditions for its applicability are proposed.

For the stationary field, general features, such as conservation of energy condition for the ejected electrons, are presented in detail. Calculation of the ionization rates are included for both circular and linear polarization; in each case, analytical formulae are given for these rates. The expression for the velocity gauge amplitude is applicable for the elliptical polarization and some of the analytical techniques can be extended to more general laser fields.

The last part compares results for the ionization rate in the case of a stationary field in the context of the Krainov rate, tunneling rate and the cycle-averaged rate based on the exact static rates. The role of the Keldysh adiabaticity parameter is pointed out in relating these results and establishing their domain

of applicability.

Chapter 6

Direct ionization in short pulses

6.1 Outline

In this chapter, we present the predictions of the Coulomb-corrected SFA model (KSFA) for direct ionization in short laser pulses. We show that the model confirms the well-known sensitivity of the angle-resolved ATI energy spectra to the absolute phase. This is also the case in the context of harmonic generation [94, 95]. The origin of this can be traced to the interplay between electron trajectories corresponding to direct ionization in the Simpleman's model. Finally, total probabilities are calculated and compared to those obtained using the exact static rates or the tunneling rate. The relevance of the Keldysh adiabaticity parameter γ is discussed. For all the cases studied here, we are in the tunneling regime, i.e., $\gamma < 1$, unless otherwise stated, and the laser intensity is such that the ionization is not in the over-the-barrier regime for the atomic systems considered.

In the last part of the chapter, we compare the predictions of the Coulomb-corrected SFA model to the fully numerical results from the Schrödinger equation; the major differences and their possible explanations are emphasized.

6.2 Pulse form and classical energy cutoffs

At relatively small intensities, the dipole approximation can be invoked. The magnetic field component of the pulse accelerates the electrons in the direction of field propagation for a linearly polarized laser, which tends to suppress re-collision processes. At 800 nm, the wavelength of a Ti:Sapphire laser, this effect becomes non-negligible for intensities above 10^{17} W/cm², in which case a non-dipole description is necessary.

Using the dipole approximation, the response of the atom to a linearly polarized laser pulse can be calculated by taking an electric field $\mathbf{E}(t) = E(t)\hat{\mathbf{e}}$ and a vector potential $\mathbf{A}(t) = A(t)\hat{\mathbf{e}}$. Although in some cases accurate numerical representations of the pulse are necessary, a simple analytical model is adequate in many applications. Assuming no chirp (the frequency is constant for the pulse), one can adopt the simple expression

$$E(t) = E_0 \chi(t) \sin(\omega t + \phi),$$

for the electric field of the pulse, or, alternatively,

$$A(t) = E_0/\omega \chi(t) \cos(\omega t + \phi)$$

for the pulse's vector potential. The two approximations are equivalent provided that the pulse is sufficiently long for $d\chi/dt$ to be negligible compared to $\omega\chi(t)$. It is convenient to characterize the pulse intensity by the peak intensity, I_0 , defined as for the stationary field, $I_0 = E_0^2/2$, assuming that $0 \leq \chi(t) \leq 1$.

The envelope function, $\chi(t)$, is usually taken a half-period \sin^2 function, encompassing a certain number of cycles n , such that

$$A(t) = A_0 \sin(\omega t + \phi) \sin^2(\omega t/2n). \quad (6.1)$$

In this case, the pulse has a strictly finite duration. If we define the full width at half maximum (*FWHM*) as the time interval during which the intensity envelope is bigger than half the peak intensity I_0 , we obtain for the \sin^2 pulse

$FWHM = 4n \arccos(2^{-1/4})/\omega$, or, in terms of one optical period $T = 2\pi/\omega$, $FWHM/T = 2n \arccos(2^{-1/4})/\pi \approx 0.364n$. If instead of intensity, we choose the field amplitude, then $FWHM = n\pi/\omega$, or $FWHM/T = n/2$ field periods.

Other popular choices are a Gaussian function (which is convenient as the intensity drops fast in the wings, but perhaps not as good a representation of the actual pulse) and a sech function. The later has for the vector potential

$$A(t) = A_0 \sin(\omega t + \phi) \operatorname{sech}(\omega t/\tau), \quad (6.2)$$

and the full width at half maximum in intensity is $FWHM = 2\tau \operatorname{arccosh}\sqrt{2}/\omega$ or, in units of one optical cycle, $FWHM/T = \tau \operatorname{arccosh}\sqrt{2}/\pi \approx 0.281\tau$. In amplitude, $FWHM = 2\tau \operatorname{arccosh}2/\omega$, or $FWHM/T = \tau \operatorname{arccosh}2/\pi \approx 0.419\tau$ optical cycles. Figure 6.1 shows a \sin^2 and a sech pulse with identical FWHM.

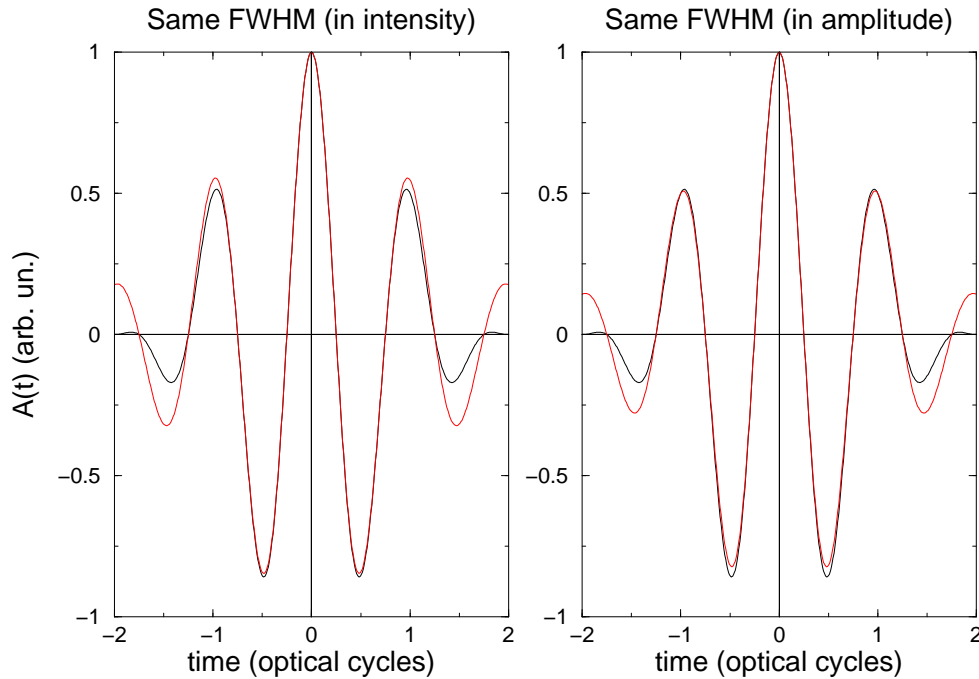


Figure 6.1: Left panel: a 4-cycle \sin^2 pulse (black curve) and a sech pulse (red curve) with the same FWHM (in intensity). The phase is $\phi = \pi/2$. The right panel shows the same, only for identical FWHM in amplitude.

To give an idea about the changes one might expect in the case of short pulses

when compared to a stationary field, we calculate the maximal kinetic energy at the time of return t of an electron starting in the origin at a time t' during the pulse, as well as the maximum kinetic energy after rescattering. If we define the quantity $k_s(t, t') = -\int_{t'}^t A(\tau) d\tau / (t - t')$, we look for the pair of ‘birth’ time t' and return time t (as in the Simpleman’s model) for which the return kinetic energy $E_{ret} = [A(t) - A(t')]^2/2$ is maximal, or the rescattering kinetic energy $E_{res} = [2A(t) - A(t')]^2/2$ is maximal. The solution must satisfy the condition $k_s(t, t') + A(t') = 0$, which means that the electron is back at the origin at time t . For the stationary field we have the well known values of $E_{ret} = 3.1731 U_p$ and $E_{res} = 10.0076 U_p$, with U_p the ponderomotive energy $U_p = A_0^2/4$.

Figure 6.2 shows the maximal return and rescattering energies in units of the ponderomotive potential U_p for a \sin^2 pulse with $A(t) \propto \sin(\omega t) \sin^2(\omega t/2n)$, as a function of the number of optical cycles n . The convergence to the values

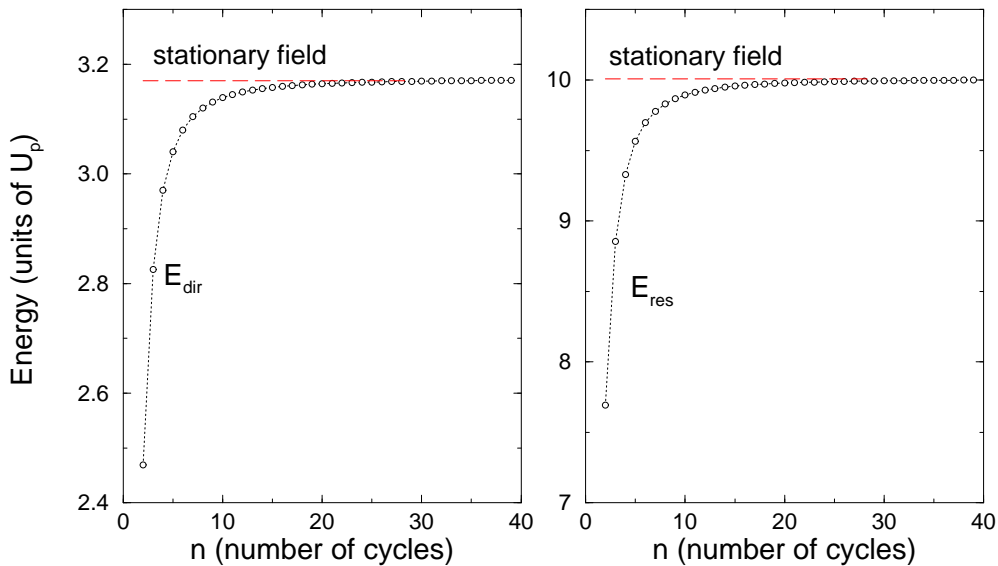


Figure 6.2: The cutoffs for the return (left panel) and rescattering (right panel) kinetic energy for a n -cycle \sin^2 pulse, with $A(t) \propto \sin(\omega t) \sin^2(\omega t/2n)$.

for the stationary field is readily achieved for both the direct and rescattering maximal energies. This shows that the envelope of the field can affect to a certain extent the physical processes. Some particular values are given in

Table 6.1; it is easy to see that already for a pulse with 38 optical cycles, the direct cutoff agrees to the stationary field's value with 0.07% relative accuracy.

n	2	4	5	10	14	19	28	38
E_{dir}/U_p	2.469	2.970	3.040	3.139	3.156	3.164	3.169	3.171
E_{res}/U_p	7.693	9.330	9.565	9.893	9.949	9.976	9.992	9.999

Table 6.1: Cutoffs for return and rescattering energy for \sin^2 pulses with different number of cycles (see Fig. 6.2).

Figure 6.3 shows the dependence with the phase ϕ of both energy cutoffs, for a 4-cycle pulse. The variation in the cutoff energies can be steep for certain values of ϕ . On the basis of the Simpleman's model, this indicates that the ionization process is highly sensitive to the phase of the field. Also, it points out that the relative phase ϕ can influence the process to a great extent, and it is important in applications to be able to produce laser pulses with controllable absolute phase and to find ways to accurately measure it.

6.3 Definitions of SFA angular and energy distributions

We use the Krainov Coulomb-corrected ionization amplitude [Eq. (5.22)], while for the vector potential we choose a linearly polarized field along the axis ϵ , with $\mathbf{A}(t) = A_0 \sin(\omega t + \phi) \sin^2(\omega t/2n) \hat{\epsilon}$. Choosing the vector potential zero at the beginning and the end of the pulse gives numerical advantages when calculating the transition amplitudes, by avoiding the boundary terms affecting the physical result. The quantities of interest are:

- the differential ionization probability for the emission of an electron with energy $E_p \equiv \mathbf{p}^2/2 = kU_p$ in the direction θ with respect to the polarization axis:

$$w(\theta, \phi) = \frac{|M_{\mathbf{p}}^{(0)}|^2 d^3\mathbf{p}}{d\Omega_{\mathbf{p}} dk} = U_p \sqrt{2kU_p} |M_{\mathbf{p}}^{(0)}|^2, \quad (6.3)$$

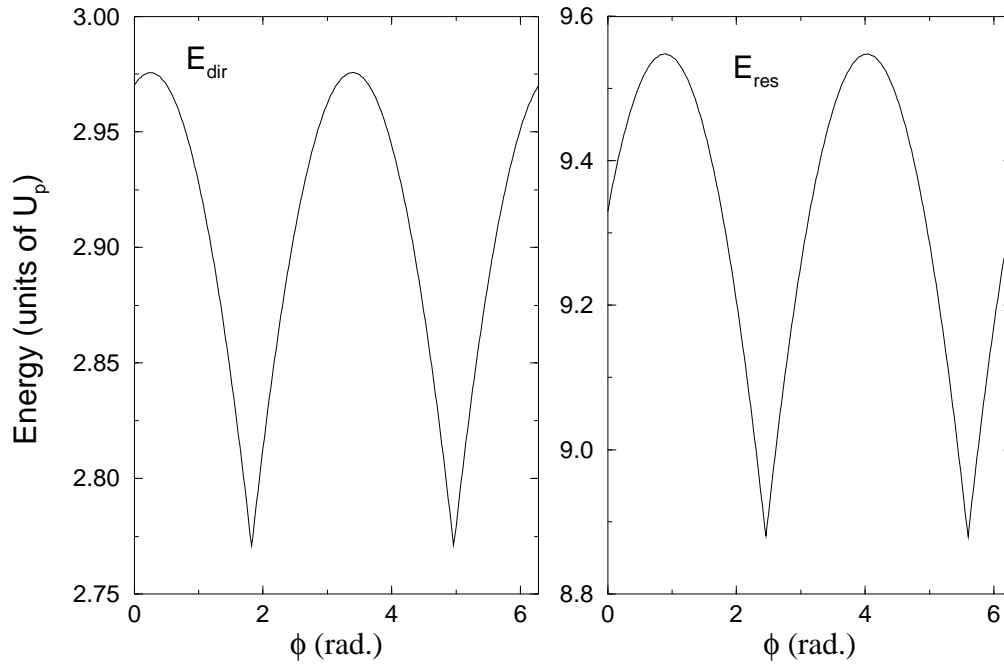


Figure 6.3: The phase dependence of the maximal return (left panel) and rescattering (right panel) kinetic energy for a 4-cycle \sin^2 pulse, with $A(t) \propto \sin(\omega t + \phi) \sin^2(\omega t/8)$.

where ϕ is the polar angle of the electron's asymptotic momentum in a plane perpendicular to the polarization direction and θ is the angle of ejection with respect to the polarization direction; $M_{\mathbf{p}}^{(0)}$ is the Krainov's transition amplitude for direct ionization. The electron emission is symmetrical around the polarization direction of the field (namely, the same for any value of ϕ);

- the differential probability per unit energy (in units of U_p) and per unit azimuthal angle θ , integrated over the polar angle ϕ :

$$w(k, \theta) \equiv \frac{d^2 \mathcal{P}}{dk d\theta} = 2\pi \sin \theta U_p \sqrt{2kU_p} |M_{\mathbf{p}}^{(0)}|^2, \quad (6.4)$$

with $E_p \equiv \mathbf{p}^2/2 = kU_p$.

Both distributions, integrated over the emission angles and energies, give the total emission probability. The angle/energy integrated probability is given by

the integration of Eq. (6.4) over θ and k , respectively:

$$\frac{d\mathcal{P}}{dk} = \int_0^\pi w(k, \theta) d\theta$$

and

$$\frac{d\mathcal{P}}{d\theta} = \int_0^\infty w(k, \theta) dk.$$

6.4 The accuracy of the saddle point method

Before presenting numerical results obtained for energy distributions of the ejected electrons in the case of finite laser pulses, we discuss first the accuracy of the saddle point method.

As discussed in detail in Appendix E.2.2, the exact integration can be performed in two ways: (i) Along the real axis, by using a special method to deal with the strongly oscillatory behavior of the integrand or (ii) Along a path in the complex plane, passing through the saddle point closest to the real axis, and connected to the end points of the integration interval by vertical lines. Of course, the results obtained by using either of the methods are identical in view of the Cauchy theorem.

Nonetheless, the complex plane integration method intuitively reveals a result from the asymptotic theory: the main contributions to an integral come from its saddle points (the integrand decreases exponentially in their vicinity) and from the end points of the integration interval. The latter part is known as the ‘boundary contribution’ and can be calculated analytically as an infinite series involving derivatives of the integrand, calculated at the end points (for more details, see Subsection E.2.2). In practice, we use only the first order boundary term (BT) contribution as the expressions for higher orders become increasingly cumbersome.

The BT terms can be shown to depend on the derivatives of the electric field at the beginning and the end of the laser pulse, i.e., on the way the laser

pulse is switched on and off. If the electric field derivatives at the temporal boundaries of the pulse are not negligible, then their inclusion in the result will distort the ionization spectrum. Therefore, according to one's intuition, the BT contribution should be extracted from the integral giving the ionization amplitude.

A way to eliminate the BT is to perform the calculation in the complex plane, and taking as a final result only the contribution coming from the path that goes through the saddle point, parallel to the real axis. The contributions coming from the connection paths with the end points of the integration interval should be thus discarded, as they represent the BT contribution. The result of such a procedure should be approximated to a high accuracy by the contribution of the saddle points. We show that this is indeed the case for the laser parameters we use. This way, the saddle point calculation implicitly discards the BT contribution and gives correct physical results.

Another way is to perform the calculation along the real axis and subtract the first order BT contribution only. The results agrees to the saddle point contribution, provided the higher order BT are negligible, which happens if the electric field is a smooth function at the beginning and the end of the pulse, or if the pulse is long enough (see Appendix E.2.2 for more details).

To illustrate the above, we present two sets of results: one for angle-resolved ATI energy spectra and the other for angular distribution of the ejected electron.

Figure 6.4 shows in the left panel an angle-resolved ATI energy spectrum for low field intensity, where BT are expected to play a role. Calculating the ionization amplitude by integration along the real axis followed by subtraction of the first order BT (red curve) is compared to the result obtained by integrating along the path in the complex plane, parallel to the real axis and going through the saddle point (hence eliminating the BT contribution – black curve). (The complex path integration agrees well with the result of the saddle

point method, as expected; the two cannot be distinguished on the scale of the graph.) Although the first order BT is extracted, there is a clear difference, due to higher order BT. For higher intensity (right panel), the two calculations (the saddle point and the one from which the first order BT has been subtracted) yield results in excellent agreement, undistinguishable on the scale of the graph. Should the BT terms not have been extracted from the integration along the real axis, we would obtain a result of order 10^3 a.u. instead of 10^{-8} in the left panel of Figure 6.4.

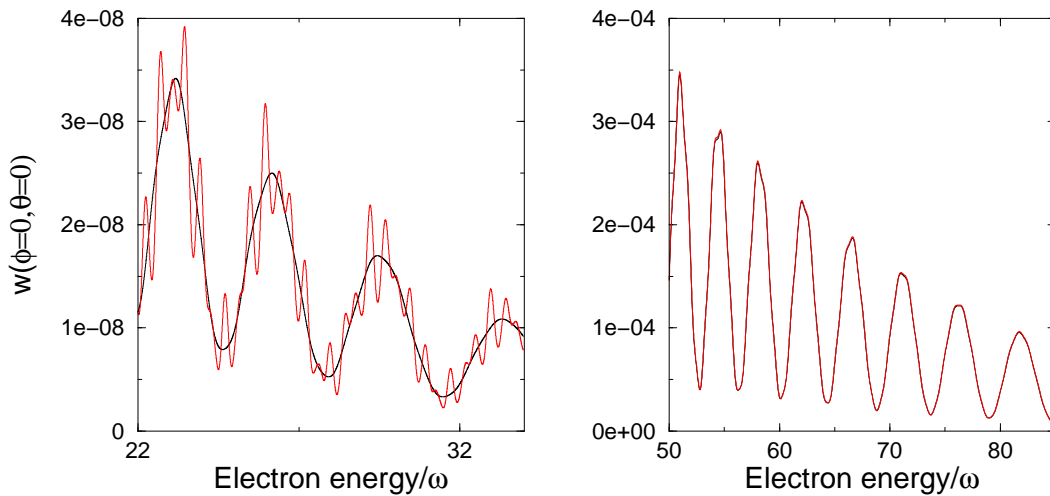


Figure 6.4: Angle-resolved [Eq. (6.3)] ATI energy spectra for electron emission from He^+ along the polarization axis for an electric field amplitude $E_0 = 0.2$ a.u. (left panel) and $E_0 = 0.3$ a.u. (right panel). The wavelength is 800 nm and the pulse duration is four optical cycles with $\phi = 0$. The red curves show the exact integration result from which the first order boundary term (BT) has been subtracted and the black curves show the saddle point result.

Similar comments can be made for the case of angular distribution spectra. The same values for intensities as in Fig. 6.4 are chosen in Fig. 6.5 for angular distribution spectra. The quantitative agreement with the saddle point results become better for higher intensity and/or for longer pulses.

In conclusion, for the range of intensities we are interested in, the saddle point method provides accurate numerical results for the ionization amplitudes. As the method is fast, it enables us to calculate, in a reasonable amount of com-

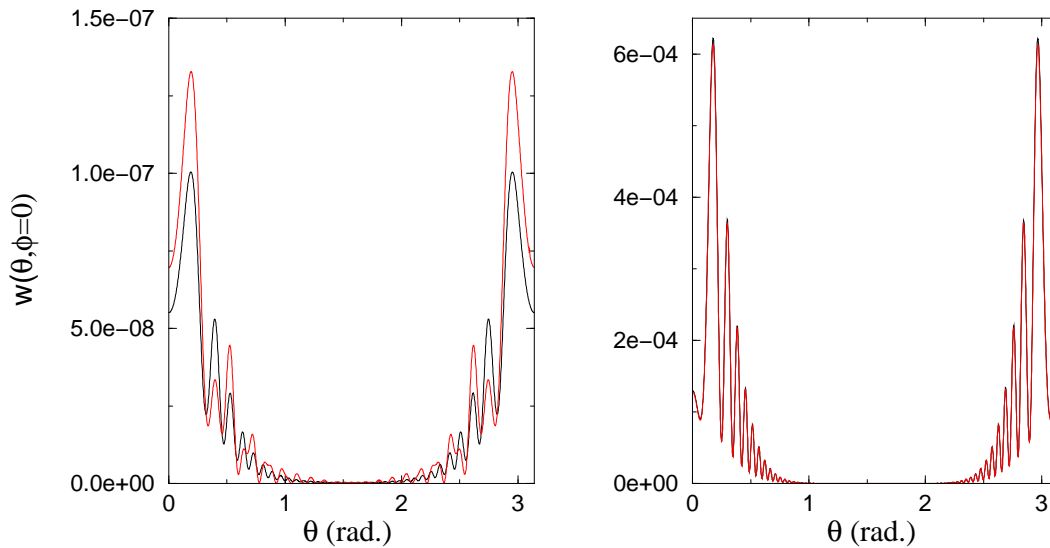


Figure 6.5: Angular distributions in He^+ for electron energy of $0.1U_p$. The pulse parameters are the same as in Fig. 6.4. The red curves show the exact integration result from which the first order boundary term (BT) has been subtracted and the black curves show the saddle point result.

putational time, angle/energy-integrated spectra or total probabilities.

6.5 Total ionization probabilities

The usual SFA model includes the Coulomb interaction in a first step, by using the exact wavefunction for the initial bound state of the ionizing electron. Further improvements include corrections due to tunneling through the potential barrier formed by the Coulomb potential and the external field: one way to do this is given by the KSFA version we use in our calculations. The accuracy for taking into account the Coulomb interaction within the SFA proved to be sufficient for obtaining correct total probabilities of ionization [37, 87, 89, 96].

In this section, we analyze the results for the ionization probabilities in a short laser pulse, given by the SFA model (with and without Coulomb correction). These are compared to the approximate results obtained by integrating along the pulse duration the exact ionization rate for a constant electric field; this

way, due to the low frequency of the carrier wave, we implicitly assume that the ionization process is of adiabatic nature. The ion studied is He^+ .

The total ionization probability is calculated by integrating Eq. (6.3) or (6.4) over the ejection angle and energy. For a 4-cycle, \sin^2 pulse with zero phase, the dependence with the laser peak intensity of the ionization probability calculated within the Coulomb-corrected SFA model is given by the blue curve in Fig. 6.6. In contrast to the results predicted by the usual SFA (for which the difference can be as much as two orders of magnitude), the Coulomb-corrected results are much closer to the estimated probabilities from the integration of the exact static rates (red curve). This justifies the use of the Coulomb-corrected SFA as a way to get more accurate quantitative results. As it will be shown in the next section, there are still significant qualitative differences between the Coulomb-corrected version and the exact results, but the order of magnitude is the same.

As seen in the similar comparison made for the stationary field, for higher intensities (thus lower Keldysh adiabaticity factor), the Coulomb-corrected SFA gives results closer to the ones obtained from integration of the static tunneling ionization rate of Landau and Lifshitz. Knowing the rate of ionization for a constant field $\Gamma(E)$, one can calculate the ionization probability as $\mathcal{P} = 1 - \int_0^{T_p} \Gamma[E(t)]dt$, where the integration is done over the entire laser pulse. The agreement at low Keldysh adiabaticity parameters comes from the proven fact that the rate of ionization obtained from the Coulomb-corrected SFA goes in the low frequency limit into exactly the static ionization rate (see Appendix D).

To conclude, the Coulomb-corrected SFA model gives results that are in better agreement with the adiabatic estimates of the ionization probabilities, than those of the usual SFA model. In the limit of low Keldysh adiabaticity parameter, the Coulomb-corrected SFA is close to the results coming from the integration of the static ionization rates. This proves that for the case examined here, in the tunneling limit, the ionization process is to a good approximation,

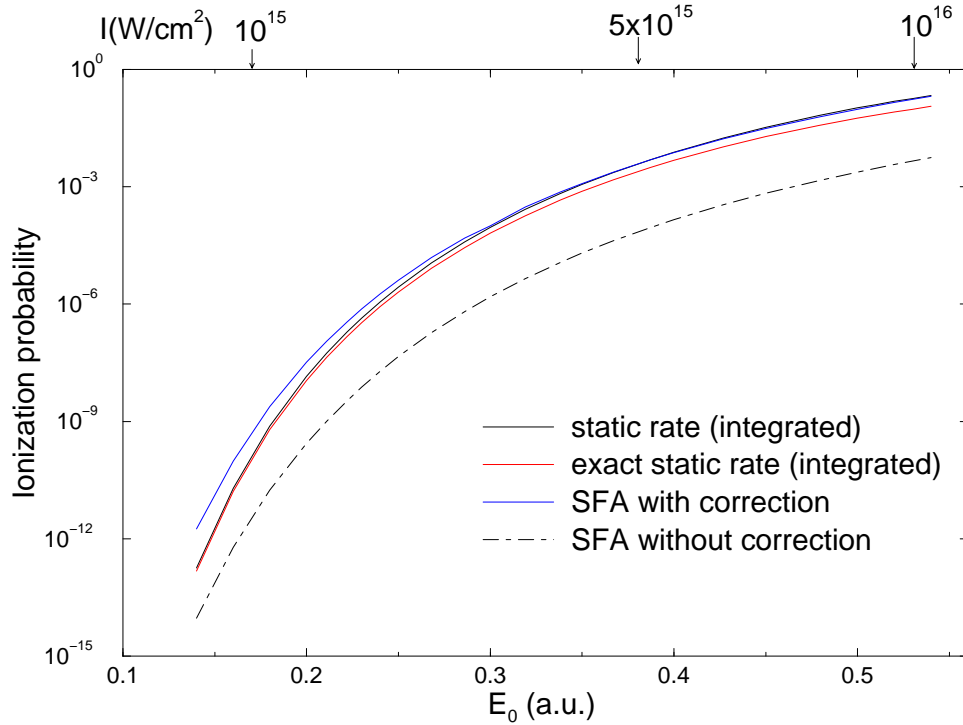


Figure 6.6: Total ionization probability for a He^+ ion irradiated by a four-cycle \sin^2 pulse, with $\phi = 0$. The results are given as a function of the peak intensity and originate for the usual and KSFA model. The other two estimates were calculated using the exact rate of ionization in a static electric field and the Landau and Lifshitz static tunneling rate, respectively.

adiabatic. As a final remark, the corrected SFA proves to be a useful tool to obtain estimates of the ionization probabilities in short laser pulses.

In the next section, we discuss the agreement of the Coulomb-corrected SFA with *ab initio* results, analyzing in detail some ATI angular distributions.

6.6 Differential ionization probabilities

We present some predictions of the Krainov Coulomb-corrected SFA model (KSFA) for direct ionization in short pulses, in the case of various ions. In Section 6.10 we show that for the field parameters and the atomic system studied there, the model is able to reproduce qualitatively the general charac-

teristics of the ATI spectra and predicts emission probability of the same order of magnitude as the results obtained from the Schrödinger equation (Section 6.10). The interference effects met in the case of the stationary field cannot build up unless the pulse is long enough. Without the Krainov correction, the SFA in the length gauge or velocity gauge predicts results that are a few orders of magnitude lower than the *ab initio* results.

Figure 6.7 shows the differential ionization probability [Eq. (6.4)] for two emission angles, close to the the axis of polarization. One remarkable feature is

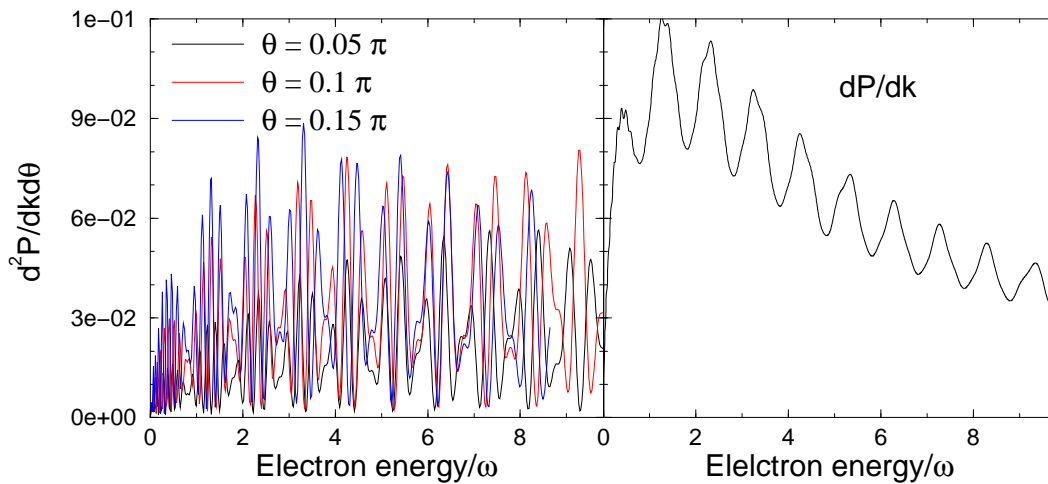


Figure 6.7: Left panel: angle-resolved ATI spectra for different emission angles θ with respect to the polarization direction. Right panel: angle-integrated ATI spectra. The pulse is with a \sin^2 envelope, encompassing four optical cycles, with 800 nm wavelength. The electric field amplitude is $E_0 = 0.4$ a.u. The ion is He^+ .

that for low ATI orders (LATI), the peaks occur at approximately the same energies, irrespective of the angle of emission. As a result, when integrating the probability over the emission angle, the LATI are still present in the angle-integrated spectrum (see the right panel of Fig. 6.7). As explained below, the weak dependence of LATI on emission angle is linked to the fact that the field phase ϕ is zero in Eq. (6.1). (The electric field is symmetrical with respect to the middle of the pulse.)

For a field phase different from zero, LATI peaks become less and less resolved

in the angle-integrated spectrum, until they eventually disappear. Figure 6.8 shows the case when the electric field is anti-symmetrical with respect to the middle of the pulse [$\phi = \pi/2$ in Eq. (6.1)]. The energies of the LATI peaks

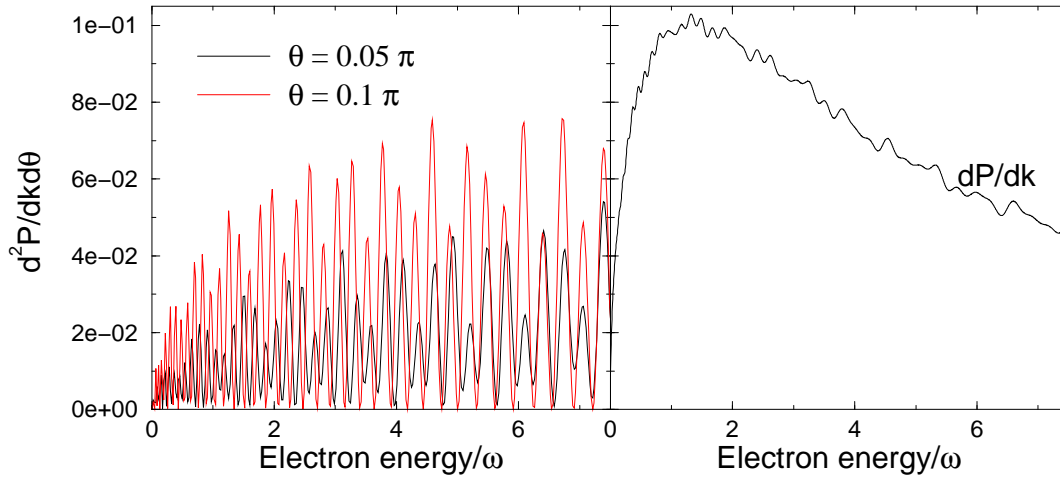


Figure 6.8: Left panel: angle-resolved ATI spectra for different emission angles θ with respect to the polarization direction. Right panel: angle-integrated ATI spectra. The parameters are the same as in Fig. 6.7, only the field phase is changed: $\phi = \pi/2$

depend now on the emission angle as it can be seen in the left panel. Hence, integrating over the angle of emission θ smoothes the spectrum, leading to less resolved LATI peaks. In particular, for the anti-symmetrical electric field, there are no peaks in the angle-integrated ATI spectrum, as the right panel of Fig. 6.8 shows. This dependence of LATI peaks on the field phase could help measuring the absolute phase of a short laser pulse.

Figure 6.9 shows the differential probability for two energies of the ejected electron, as a function of the emission angle θ . Note the decrease for higher energies although their values are far below the cutoff value. The probability of emission decreases faster for electrons not ejected along the polarization direction (which corresponds to $\theta = 0$ and $\theta = \pi$). For high ejection energies, the emission perpendicular to the polarization axis is practically negligible, this being characteristic for ionization in linearly polarized radiation. The dashed curves in Fig. 6.9 show the energy-integrated probability. Because

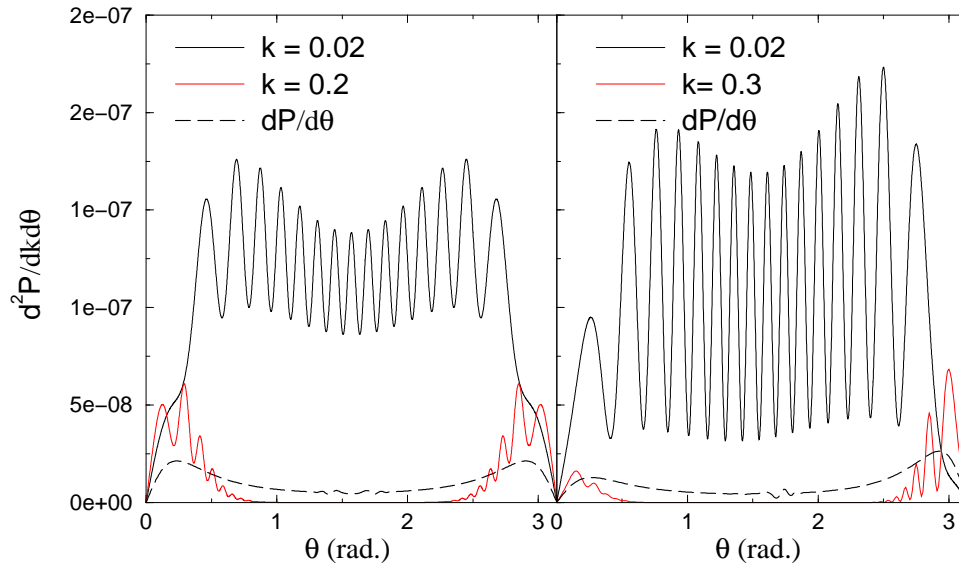


Figure 6.9: The differential ionization probability for constant electron energy as a function of the emission angle and the energy-integrated probability for He^+ irradiated by a four-cycle \sin^2 pulse with peak electric field $E_0 = 0.2$ a.u. Left panel: the field phase is $\phi = 0$, right panel: $\phi = \pi/4$. The wavelength is 800 nm. (The ponderomotive energy is $U_p = 0.77$ a.u.)

of the symmetrical electric field with respect to the middle of the pulse, the electron emission in the left panel has a backward-forward symmetry (i.e., emission at angle θ is the same as for the angle $\pi - \theta$). This is typical to Keldysh-like theories as the Coulomb interaction, responsible for breaking the symmetry, is not included. (For a more detailed discussion of Keldysh-like theories for ionization in elliptical polarization, see Ref. [97] or for asymmetries in short laser pulses see Ref. [98].) Another symmetry is for rotations around the polarization axis; together with the other symmetry, it gives the known fourfold symmetry of the angular distribution of the SFA model. The right panel of the same figure depicts the case of a nonzero value of the field phase. As the electric field is not symmetrical with respect to the middle of the pulse, the electron emission is bigger in that direction of the polarization axis in which the electric field points mostly during the pulse. This effect is discussed in Section 6.9.

6.7 Mathematical analysis

Based on the saddle point method, the interference effects due to different electron trajectories during the pulse duration can be analyzed and, for low energies, approximate analytical expressions describing this interference can be found.

The ionization amplitude is given by a sum over the contribution of all saddle points, of the form:

$$\mathcal{A} = \sum_{l=1}^{n_s} a_l \exp(iS_l), \quad (6.5)$$

where a_l and S_l are the amplitudes and the phase of the contribution of saddle time t_l . The modulus squared reads:

$$|\mathcal{A}|^2 = \sum_{l=1}^{n_s} a_l^2 + 2 \sum_{\substack{l, m=1 \\ m>l}}^{n_s} a_l a_m \cos(S_l - S_m), \quad (6.6)$$

In order to analyze the possible interference effects in Eq. (6.6), one needs to calculate the expression of the phase difference between any two saddles. The saddle points are solutions of the equation $[\mathbf{p} + \mathbf{A}(t)]^2/2 + I_p = 0$; the equation can be re-written as $A(t_s) = -p_{\parallel} \pm i\sqrt{2I_p + p_{\perp}^2}$, where the indices for the asymptotic momentum \mathbf{p} refer to the directions parallel and perpendicular to the polarization direction, respectively. For small energies $|\mathbf{p}^2/2| \ll U_p$, we have that t_s is close to t_0 , where t_0 is one of the zeros of the vector potential, $\mathbf{A}(t_0) = 0$; this can be seen from the equation for $A(t_s)$. The goal is to write an expansion of quantities of interest (such as the semiclassical action $S(0, t) = \int_0^t dt' [\mathbf{p} + \mathbf{A}(t')]^2/2 + I_p t$) for small electron energies. This can be accomplished by expanding the time derivative of the action around t_0 , up to a second-order term proportional to the small quantity $(t_s - t_0)^2$. By solving the approximate equation for the saddle time t_s and replacing it in the expression of the action, one obtains:

$$S(0, t_s) = S(0, t_0) + \frac{p_{\parallel}}{E(t_0)} \left(I_p + \frac{p^2 + 2p_{\perp}^2}{6} \right) + i \frac{(2I_p + p_{\perp}^2)^{3/2}}{3|E(t_0)|} + \dots \quad (6.7)$$

Consider now a pair of saddles: denoting the two saddle times in the pair by t_{s1} and t_{s2} , then, from Eq. (6.7) one obtains the following expression for $S_2 - S_1 \equiv S(0, t_{s2}) - S(0, t_{s1})$:

$$S_2 - S_1 = S(t_{01}, t_{02}) + p_{\parallel} \left(I_p + \frac{p^2 + 2p_{\perp}^2}{6} \right) \left[\frac{1}{E(t_{02})} - \frac{1}{E(t_{01})} \right], \quad (6.8)$$

where $S(t_{01}, t_{02}) \equiv \int_{t_{01}}^{t_{02}} \{[\mathbf{p} + \mathbf{A}(t')]^2/2 + I_p\} dt'$. The expression obtained for the phase difference of a pair of saddles applies only for low momenta of the ejected electron. The reason for using the times t_{01} and t_{02} is that they do not depend on \mathbf{p} , making the analysis possible. The phase difference is seen to depend on the angle of ejection, via the quantity p_{\parallel} , only through the term $\int_{t_{01}}^{t_{02}} A(t) dt$ and another one proportional to the difference $E(t_{02}) - E(t_{01})$. When doing the integration over the angles to obtain the angle-integrated ATI spectrum, the contribution of a certain saddle pair averages to zero if the corresponding phase difference of the pair depends on the angle. Hence, to avoid the cancellation of a certain pair, the necessary condition is to have $\int_{t_{01}}^{t_{02}} A(t) dt = 0$ together with $E(t_{02}) = E(t_{01})$. If there is not at least one such a pair whose amplitude $a_l a_m$ is not negligible, then one would expect a relatively flat angle-integrated ATI spectrum. Moreover, for a pair (lm) whose phase difference does not depend on the angle of emission, the LATI peaks coming from the pair's interference occur at energies given by the condition $S_l - S_m = 2N\pi$, when constructive interference takes place between the contributions of the two saddles. These peaks are not affected by the angle integration.

To exemplify, we study in the next Subsection the case of a four-cycle symmetrical electric field, for which the interference occurs typically between a pair of saddles and an isolated saddle. We prove that, when integrating over the emission angle, the modulus squared of the total contribution is equal approximately to the modulus squared of the contribution coming from the saddle pair and the modulus squared of the isolated saddle contribution. This is in agreement with the previous discussion. The case of an anti-symmetrical electric field is presented in Subsection 6.7.2.

6.7.1 The case of symmetrical electric field

Let us consider the case when the electric field has the same value for both saddles, $E(t_{01}) = E(t_{02})$. This happens for example if the electric field is symmetrical with respect to the middle of the pulse [$\phi = 0$ in Eq. (6.1)]. Fig. 6.10 shows such a possible configuration for a four-cycle \sin^2 pulse; one can see that in this case $t_{02} - t_{01} = 2\pi/\omega$. Because of the strong nonlinear dependence of the ionization amplitude on the electric field, we discuss only the saddle pair with the highest electric field value. Then, from Eq. (6.8), using that the

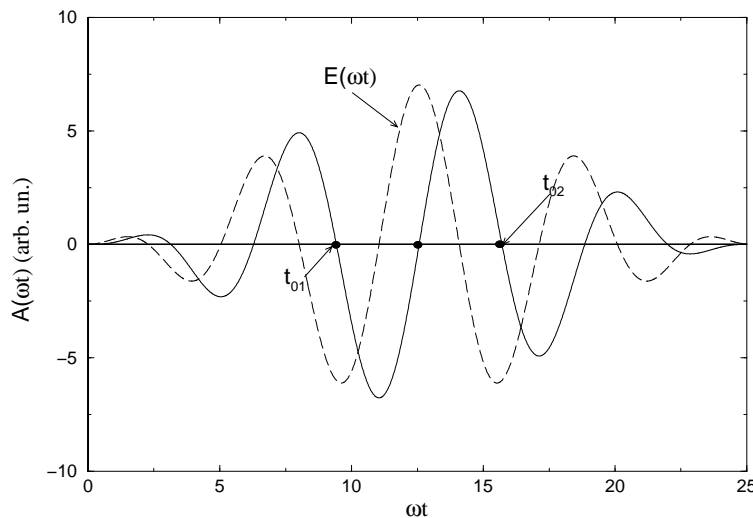


Figure 6.10: The case of a symmetrical electric field.

electric fields are equal at the two times t_{01} and t_{02} and that $\int_{t_{01}}^{t_{02}} A(t') dt' = 0$ due to the asymmetry of $A(t)$ with respect to the middle of the pulse, the condition for constructive interference for the saddle pair reads

$$\left(\frac{p_N^2}{2} + I_p\right) \frac{2\pi}{\omega} + \int_{t_{01}}^{t_{02}} A^2(t')/2 dt' = 2N\pi, \quad (6.9)$$

giving the energies of LATI peaks: $p_N^2/2 = N\omega - [(\int_{t_{01}}^{t_{02}} A^2(t')/2 dt')/(2\pi/\omega) + I_p]$. Thus, the pair has the property that its interference pattern does not depend on the angle of emission (see the previous general discussion at the beginning of this Section). The other possible pairs can be formed by the isolated saddle and t_{01} or t_{02} , respectively; these pairs are seen to depend on the

angle of emission, as the electric fields differ within each pair and also $\int A(t)dt$ is non-zero between the pair's saddles [see Eq. (6.8)]. As a consequence, their interference patterns does not contribute to the angle-integrated spectrum.

The symmetrical pair's interference peaks are separated by ω , the carrier wave frequency. Their energies are seen not to depend on the emission angle θ and this explains why the LATI peaks are still well resolved after integrating over θ . An illustration of this was presented in the left panel of Fig. 6.7, from Section 6.6. The expression for LATI energies is identical to the definition of the ATI peaks for a stationary field (the conservation of energy condition). With t_{01} and t_{02} taken as the beginning and the end of one optical cycle, the quantity $\left(\int_{t_{01}}^{t_{02}} dt' A^2(t')/2\right)/(2\pi/\omega)$ resembles the definition of the ponderomotive energy U_p , for a stationary field.

As an application of the LATI energies formula, Figure 6.11 shows angle-resolved ATI energy spectra for a four-cycle pulse; the contribution is only that of the symmetrical pair's. Three different emission angles with respect to the polarization axis are depicted. Note the decrease of the ionization amplitude with increasing emission angle. The filled circles represent the LATI energies calculated from Eq. (6.9). The agreement is very good and indicates also that our expansion holds for not so small kinetic energies (in this case, up to $0.15U_p$).

Furthermore, interesting effects could appear. This is due on one hand to the fact that LATI peaks do not depend on emission angle and on the other hand to the fact that the main contribution to the ionization amplitude comes from an isolated saddle point (corresponding to electron emission close to the middle of the pulse – see Fig. 6.10) and from one pair of saddles. The magnitude of the isolated contribution is the biggest, as the electron is emitted close to the peak of the electric field. If the pair's contribution is smaller, then, as a result, the angle-integrated spectrum will display a series of LATI peaks modulated by the saddle pair, superimposed over a background whose magnitude is given by the isolated saddle.

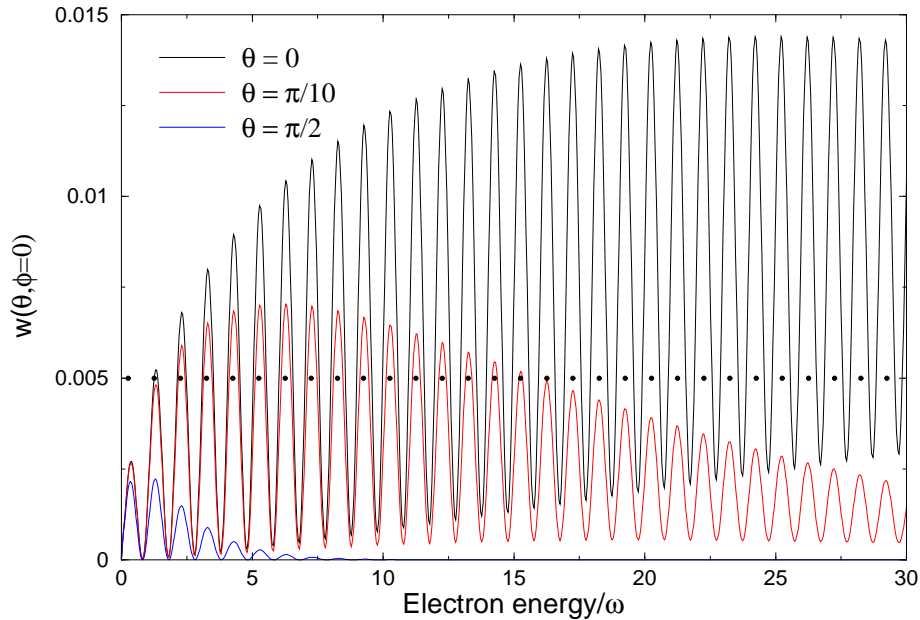


Figure 6.11: Angle-resolved ATI energy spectra at different emission angles for a He^+ irradiated by a \sin^2 pulse with $E_0 = 0.4$ a.u. and field phase $\phi = 0$. The wavelength is 800 nm. Only the contribution of the symmetrical pair of saddles is shown. The filled circles represent the predicted LATI peaks, from Eq. (6.9).

Figure 6.12 shows the angle-integrated ATI spectrum for the case of a four-cycle symmetrical electric field. In agreement with those discussed above, the main contribution to the ionization rate comes from an isolated saddle (with the biggest magnitude) and from a pair of saddle points (responsible for the interference pattern in the angle-integrated spectrum). The second pair's contribution is six orders of magnitude lower than the first pair's. One can see that the magnitude of the LATI peaks is set by the isolated contribution, while the modulation of the spectrum is due to the pair of saddles. The peak separation in energy is equal to approximately ω , the carrier wave frequency.

As discussed in Section 6.7, the ATI spectrum for each angle of emission consists of peaks at energies which do not depend on the angle (the LATI peaks are given by the interference of the saddles in the pair). The energy-resolved spectra for different emission angles are modulated by a factor depending on the angle, coming from the interference of each of the saddles in the pair with

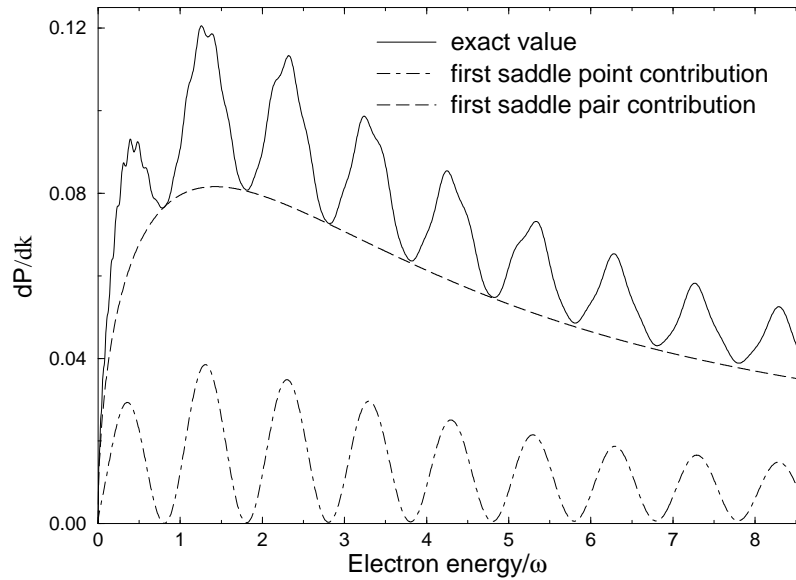


Figure 6.12: The saddle point contributions to the ionization probability of He^+ , for a 4-cycle \sin^2 pulse with symmetrical electric field. The pulse has 800 nm wavelength and the peak electric field is $E_0 = 0.4$ a.u.

the isolated saddle. In the final angle-integrated spectrum, these fast oscillations depending on the angle average out, and one sees only the peaks at the angle-independent energies.

Increasing the pulse duration and/or intensity will result in better resolution for LATI peaks in the angle-integrated spectrum. Of course, if the pulse duration is too long, the effects just discussed become less relevant, as the pulse resembles a stationary field, where the carrier phase is no longer important in the physical processes. These aspects are discussed in the Section 6.8.

6.7.2 The case of anti-symmetrical electric field

For an anti-symmetrical electric field we have $E(t_{01}) = -E(t_{02})$ and $t_{02} - t_{01} = \pi/\omega$. Figure 6.13 shows the first two saddle pairs. Due to the lower electric field magnitude, the second saddle pair (filled red circles) does not contribute

to the ionization amplitude. Equation (6.8) can be re-written as

$$\left(\frac{p^2}{2} + I_p\right) \frac{\pi}{\omega} + p_{\parallel} \left[\int_{t_{01}}^{t_{02}} A(t') dt' + \left(I_p + \frac{p^2 + 2p_{\perp}^2}{6}\right) \frac{2}{E(t_{01})} \right] + \int_{t_{01}}^{t_{02}} \frac{A^2(t)}{2} dt = 2N\pi. \quad (6.10)$$

The situation is different from the symmetrical case, as because of the ' p_{\parallel} ' term

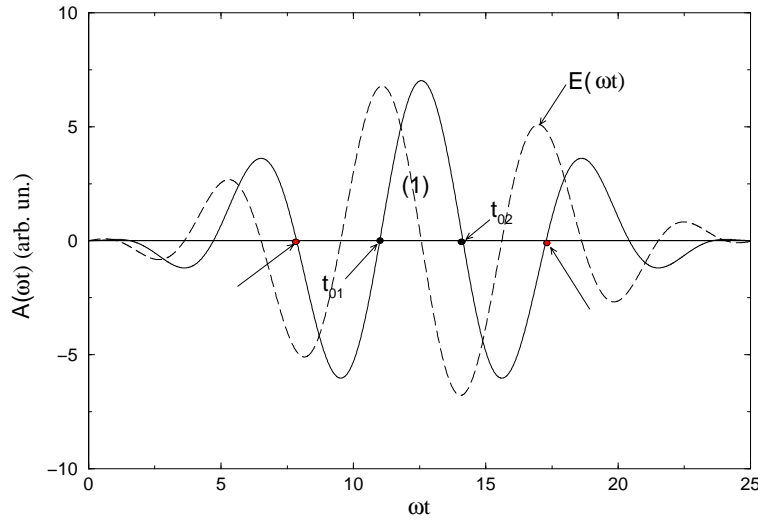


Figure 6.13: The case of an anti-symmetrical electric field.

in Eq. (6.10), the LATI peaks depend now on the emission angle. Their energies satisfy a cubic equation in p_N and the spacing between two consecutive peaks is no longer equal to the carrier frequency ω , as in the case of the symmetrical electric field. Figure 6.14 shows the accuracy of the LATI peaks prediction formula.

The particularity of the anti-symmetrical case is that the dependence of LATI peaks on the emission angle relates to the quantity $\int_{t_{01}}^{t_{02}} A(t') dt'$ (the region '(1)' in Fig. 6.13). The smaller its value is, the weaker the dependence on the emission angle. A typical example was given in left panel of Figure 6.8, Section 6.6. The angle-integrated spectrum in the right panel shows no peaks: as the position of the LATI peaks depends on angle, the integration results in a relatively smooth angle-integrated spectrum (right panel in the same figure).

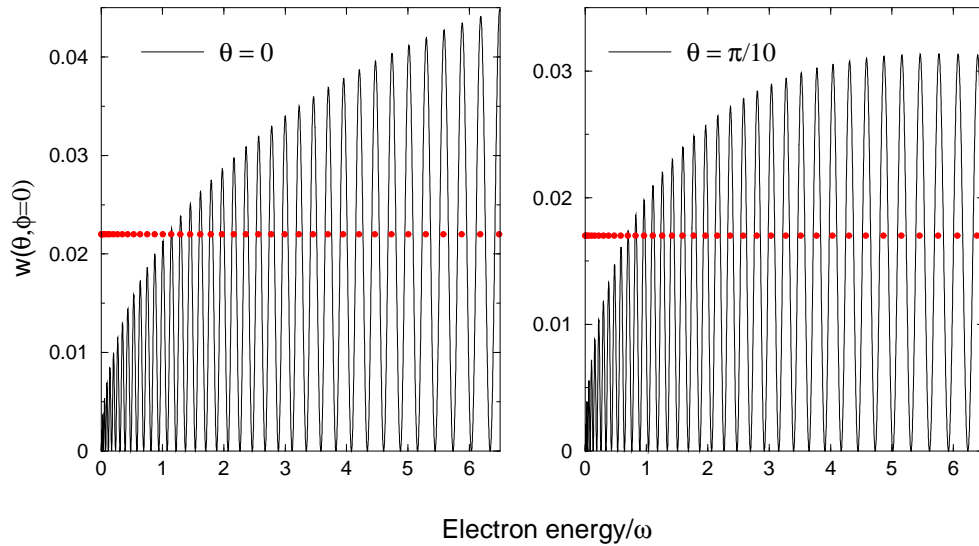


Figure 6.14: Angle-resolved LATI energy spectra. Only the contribution of the first pair is shown. The parameters are the same as in Fig. 6.11, only the electric field is anti-symmetrical: $\phi = \pi/2$. The filled circles are the predicted LATI peaks, from Eq. (6.10). The emission is along the polarization direction (left panel) and at an angle $\theta = \pi/10$ with respect to the polarization axis (right panel).

6.8 Influence of pulse parameters on direct ionization

For a given intensity, there is a maximal pulse duration for which phase effects still play a role, as the previous discussions suggest. Moreover, we show that the resolution of LATI peaks depend on the pulse intensity, duration and shape.

6.8.1 Influence of the field phase

From the previous sections, we have seen that LATI peaks depend on the field phase value. We choose here a four-cycle \sin^2 pulse and study the angle-integrated LATI spectrum while changing the field phase.

To see how sensitive the effect of LATI disappearance is with the phase variation from zero, Fig. 6.15 shows calculations done for increasing phases. The spectra for nonzero phase have no LATI peaks, and the effect is visible even

for phases as small as $\pi/10$ (the blue curve). For the anti-symmetrical electric

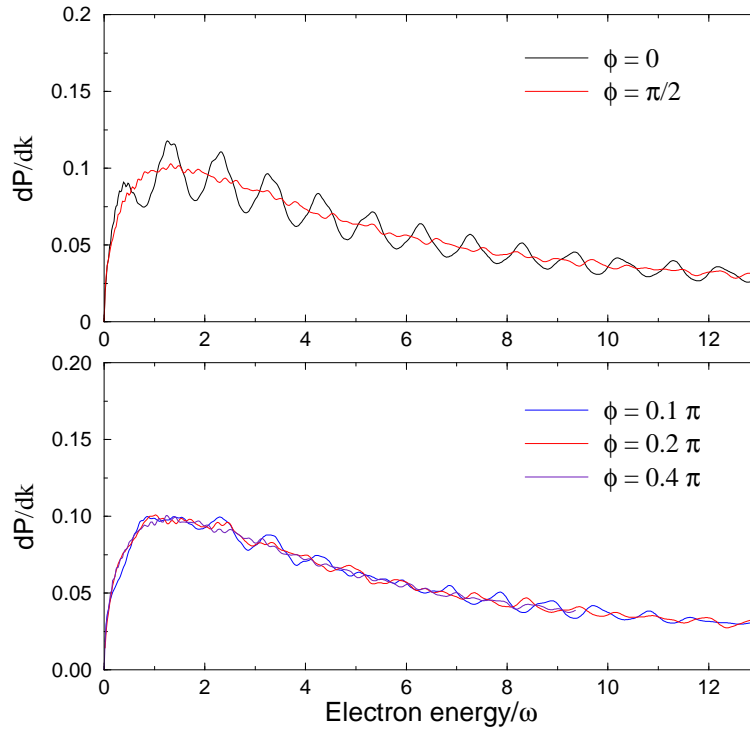


Figure 6.15: The angle-integrated ionization probability in He^+ for the same pulse as in Fig. 6.12, only for various field phases.

field ($\phi = \pi/2$), the spectrum is almost flat, with no structure.

6.8.2 Influence of the intensity

For short pulses and/or low intensities, the contribution to the ionization amplitude of the saddle pair is much less than the magnitude of the isolated saddle. Under such conditions, even for a symmetrical electric field, the LATI interference pattern has little contrast or is even absent in the angle-integrated spectrum. The left panel in Fig. 6.16 shows a case where despite the phase being zero, the LATI do not appear in the spectrum. The explanation is that the amplitude of the saddle pair's contribution is so low that does not influence the ATI spectrum. To improve the contrast, it suffices to increase the intensity (see the centre panel). This way, the contribution of the saddle pair

increases and LATI become better resolved. Further increase of the intensity allows higher energy peaks to gain resolution (right panel).

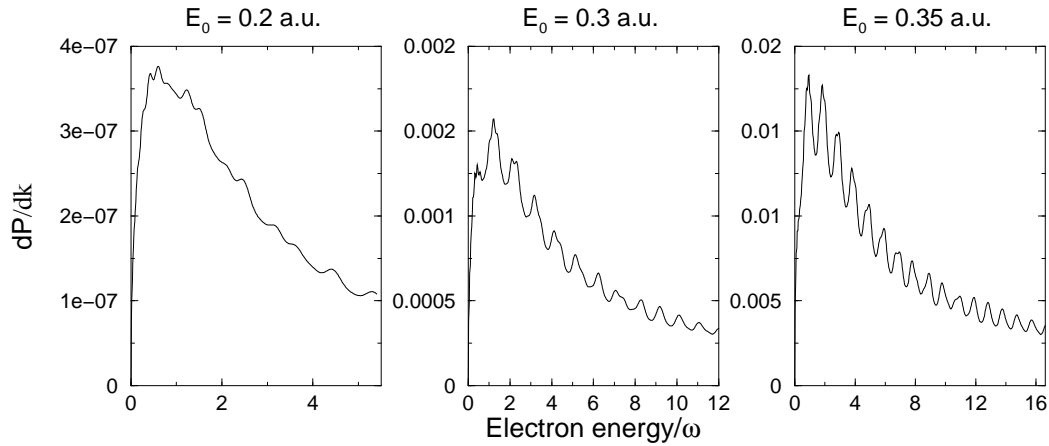


Figure 6.16: Angle-integrated ionization probability of He^+ for increasing intensity. The electric field is symmetrical with respect to the middle of the pulse. The rest of the pulse parameters are the same as in Fig. 6.18.

If we increase the intensity for a field with non-zero phase, the ATI spectrum changes as in Fig. 6.17. The spectrum remains relatively flat, with no well-resolved ATI peaks.

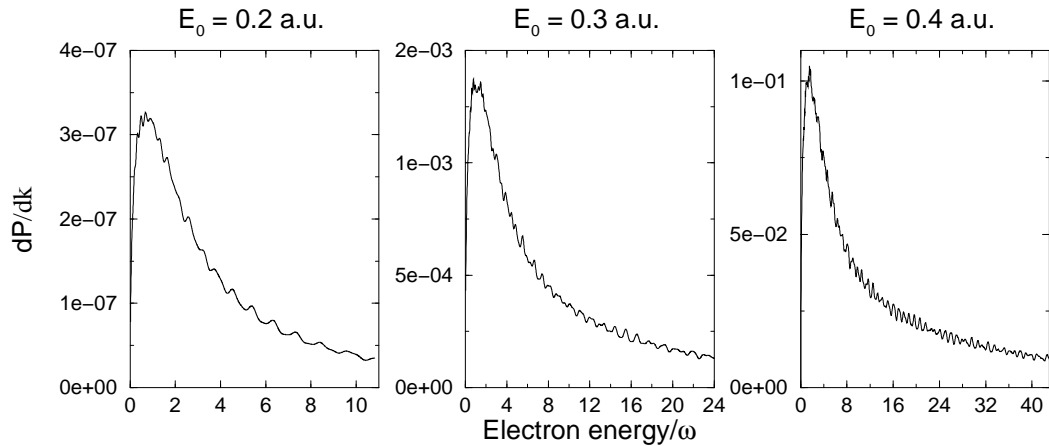


Figure 6.17: Angle-integrated ionization probability of He^+ for increasing intensity. The electric field has the phase $\phi = \pi/4$. The rest of the pulse parameters are the same as in Fig. 6.18.

6.8.3 Influence of pulse duration

For a short pulse, we have seen that the carrier phase can influence to a great extent the appearance of the LATI peaks in the angle-integrated ATI spectra. For phases different from zero, the LATI peaks are less and less resolved, until they eventually disappear. In addition, even for a symmetrical electric field, if the intensity is too low and/or the pulse is too short, the LATI peaks are not well resolved.

A possible way to have better contrast for the LATI peaks is to increase the pulse duration. Figure 6.18 shows a field with zero phase, which should have LATI peaks in the angle-integrated spectrum. For a pulse as short as two cycles and low intensity, the magnitude of the saddle pair contribution to the ionization spectrum is much lower than that of the isolated saddle. Hence, there is no modulation in the spectrum and the LATI peaks are absent. Because the relative magnitude of the isolated saddle contribution to that of the saddle pair is set by the ratio of the ionization rates at the corresponding birth times, its variation is more abrupt in the region of low electric fields. This is because the tunneling ionization rate varies strongly at low electric fields. By increasing the pulse duration, the contribution of the saddle pair increases relatively to the isolated saddle contribution, and the LATI peaks begin to appear, separated approximatively by ω , the carrier wave frequency.

If the pulse is long enough, the phase effects become less important (see also Ref. [32] for phase effects related to ionization in circularly polarized short pulses, where the authors reached similar conclusions). Figure 6.19 shows the angle-integrated spectra for a non-zero field phase. For a four-cycle pulse, the LATI are not well resolved, as expected (see the left panel). The centre panel displays the results for longer pulses (five and six optical cycles). Despite the non-zero phase value, LATI peaks are seen in the spectra and the lower their energy, the better the resolution. Increasing the pulse duration, the resolution improves even more, looking similarly to the ATI spectrum for a stationary

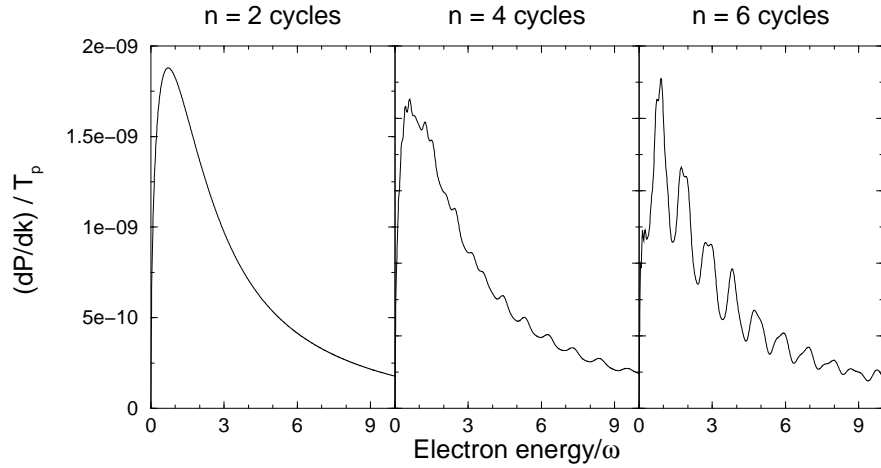


Figure 6.18: Angle-integrated ionization probability per pulse duration in He^+ irradiated by a 4-cycle \sin^2 pulse with $E_0 = 0.2$ a.u. and $\phi = 0$.

field. The spacing between the peaks is approximately ω , the carrier wave frequency. The explanation for this is that with increasing duration, the field

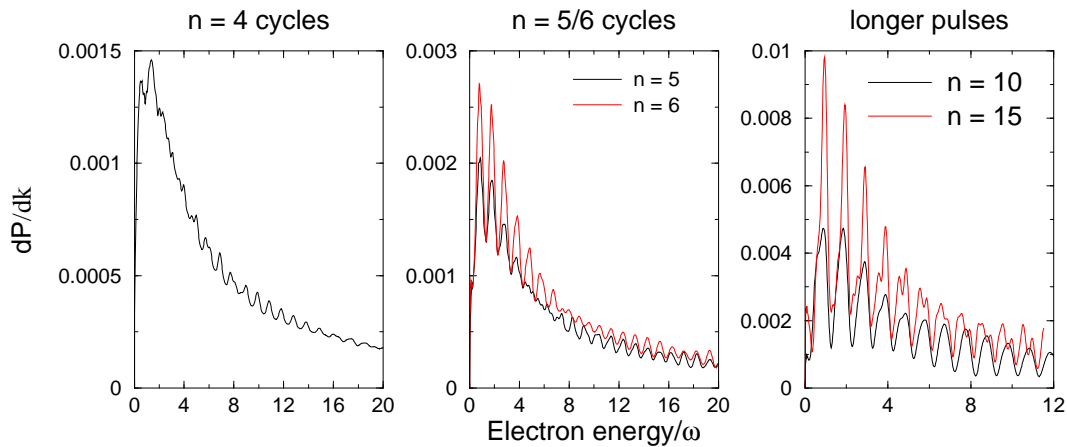


Figure 6.19: Angle-integrated ionization probability in He^+ for different duration \sin^2 pulses with $E_0 = 0.3$ a.u. and phase $\phi = 0.23$ rad. The rest of the parameters are the same as in Fig. 6.18.

near the peak of the envelope (where the main contribution to the ionization amplitude comes from) encompasses a large number of optical cycles. This in turn, resembles a stationary field. The larger the pulse duration is, the less relevant the phase effects become. For the intensity used in Fig. 6.19, already for nine cycles and longer, the phase effects diminish when compared to a

four-cycle pulse.

In conclusion, for a given intensity, one possible way to increase the resolution of LATI peaks is to increase the pulse duration. However, a pulse that is too long loses the sensitivity to the phase effects. For symmetrical electric field and same pulse duration, better resolution can be achieved by increasing the field intensity.

6.8.4 Influence of the binding energy and pulse shape

The pulse shape can affect the ATI spectrum due to effects induced by the shape of the envelope (more precisely, the envelope variation near its peak).

Figure 6.20 shows the angle-integrated ATI spectrum for a sech pulse [for definition, see Eq. (6.2)]. The spectrum for symmetrical electric field is compared to the one for the case of a \sin^2 pulse, with the same FWHM (in amplitude). In the left panel it can be seen that the general effect of interference described previously is still present, independent of the pulse shape. The right panel presents the situation for different field phases, where the LATI are less resolved.

Another case we choose to study is a Gaussian pulse, with the width such that its FWHM (in amplitude) is the same as for a four-cycle \sin^2 pulse. The same comparison as for the sech pulse is done. Figure 6.21 shows in the left panel that the general behavior of LATI peaks contrast with the field phase is the same. The right panel depicts the LATI losing resolution for phases different from zero.

Both the sech and Gaussian pulse calculations prove that the analysis done in Section 6.7 applies to an arbitrary pulse shape.

One other effect appears, and it is due to the form of the field envelope near its peak. In Fig. 6.21, the LATI peaks for the Gaussian pulse appear to have a better contrast than those for the sech pulse in Figure 6.20. This underlines

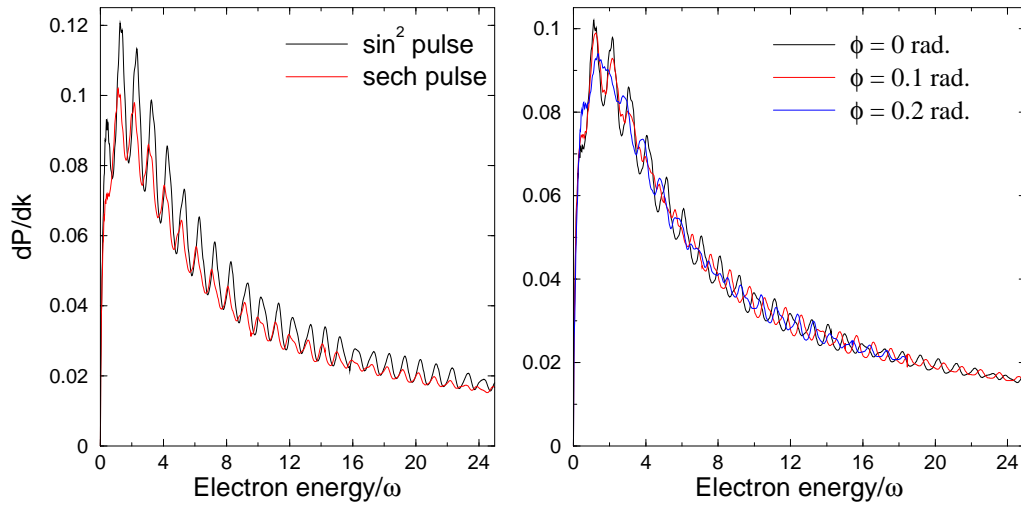


Figure 6.20: Left panel: angle-integrated ionization probabilities for He^+ in a 800 nm, 4-cycle \sin^2 pulse and a sech pulse with identical FWHM (in amplitude). The peak electric field is $E_0 = 0.4$ a.u. The phase is $\phi = 0$. Right panel: the probability for different pulse phases for the sech pulse.

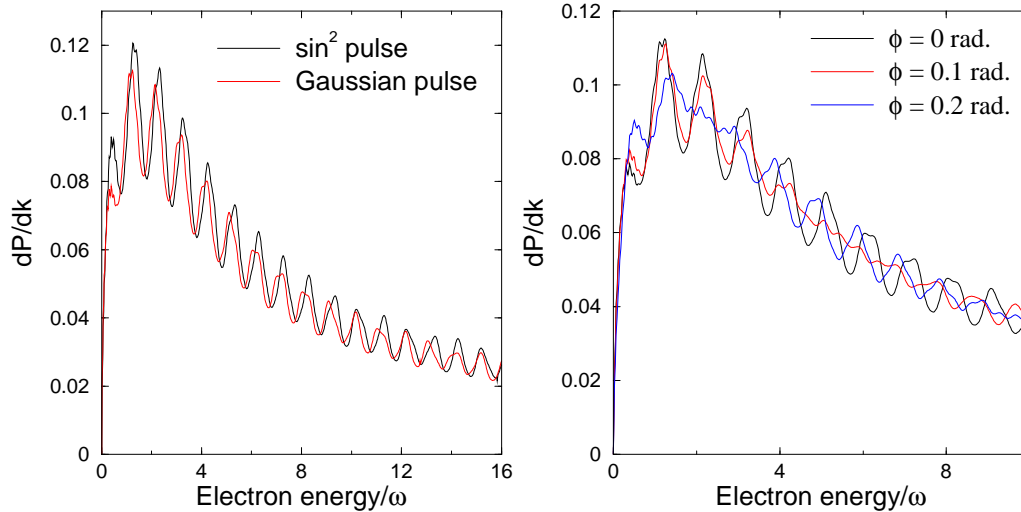


Figure 6.21: The same as in Fig. 6.20, but for a Gaussian pulse.

the influence of the field envelope: because the sech pulse has a faster decrease in amplitude near the peak of the envelope, the contribution of the saddle pair is smaller than for the case of a \sin^2 or Gaussian field. As a consequence, the LATI become less resolved from the background. The Gaussian pulse results agree better to the results obtained for the \sin^2 pulse. The reason is that the the two envelopes are nearly identical to the peak, provided they have the

same FWHM (in amplitude).

To conclude, we present results for the helium atom ($I_p = 0.903$ a.u.). Figure 6.22 (left panel) presents angle-integrated ATI spectra for a \sin^2 pulse and a sech pulse, with the same FWHM (in amplitude).

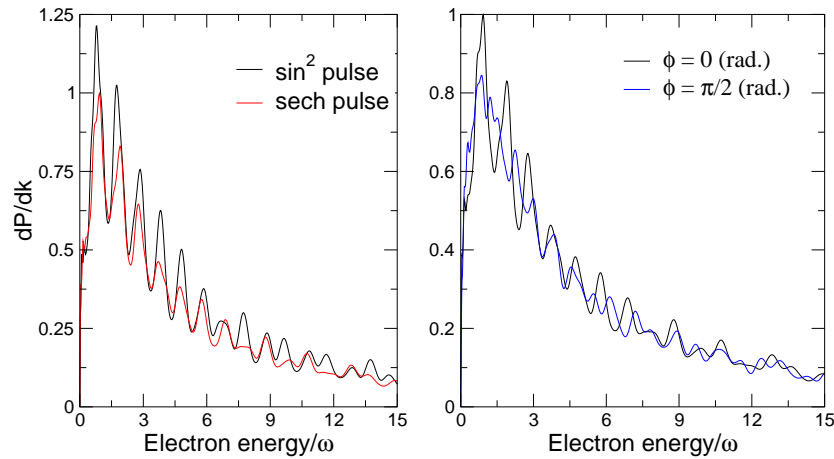


Figure 6.22: The same as in Fig. 6.20, but for helium, at intensity $I = 1 \times 10^{15}$ W/cm². (The Keldysh parameter $\gamma = 0.45$.)

Due to the lower ionization potential and the low intensity (where the ionization rates vary rapidly with the electric field amplitude), the effect of the envelope on the ATI spectrum is stronger than in the case of the He⁺ ion (see Figure 6.20). The right panel of Fig. 6.22 shows the angle-integrated spectra for two different field phases (namely for the case of the symmetrical and anti-symmetrical electric pulse). For the case of the anti-symmetrical electric field, the ATI spectrum is not flat, as expected; because of the low intensity, the asymmetry effects are not strong enough. To increase the intensity for this case would mean to approach the saturation intensity.

6.9 Field-phase dependence of emission asymmetry

Depending on the phase of the laser field, the emission of ionized electrons can occur in the positive direction of the polarization axis with different probability than in the negative direction. To assess the importance of the phase effects in the emission of electrons in the positive/negative direction we define the asymmetry:

$$R = \frac{P_+ - P_-}{P_+ + P_-}, \quad (6.11)$$

where P_+ is the total probability of emission in the positive direction of the polarization axis and P_- is the total probability in the negative direction. The

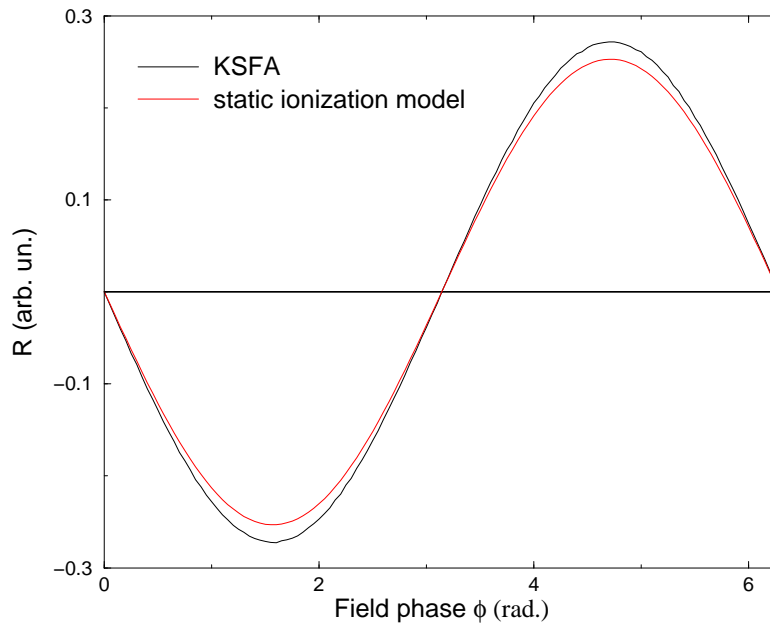


Figure 6.23: The asymmetry for direct ionization in He^+ for a peak electric field $E_0 = 0.4$ a.u., at a wavelength of 800 nm. The field is a \sin^2 field, encompassing four optical cycles. The two curves show the KSFA results and the prediction of a simple model based on the exact ionization rates in a static electric field.

emission probabilities are calculated using the KSFA model, by integrating over the energy of the ejected electron and over the emission angles corresponding to emission in the positive and negative direction, respectively. The black curve

in Figure 6.23 shows the variation of R with the field phase. Its variation is similar to a sinusoidal dependence and it reaches zero for phases $\phi = 0$ and $\phi = \pi$, when the vector potential $\mathbf{A}(t)$ is anti-symmetrical with respect to the middle of the pulse (thus, the electrons are emitted with the same probability in the positive/negative direction of the polarization axis).

From the Simpleman's model, at a time t_0 during the pulse, the electron is born in the continuum with a momentum along the polarization axis $p_1 = -A(t_0)$. The probability of emission depends exponentially on the modulus of the electric field $|E(t_0)|$. For a \sin^2 pulse, we have that $A(t, \phi) = -A(t, \pi + \phi)$ (ϕ is the field phase) and the same for the electric field. Therefore, by changing the phase with π , the emission of electrons changes direction. This explains why the asymmetry factor R in Figure 6.23 satisfies $R(\phi + \pi) = -R(\phi)$.

Starting from the Simpleman's model, we can calculate the total probabilities of emission in the positive/negative direction of the polarization axis as:

$$\begin{aligned} P_+ &= \int_0^{T_p} \Gamma_+(|E(t')|) dt' \\ P_- &= \int_0^{T_p} \Gamma_-(|E(t')|) dt'. \end{aligned} \quad (6.12)$$

In Eqs. (6.12), we assume that the depletion is negligible [i.e., $\int_0^t \Gamma(|E(t')|) dt' \ll 1$ at all times]. We define the ionization rate $\Gamma_+(|E(t)|)$ as being equal to the exact ionization rate in the static electric field of magnitude $|E(t)|$ if $A(t) < 0$, and zero if $A(t) > 0$. The latter condition ensures that the emission occurs in the positive direction: $p_1 = -A(t) > 0$. A similar definition is adopted for $\Gamma_-(|E(t)|)$, only the condition for emission in the negative direction reads $A(t) > 0$, such that $p_1 = -A(t) < 0$. The results are shown by the red curve in Fig. 6.23. They are in good agreement with the KSFA results which suggests that for the frequency and intensity used here, the ionization process can be approximated as adiabatic and occurs via tunneling.

A similar curve for the asymmetry factor R has been obtained in the work of Chelkowski, Bandrauk and Apolonski [99], based on *ab initio* calculations.

Their curve has an offset with a certain phase, so $R(\phi = 0) \neq 0$. This may be attributed to the Coulomb effects, which are only partially included in the KSFA model.

6.10 Comparison with *ab initio* results

In this section, we compare predictions of the KSFA model with exact results¹, aiming at establishing the differences between the two calculations. A possible way to improve this agreement is suggested.

The usual SFA model doesn't take into account the Coulomb interaction of the electron with the atomic core. The only place where the Coulomb interaction is taken into account is in the ground state used in the SFA amplitude. This ground state is the exact ground state of an electron bound by a Coulomb potential. The Krainov Coulomb-corrected SFA accounts for the influence of the Coulomb potential in the tunneling step of the ionizing electron; it reduces to a factor proportional to the Coulomb potential that multiplies the Volkov solution describing the final wavefunction of the electron. What it still uncorrected for the Coulomb interaction is the motion of the electron in the continuum. The reason is that due to the large electric field, the electron spends little time in the vicinity of the atomic core. The electron's large excursion amplitudes under the influence of the laser field only justifies neglecting the Coulomb interaction.

To assess the main differences between the Coulomb-corrected SFA and the exact results, we study some ATI spectra for two cases. Figure 6.24 shows the emission spectrum for an electron ejected at an angle $\theta = 10^\circ$ with the polarization axis, for a two-cycle pulse. The KSFA results agree quantitatively well with the results obtained from the integration of the Schrödinger equation. One should remember that the usual SFA model gives results that are

¹The author thanks Dr. R M Potvliege for the *ab initio* results, obtained using a numerical code courtesy of Dr. B Piraux.

consistently lower than those given by KSFA. Also, the ATI peaks energies as coming from the KSFA are slightly shifted in energy with respect to the exact results. The energy shift seems to increase with increasing electron energy.

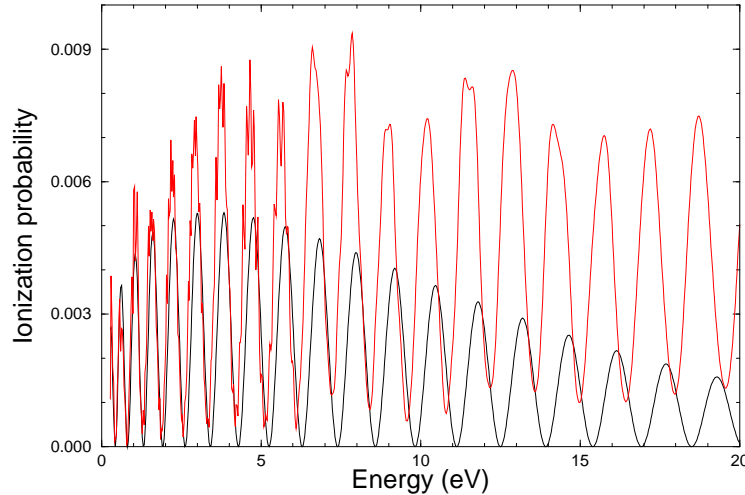


Figure 6.24: The ionization probability for an ejection angle $\theta = 10^\circ$ with respect to the polarization direction for a He^+ ion irradiated by a two-cycle \sin^2 pulse, with $\phi = \pi/2$. The intensity is 10^{16} W/cm^2 and the carrier wavelength is 400 nm. The red curve gives the *ab initio* results and the black curve the KSFA results.

Figure 6.25 shows the same as Figure 6.24, only for a longer pulse (four cycles). The general conclusions hold: the positions of the ATI peaks are energy-shifted, and the KSFA peaks show less structure than the exact peaks, obtained from the integration of the Schrödinger equation. Qualitatively, the number of ATI peaks is the same, only their energy differs from the exact value and the structure is less complicated.

Comparing to the exact spectra, one can say that the KSFA model is satisfactory to some extent, but there are differences in the structure of the ATI peaks and a small shift in ATI peak-energy is present. Better agreement is expected for higher laser intensities, or at least smaller frequencies. The comparison is hampered for the high intensity regime by a lack of data for the exact results. This is due to the increased numerical difficulty in solving the Schrödinger equation.

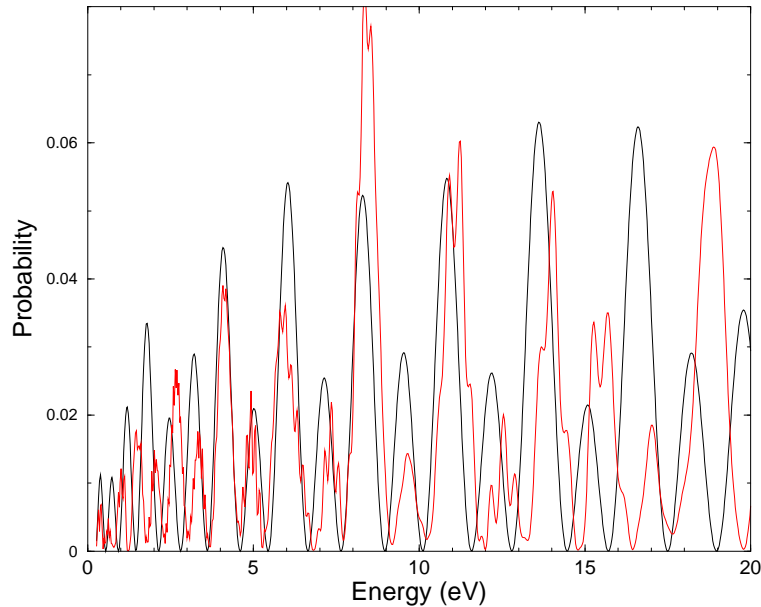


Figure 6.25: The ionization probability for an ejection angle $\theta = 10^\circ$ with respect to the polarization direction for a He^+ ion irradiated by a four-cycle \sin^2 pulse, with $\phi = \pi/2$. The intensity is 10^{16} W/cm^2 and the carrier wavelength is 400 nm. The red curve gives the *ab initio* results and the black curve the KSFA results.

The shift in the positions of the LATI peaks could be attributed to the bigger influence of the Coulomb interaction on the electron trajectories with the same final (low) momentum state. Some of the electron wavepackets created after tunneling through the potential barrier are ‘direct’, in the sense that after emission they propagate away from the atomic core. Other trajectories (presumably corresponding to the ‘indirect wavepackets’ of Ref. [4]) remain in the vicinity of the nucleus for a longer time; for these we expect the Coulomb interaction during the motion of the electron in the continuum, which is not included in the SFA model, to play a more important role .

A more detailed and complete comparison is presented in Figure 6.26: the density of probability in the momentum space² as obtained from the fully numerical solution of the Schrödinger equation is compared to the predictions of the KSFA model. This case differs from the ones studied so far in that the

²Courtesy of Dr. Bernard Piroux, from A. de Bohan, “Thèse de Doctorat”, Université Catholique de Louvain, 2001

ponderomotive energy is actually *smaller* than the binding energy ($U_p = 0.29$ and $I_p = 0.5$ atomic units, respectively). In this regime, it is expected that many electron trajectories will stay close to the atomic core, before leaving it, probably experiencing many interactions with the core [57], which agrees with the observation about the existence of the ‘indirect wavepackets’ of de Bohan *et al.* in Ref. [4]. Within the rescattering SFA model (using the atomic potential as expansion parameter), calculations done in Ref. [57] show that for the case $U_p < I_p$, the first-order term, or rescattering, is much larger than the zeroth-order term (which, Coulomb-corrected, gives the KSFA). This may indicate, according to [57] that the perturbation expansion in terms of the atomic potential actually breaks down, or converges more slowly. The Keldysh adiabaticity parameter $\gamma \approx 1$, so we are at the borderline between the tunneling and the multiphoton regime. In the *ab initio* calculation, the ATI peaks are much better defined than in the SFA model and the momentum distribution extends to slightly higher momentum values. Also, the up-down asymmetry along the polarization axis Oz is obvious, while the SFA gives a symmetrical distribution. So, the symmetry breaking could be attributed to effects related to the Coulomb interaction.

In the same figure, the comparison made in the upper picture with the results of a semiclassical approximation refers to an earlier version of the SFA, due to Faisal [63] and Reiss [64]. In the lower picture, we show the results of the KSFA model, for which an overall qualitative agreement can be seen. For the comparison to be more relevant, it requires a higher intensity case (where SFA is expected to be more accurate). At the same time, the numerical difficulty of the *ab initio* calculations increases considerably.

A last comparison is made for 4-cycle, \sin^2 pulse, at an intensity $I = 10^{16}$ W/cm², at 400 nm. We compare the *ab initio* results to the predictions of the KSFA model for a symmetrical (Figure 6.27) and anti-symmetrical pulse (Figure 6.28). The interference effect is visible in the *ab initio* calculation, but it is less obvious than in the KSFA calculation. This may be due to the shorter

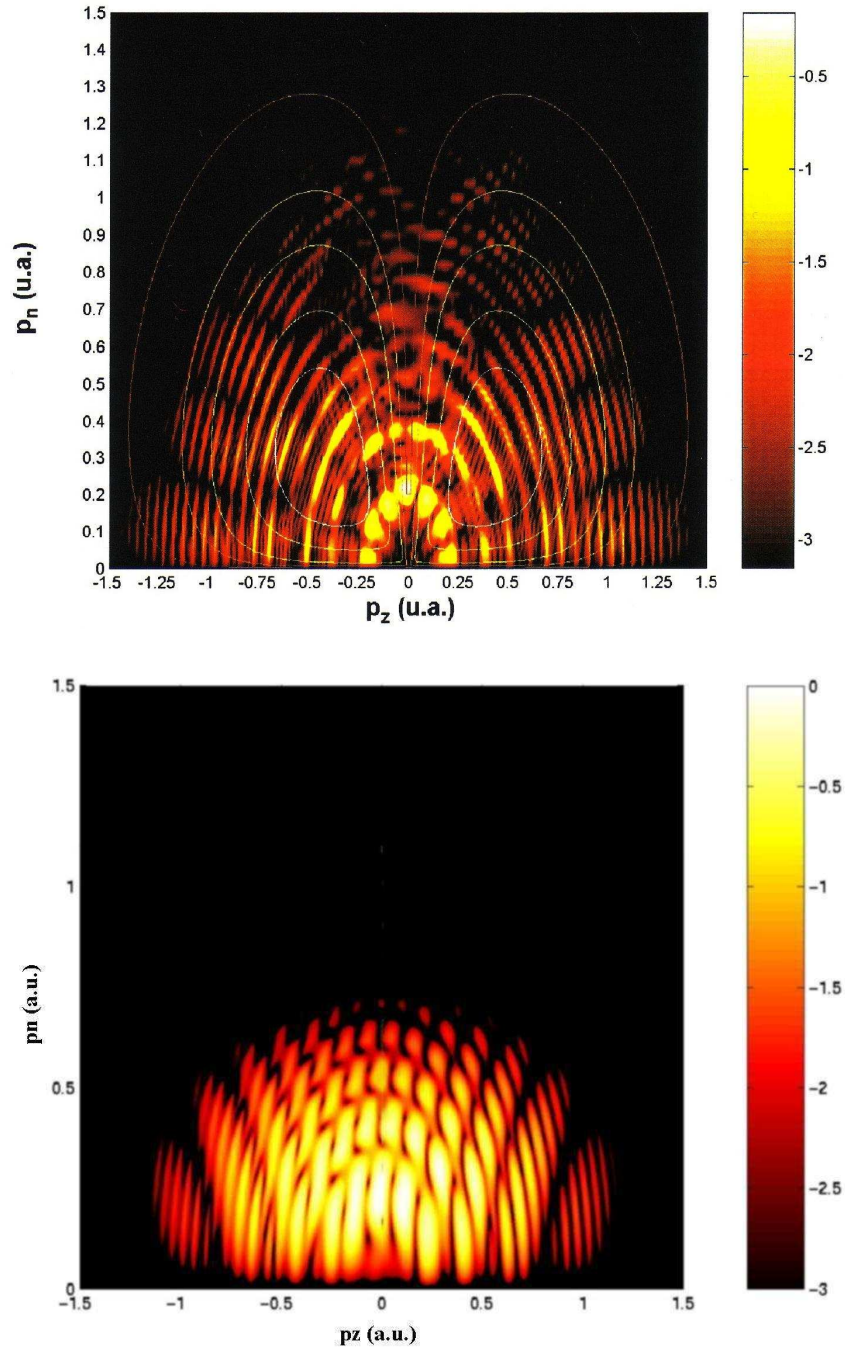


Figure 6.26: Emission probability in hydrogen, for ejection of the electron along the polarization axis with momentum p_z and in the perpendicular plane with momentum p_n . The laser has a peak intensity of 1.3×10^{14} W/cm², eight optical cycles and the wavelength is 800 nm. The electric field is symmetrical with respect to the middle of the pulse. The *ab initio* result is displayed in the upper panel [3], while the lower one shows the Coulomb-corrected SFA result. White lines in the top diagram are the predictions of the SFA in the velocity gauge [4].

wavelength of the field (half the value used in Section 6.8).

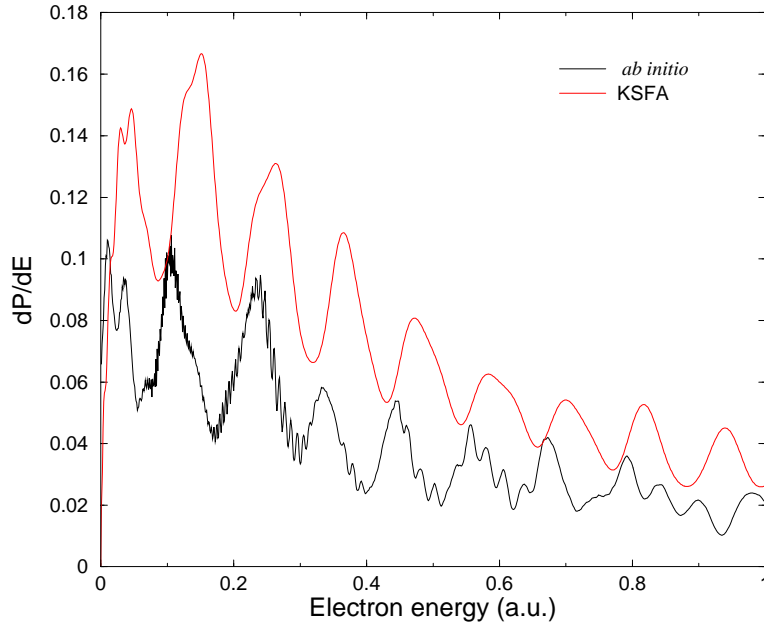


Figure 6.27: Angle-integrated ATI spectrum of He^+ irradiated by a 400 nm, 4-cycle \sin^2 laser pulse, with peak intensity of $1 \times 10^{16} \text{ W/cm}^2$. The field phase is $\phi = 0$. The *ab initio* result is compared to the KSFA result.

Based on the conclusions from this Section, it appears that the behavior of the ATI angle-integrated spectrum with the phase of the field described in Section 6.8 should remain valid.

6.11 Conclusions

In this chapter, we have presented predictions of the Krainov Coulomb-corrected SFA model (KSFA) for direct ionization in short laser pulses. The numerical results were obtained using the saddle point method. We showed that the agreement with the exact numerical results is excellent for the pulse parameters used.

The main point is the interference effect in the ATI spectrum and its dependence on the field phase. Only for a symmetrical electric field with respect to

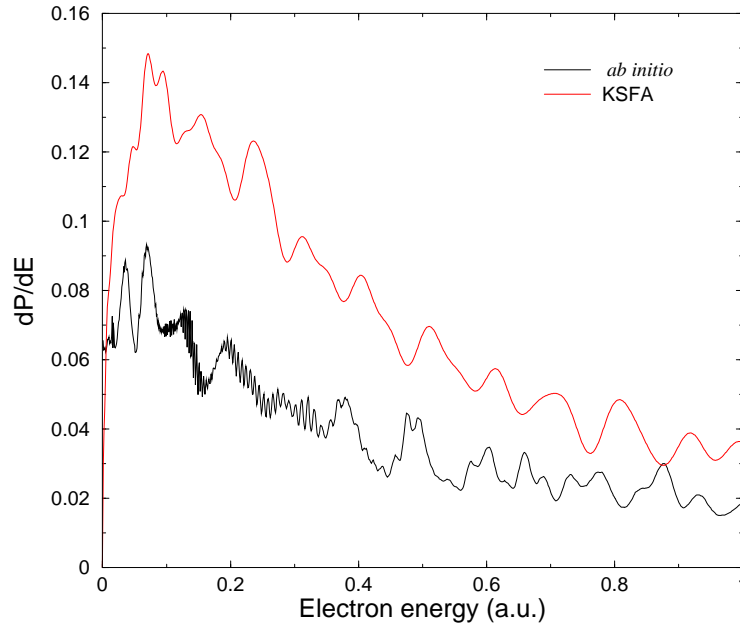


Figure 6.28: Comparison between the *ab initio* result and the KSFA result. The pulse parameters are the same as in Fig. 6.27, only the electric field is asymmetrical: $\phi = \pi/2$.

the middle of the pulse there are LATI peaks in the angle-integrated spectrum. Otherwise, the spectrum is flat for field phases departing from the zero value. This may suggest a way to measure the absolute phase of a short laser pulse.

The analysis of the influence of pulse parameters, as pulse duration and intensity, shows that the phase sensitivity of LATI manifests only for a small number of optical cycles. Increasing the pulse duration results in losing the phase effects, as the ATI spectrum begins to resemble the one for the stationary field.

We have also analyzed the total ionization probability and compared it to the results obtained from integration over the pulse duration of the exact ionization rates in static electric field. The agreement of the KSFA model is much better than for the usual SFA.

The last part of the chapter compares angle-resolved LATI spectra from the KSFA model to the exact results from the numerical integration of the Schrödinger

equation. We show that the agreement is good as order of magnitude, but there is a shift in the energies of the LATI and less structure of the peaks for the KSFA. The differences may originate in the neglect of the Coulomb interaction for the motion of the electron after tunneling. A more accurate SFA would have to incorporate these corrections for the motion of the electron in the continuum.

Chapter 7

Conclusions

This work is concerned with the study of the predictions of the strong field approximation model (SFA) for harmonic generation (HG) and above threshold ionization (ATI) in simple atomic systems. For the case of HG, the non-dipole, non-relativistic approach of Ref. [22] is shown to be in good agreement with the fully relativistic calculation of Refs. [1, 32] in the dynamical regime where relativistic effects are not dominant. The non-dipole approach is based on including the $1/c$ correction to the electric and magnetic field components of the laser beam, which raises the natural question of the inclusion of the next orders at higher intensities. The answer can be based on two remarks: (i) The relativistic mass effect is of order $1/c^2$; by not including it, the model becomes explicitly non-relativistic, and therefore its predictions cannot be expected to be correct. The fact that the first relativistic correction is of order $1/c^2$ allowed in the first place the existence of the intermediate non-relativistic, non-dipole regime, where $1/c^2$ corrections are negligible, but $1/c$ corrections are not. (ii) Solving the non-relativistic Schrödinger equation for a vector potential $\mathbf{A}(\omega t - \mathbf{k} \cdot \mathbf{r})$ (hence including *all* orders of $1/c$) is shown to predict energy bands [100, 101] instead of a continuum spectrum for a free electron in the field. The energy bands are not present in the relativistic formulation.

We can conclude that the $1/c$ correction is the only possible non-dipole extension in this form of the SFA, without directly contradicting the relativistic

theory. Its analytical simplicity led to a natural extension of the Simpleman's model in the non-dipole regime. This suggests a deeper connection between classical trajectories and the semi-classical approximation, on which the SFA is based. A further understanding may open the way to control the atomic processes by controlling the few parameters that govern the contributing trajectories [11].

Regarding ATI, the SFA model (including rescattering) qualitatively reproduces the experimental data well and helps in elucidating the role of different variables, related to the laser pulse or to the atomic species. Quantitatively, only short range interactions (such as for the case of negative ions) can be modelled in a satisfactory way. We discuss a version of the Coulomb correction of the SFA as proposed by Krainov (KSFA), and show it to be an improvement for the long range interactions, but the overall level of agreement with *ab initio* results under general pulse conditions remains an open question. A possible investigation could analyze when the semi-classical propagator, including the interaction of the electron with the atomic core, is a sufficiently accurate approximation to the exact propagator. Furthermore, in the same manner as the KSFA corrects for the tunneling step of the process, a correction for the Coulomb interaction during the motion of the electron in the continuum can be done.

Predictions of the KSFA model for ionization in short laser pulses reveal interesting interference features, much richer than for the stationary field. Electron wavepackets are ejected from the atom at times when the electric field is close to a maximum, and they interfere. Because the magnitude of each interference term that corresponds to a certain emission time depends exponentially on the electric field amplitude when the electron is 'born' in the continuum, the modulations in the ATI spectrum will depend essentially on the pulse parameters, such as shape, carrier phase or duration. It is the interplay between all these parameters that shape the ATI distribution spectrum, making it more complex than for a stationary field where the carrier phase does not play a role

and there are only two interfering wavepackets per optical cycle. Brief comparisons with *ab initio* spectra of the KSFA are in good qualitative agreement and of the same order of magnitude, suggesting that the interference effects are genuine and should also be present in *ab initio* results. The latter are difficult to obtain numerically at the relatively high intensities we employed here. The confirmation of such effects is still a matter for future research.

To finalize, we hope that the present work would help in a better understanding of the predictive power and limits of the SFA model and its improvements for the analysis of HG and ATI.

Appendix A

The dipole Gordon-Volkov solution

The problem of a charged particle in an external electromagnetic field was first solved by W Gordon [102] and D M Volkov [61]. Below, we reproduce their result and introduce notations used in this work.

Consider a charged particle in an external electromagnetic field. We try to solve the associated quantum mechanical problem (i.e., finding the wave function of the particle) in the dipole approximation.

By ‘dipole approximation’ we understand that for the terms in the hamiltonian describing the interaction with the field, we neglect the dependance on the spatial position of the particle, meaning that the field changes over a characteristic length much bigger than the amplitude of the particle motion. Usually this is the case for low frequency radiation (long wavelength). As long as the particle doesn’t move over extended regions in space, the approximation remains valid.

For describing the electromagnetic field, we choose to work in the Coulomb gauge, in which the field with the propagation vector \mathbf{k} is completely described by the magnetic vector potential $\mathbf{A}(t, \mathbf{k} \cdot \mathbf{r})$ and the electrostatic potential ϕ is set to zero. The magnetic vector potential has to satisfy the condition of being a transverse field : $\mathbf{A} \cdot \mathbf{k} = 0$.

In the velocity gauge and the dipole approximation, the Schrödinger equation reads:

$$i\frac{\partial}{\partial t}|\psi(t)\rangle = \frac{1}{2}[-i\nabla + \mathbf{A}(t)]^2|\psi(t)\rangle. \quad (\text{A.1})$$

The easiest way to solve it is to choose the momentum representation for the wave function $\tilde{\psi}(t, \mathbf{p}) = \langle \mathbf{p}|\psi(t)\rangle$ (which corresponds to solving the equation in the Fourier transformed form). From

$$i\frac{\partial}{\partial t}\tilde{\psi}(t, \mathbf{p}) = \frac{1}{2}[\mathbf{p} + \mathbf{A}(t)]^2\tilde{\psi}(t, \mathbf{p}),$$

one obtains :

$$\tilde{\psi}(t, \mathbf{p}) = \exp\left\{-\frac{i}{2}\int^t[\mathbf{p} + \mathbf{A}(\tau)]^2 d\tau\right\}.$$

Taking the inverse Fourier transform of the above, we obtain the solution of (A.1) :

$$\psi_{\mathbf{p}}(t, \mathbf{r}) = C \exp\left\{i\mathbf{p} \cdot \mathbf{r} - \frac{i}{2}\int^t[\mathbf{p} + \mathbf{A}(\tau)]^2 d\tau\right\},$$

with C a normalization constant.

From the normalization condition :

$$\langle \psi_{\mathbf{p}}(t, \mathbf{r})|\psi_{\mathbf{p}'}(t, \mathbf{r})\rangle = \delta(\mathbf{p} - \mathbf{p}'),$$

we find the constant $C = (2\pi)^{-3/2}$.

Putting it all together, the Volkov solution [61] for a plane wave in the dipole approximation and using the velocity gauge reads:

$$\psi_{\mathbf{p}}^{Vv}(t, \mathbf{r}) = (2\pi)^{-3/2} \exp\left\{i\mathbf{p} \cdot \mathbf{r} - \frac{i}{2}\int^t[\mathbf{p} + \mathbf{A}(\tau)]^2 d\tau\right\}. \quad (\text{A.2})$$

To go to the length gauge, one can use the unitary transformation:

$$|\psi^{Vl}(t)\rangle = \exp[i\mathbf{A}(t) \cdot \mathbf{r}] |\psi^{Vv}(t)\rangle$$

and obtains

$$\psi_{\mathbf{p}}^{Vl}(t, \mathbf{r}) = (2\pi)^{-3/2} \exp\left\{i[\mathbf{p} + \mathbf{A}(t)] \cdot \mathbf{r} - \frac{i}{2}\int^t[\mathbf{p} + \mathbf{A}(\tau)]^2 d\tau\right\}. \quad (\text{A.3})$$

A general way to write the Volkov solutions in both gauges is:

$$\psi_{\mathbf{p}}^V(t, \mathbf{r}) = (2\pi)^{-3/2} \exp \left\{ i\mathbf{\Pi}_{\mathbf{p}}^V(t) \cdot \mathbf{r} - \frac{i}{2} \int^t [\mathbf{p} + \mathbf{A}(\tau)]^2 d\tau \right\}, \quad (\text{A.4})$$

where $\mathbf{\Pi}_{\mathbf{p}}^V(t)$ is the momentum eigenvalue for the Volkov solution and reads:

$$\begin{aligned} \mathbf{\Pi}_{\mathbf{p}}^{Vl}(t) &\equiv (-i\nabla)\psi_{\mathbf{p}}^{Vv}(t, \mathbf{r}) = \mathbf{p}, \quad (\text{length gauge}) \\ \mathbf{\Pi}_{\mathbf{p}}^{Vv}(t) &= \mathbf{p} + \mathbf{A}(t) \quad (\text{velocity gauge}). \end{aligned} \quad (\text{A.5})$$

Appendix B

Non-dipole non-relativistic Volkov solution

For a charged particle in an external electromagnetic field, the calculation of the wavefunction including first order corrections in $1/c$ (c is the speed of light), was first done by Kylstra, Potvliege and Joachain in [22].

The non-dipole non-relativistic Volkov Green's function can be expressed as

$$G_V^{(+)}(\mathbf{r}, t; \mathbf{r}', t') = -i\theta(t - t') \int d\mathbf{p} \Psi_{\mathbf{p}}^L(\mathbf{r}, t) [\Psi_{\mathbf{p}}^L(\mathbf{r}', t')]^* , \quad (\text{B.1})$$

where the function $\Psi_{\mathbf{p}}^L(\mathbf{r}, t)$ is a solution of the time dependent Schrödinger equation (TDSE) (2.4) with $V(r) = 0$. Calling $\Psi_{\mathbf{p}}(\mathbf{r}, t)$ the solution of the TDSE (2.3) with $V(r) = 0$, introducing the wave function $\Psi'_{\mathbf{p}}(\mathbf{r}, t)$ by

$$\Psi_{\mathbf{p}}(\mathbf{r}, t) = \exp\left(\frac{i}{c} \left[-i\nabla \cdot \mathbf{A}(\omega t) + \frac{1}{2}A^2(\omega t) \right] (\hat{\mathbf{k}} \cdot \mathbf{r})\right) \Psi'_{\mathbf{p}}(\mathbf{r}, t) , \quad (\text{B.2})$$

and recalling that $\nabla \cdot \mathbf{A}(\omega t)$ commutes with $\hat{\mathbf{k}} \cdot \mathbf{r}$, it is seen that

$$i\frac{\partial}{\partial t} \Psi'_{\mathbf{p}}(\mathbf{r}, t) = \frac{1}{2} \left(-i\nabla + \mathbf{A}(\omega t) + \frac{1}{c} \left[-i\nabla \cdot \mathbf{A}(\omega t) + \frac{1}{2}A^2(\omega t) \right] \hat{\mathbf{k}} \right)^2 \Psi'_{\mathbf{p}}(\mathbf{r}, t) . \quad (\text{B.3})$$

The Hamiltonian operator in equation (B.3) commutes with the momentum operator, so that the TDSE is easily solved. Transforming back to the length

gauge, the non-dipole Volkov wave function reads

$$\Psi_{\mathbf{p}}^{\text{L}}(\mathbf{r}, t) = \frac{1}{(2\pi)^{\frac{3}{2}}} \exp \left(i\boldsymbol{\pi}(\mathbf{p}, t) \cdot \mathbf{r} - \frac{i}{2} \int^t dt'' [\boldsymbol{\pi}(\mathbf{p}, t'')]^2 \right). \quad (\text{B.4})$$

where $\boldsymbol{\pi}(\mathbf{p}, t)$ is defined in equation (2.8). The non-dipole Volkov wave function (B.4) is also readily obtained by expanding the relativistic Volkov wave function in powers of $1/c$ and neglecting terms of orders $1/c^2$ and higher. It reduces to the familiar non-relativistic, dipole Volkov wave function when $1/c \rightarrow 0$.

Appendix C

Singular asymptotics

When we apply the usual saddle point formula, we assume that the exponential is of Gaussian form and the pre-exponential factors have no singularities. The presence of a singularity in the pre-exponential term (e.g., a pole or a branch point) makes the analysis difficult, especially if the singularity is close to one of the saddle points. A way to deal with this is to use what is called uniform approximations; they are generalizations of the classical saddle point formulae which simplify to the standard form, under appropriate conditions (for example, when the singularity and the saddle point are far apart, as implicitly considered in the non-uniform saddle methods).

In our case (the dipole moment in the context of harmonic generation), one has to deal with the situation when the saddle point is also a pole of first order in the pre-exponential factor; i.e., we have to consider asymptotic expansions for model integrals

$$J_\nu = \int \frac{\exp[-\lambda f(x)]}{(x - x_0)^\nu} dx; \quad \nu > 0, \quad (\text{C.1})$$

with the first term of the uniform asymptotic expansion (from Appendix B in [68])

$$J_\nu \simeq i^\nu \frac{\Gamma(\nu/2)}{2\Gamma(\nu)} \left(\frac{2\pi}{\lambda f''(x_0)} \right)^{1/2} [2\lambda f''(x_0)]^{\nu/2} \exp[-\lambda f(x_0)], \quad (\text{C.2})$$

where $\Gamma(x)$ is the gamma function. For more details and next order terms

see the book of Borovikov [39]. For $\nu = 0$ one recovers, of course, the usual standard saddle point formula.

Appendix D

Coulomb corrected ionization rates

This appendix details the calculation done in [85] and corrects the misprints in the article.

D.1 Tunnelling ionization by linearly polarized radiation

In the limit of a weak field $E_0 \ll Z^3$ when tunneling ionization is realized, we can simplify the general expression (5.27) for the energy and angular distribution of electrons by using the saddle point for the calculation of the integral (i.e., finding its asymptotic expansion within the constraints on the arguments imposed by the tunneling regime). The actual integral of the action can be written as a generalized Bessel function (for a detailed discussion see [103]).

The saddle points satisfy the equation :

$$S'(t_s) \equiv p_{\perp}^2 + (p_{\parallel} - E_0/\omega \sin \omega t)^2 + I_p = 0 \quad (\text{D.1})$$

and in the interval $[0, 2\pi/\omega]$ are given by :

$$t_s^{(1)} = \frac{1}{\omega} \arcsin \left[\frac{\omega}{E_0} (p_{\parallel} + i\sqrt{p_{\perp}^2 + Z^2}) \right] \quad (\text{D.2a})$$

$$t_s^{(2)} = \pi/\omega - (t_s^{(1)})^*. \quad (\text{D.2b})$$

For momentum $p \ll Z$, one can see that the real part of the saddle times corresponds to $t = 0$ and $t = \pi/\omega$, when the electric field is maximal.

The interference between these two saddle points is responsible for oscillations in the photoelectron angular distribution. From the theory of the saddle approximation, the integral in 5.27 can be written as:

$$\mathcal{A} = \int_0^{2\pi/\omega} \exp[iS(t)] dt = \sum_{1,2} \sqrt{\frac{2\pi i}{S''(t_s)}} \exp[iS(t_s)]. \quad (\text{D.3})$$

Using the energy conservation for the absorption of N photons, we note that

$$S(\pi/\omega - x^*) = N\pi - S(x)^* \quad (\text{D.4})$$

$$S''(\pi/\omega - x^*) = -S''(x)^*,$$

which means together with (D.2) that the contribution from the second saddle is just the complex conjugate of the contribution from the first, apart from a phase factor $\exp(iN\pi)$. From

$$\rho e^{i\phi} + e^{iN\pi} \rho e^{-i\phi} = 2\rho e^{iN\pi/2} \cos(\phi - \frac{n\pi}{2}),$$

with $q_s \equiv \rho e^{i\phi} \equiv \sqrt{\frac{2\pi i}{S''(t_s^{(1)})}} \exp[iS(t_s^{(1)})]$ we get from (D.3):

$$|\mathcal{A}|^2 = 2|q_s|^2 \left\{ 1 + (-1)^N \cos[2 \arg(q_s)] \right\}. \quad (\text{D.5})$$

To carry out the full calculation, we need expanding the expressions in powers of the electric field amplitude E_0 . For the saddle point, we obtain:

$$t_s^{(1)} = \frac{p_{\parallel} + i\sqrt{p_{\perp}^2 + Z^2}}{E_0} + \mathcal{O}\left(\frac{1}{E_0^3}\right).$$

Note that for low momentum, the real part of one saddle is close to zero, while for the other will be close to half of the period of the oscillating field (see above comments).

The second derivative of the action (after expanding in power series in electron momenta and inverse of powers of the electric field amplitude) is given by:

$$S''(t_s^{(1)}) = iFZ \left(1 + \frac{p_\perp^2}{2Z^2} \right) + \mathcal{O}\left(\frac{1}{E_0}\right). \quad (\text{D.6})$$

(Remember that the probability for the electron to have a momentum perpendicular to the polarization direction is very small, as we will see below).

Let us calculate the exponent in the saddle point approximation:

$$\begin{aligned} \text{Re}[S(t_s^{(1)})] &= \frac{Fp_\parallel}{\omega^2} + p_\parallel \frac{p_\parallel^2 + 3(p_\perp^2 + Z^2)}{6E_0} + \mathcal{O}\left(\frac{1}{E_0^3}\right) \\ \text{Im}[S(t_s^{(1)})] &= \frac{(p_\perp^2 + Z^2)^{3/2}}{3E_0} - \frac{\omega^2(p_\perp^2 + Z^2)^{3/2}}{30E_0^3} (-5p_\parallel^2 + p_\perp^2 + Z^2) + \mathcal{O}\left(\frac{1}{E_0^5}\right) \end{aligned} \quad (\text{D.7})$$

Further, expand D.7 in powers of the momenta, and keep the lowest (quadratic) terms:

$$\text{Re}[S(t_s^{(1)})] = \frac{Fp_\parallel}{\omega^2} \left[1 + \frac{\gamma^2}{2} + \frac{\gamma^2}{6} \frac{p^2 + 2p_\perp^2}{Z^2} \right] + \mathcal{O}\left(\frac{1}{E_0^3}\right) \quad (\text{D.8a})$$

$$\text{Im}[S(t_s^{(1)})] = \frac{Z^3}{3E_0} \left(1 - \frac{\gamma^2}{10} \right) + \frac{Z}{2E_0} p_\perp^2 + \frac{\gamma^3}{6\omega} p_\parallel^2 \quad (\text{D.8b})$$

Here $\gamma = \omega Z/E_0$ is the Keldysh adiabaticity parameter.

The complex argument of the saddle contribution from the first saddle point originates from the real part of the action and half the argument of the second derivative of the action (see D.5); because the second derivative comes as $\sqrt{i/S''}$, its dominant contribution in the tunneling limit is real [see (D.6)], so that the argument of the saddle interference term is given by the real part of

the action only. In conclusion:

$$\left| \int_0^{2\pi/\omega} dt \exp[iS(t)] \right|^2 = \frac{4\pi}{ZF} \exp \left[-\frac{2Z^3}{3E_0} \left(1 - \frac{\gamma^2}{10}\right) - \frac{Z}{E_0} p_\perp^2 - \frac{\gamma^3}{3\omega} p_\parallel^2 \right] \left\{ 1 + (-1)^N \cos \left[2\frac{Zp_\parallel}{\omega\gamma} \left(1 + \frac{\gamma^2}{2}\right) + \mathcal{O}\left(\frac{1}{E_0}\right) \right] \right\} \quad (\text{D.9})$$

If we choose to expand the action in momenta only and not in powers of the electric field strength E_0 , the interference term would be $\frac{2Zp_\parallel}{\omega\gamma} \sqrt{1 + \gamma^2}$ [compare to Eq. (42) in [68], where the authors do a similar calculation].

Integrating the distribution (which doesn't depend on ϕ) over the momentum solid angle

$$d\Omega = \sin\theta d\theta d\phi \simeq \theta d\theta d\phi$$

neglecting the highly oscillating cos function and remembering that

$$p_\perp \simeq p\theta \text{ and } p_\parallel \simeq p,$$

we obtain (up to a numerical factor which will be included in the end to avoid confusion):

$$\int p_N \left| \int_0^{2\pi/\omega} dt \exp[iS(t)] \right|^2 d\Omega = \frac{2}{p_N} \left(\frac{2\pi}{Z}\right)^2 \exp \left[-\frac{2Z^3}{3E_0} \left(1 - \frac{\gamma^2}{10}\right) - \frac{\gamma^3}{3\omega} p^2 \right] \quad (\text{D.10})$$

The integration over the p_\perp was done for θ in small intervals around $\theta = 0$ and $\theta = \pi$, where the distribution decreases exponentially (the electron emission can occur with equal probabilities in both directions of the axis of polarization); the integral can be thus replaced by two times a Gaussian-like integral.

When the frequency of the field decreases $\omega \rightarrow 0$ the momentum spectrum of the ejected electrons becomes continuous, so we can replace the summation over the number of absorbed photons N according to the rule:

$$\sum_N = \int w dN = \int (w/\omega) d(N\omega) = \int_0^\infty (w/\omega) p dp,$$

where we used the energy-conservation law.

To conclude, in the tunneling regime the sum over the multiphoton contributions reduces to:

$$\sum_N p_N \left| \int_0^{2\pi/\omega} dt \exp[iS^{(N)}(t)] \right|^2 = 2 \frac{(2\pi)^3 E_0}{(2\omega Z)^2} \sqrt{\frac{3E_0}{\pi Z^3}} \exp \left[-\frac{2Z^3}{3E_0} \left(1 - \frac{\gamma^2}{10}\right) \right] \quad (\text{D.11})$$

From 5.27, we can write the limit ionization rate in the tunneling regime:

$$w_l = \frac{4Z^5}{E_0} \sqrt{\frac{3E_0}{\pi Z^3}} \exp \left[-\frac{2Z^3}{3E_0} \left(1 - \frac{\gamma^2}{10}\right) \right] \quad (\text{D.12})$$

We can see that the ADK [90] result is obtained exactly for the ionization rate. The ionization rate in the field of linear polarization w_l is connected to the ionization rate in the field of circular polarization w_c by the well-known relation

$$w_l = \left(\frac{3E_0}{\pi Z^3} \right)^{1/2} w_c.$$

This result is correct only in the tunneling regime, so $w_l \ll w_c$. In the case of barrier-suppression ionization, both ionization rates are of the same order of magnitude.

D.2 Tunnelling ionization by circularly polarized radiation

In the tunneling limit, we have the adiabatic Keldysh parameter $\gamma = \omega Z/E_0 \ll 1$ and the field strength is small compared to the barrier suppression field strength. Therefore we can use the asymptotic representation for the Bessel function:

$$J_N(N/\cosh \alpha) = (2\pi N \tanh \alpha)^{-1/2} \exp[N(\tanh \alpha - \alpha)]. \quad (\text{D.13})$$

Instead of the angle θ between the direction of propagation of the ejected electron and the direction of propagation of the polarized wave, we will use the small angle

$$\psi = \frac{\pi}{2} - \theta,$$

between the ejected electron and the plane of polarization. Further, we introduce the small number

$$\delta N = N - E_0^2/\omega^3 - I_p/\omega. \quad (\text{D.14})$$

Comparing the argument of the asymptotic Bessel function representation with the argument as appears in (5.32) with p_N given by the energy conservation condition, replacing $N = N(\delta N)$ from (D.14) and θ with ψ as above, we obtain:

$$\cosh \alpha = \frac{1 + \frac{\omega^3}{E_0^2} \delta N + \frac{1}{2} \left(\frac{\omega Z}{E_0} \right)^2}{\cos(\psi) \sqrt{1 + \frac{2\omega^3}{E_0^2} \delta N}}.$$

Expanding in power series of inverse of the field strength $1/E_0$ and $|\delta N| \ll 1$:

$$\alpha \simeq \frac{Z \omega}{E_0} - \frac{Z^3 \omega^3}{24 E_0^3} - \frac{Z \delta N \omega^4}{2 E_0^3} + \frac{\delta N^2 \omega^5}{2 E_0^3 Z} + \left[\frac{E_0}{2Z\omega} + \mathcal{O}\left(\frac{1}{E_0}\right) \right] \psi^2 + \mathcal{O}\left(\frac{1}{E_0^3}, \psi^4\right).$$

Following the same changes in the exponential of the Bessel asymptotic expansion, we get to the same order (after constructing a binomial expression in δN):

$$2N(\tanh \alpha - \alpha) \simeq -\frac{2Z^3}{3E_0} \left(1 - \frac{\gamma^2}{15}\right) - \frac{ZF}{\omega^2} \psi^2 - \frac{Z\omega^4}{E_0^3} \left(\delta N - \frac{Z^2}{6\omega}\right)^2 \quad (\text{D.15})$$

The pre-exponential factor in (D.13) has the series expansion:

$$N \tanh \alpha = \frac{FZ}{\omega^2} + \mathcal{O}(\psi^2).$$

Before putting it all together, we write one last expansion:

$$p_N = \frac{E_0}{\omega} \sqrt{1 + \frac{2\omega^3}{E_0^2} \delta N} \simeq \frac{E_0}{\omega} + \mathcal{O}\left(\frac{1}{E_0^2}, \delta N\right)$$

and the ionization rate (5.32) becomes:

$$dw_c/d\Omega_p = \frac{2\omega Z^6}{\pi^2 E_0^2} \sum_{N \geq N_0} \exp \left[-\frac{2Z^3}{3E_0} \left(1 - \frac{\gamma^2}{15}\right) - \frac{ZF}{\omega^2} \psi^2 - \frac{Z\omega^4}{E_0^3} \left(\delta N - \frac{Z^2}{6\omega}\right)^2 \right]. \quad (\text{D.16})$$

One can see that the emission of electrons has a maximum in energy approximately at

$$\frac{p_{max}^2}{2} \simeq \frac{E_0^2}{2\omega^2} + \frac{2}{3}I_p$$

(see Fig. 1 in [104]) and that the angular distribution decreases exponentially as moving away from the polarization plane.

We also quote the result:

$$\sum_{N \geq N_0} p_N J_N^2 \left(\frac{p_N E_0 \sin \theta}{\omega^2} \right) \xrightarrow{\text{tunneling limit}} \frac{E_0}{2Z\omega} \sqrt{\frac{E_0}{\pi Z}} \exp \left[-\frac{2Z^3}{3E_0} \left(1 - \frac{\gamma^2}{15} \right) - \frac{ZF}{\omega^2} \psi^2 \right] \quad (\text{D.17})$$

Summing over the number of absorbed photons in (D.16):

$$dw_c = \frac{2Z^6}{\pi\omega} \frac{1}{\sqrt{\pi Z E_0}} \exp \left[-\frac{2Z^3}{3E_0} \left(1 - \frac{\gamma^2}{15} \right) - \frac{ZF}{\omega^2} \psi^2 \right] \cos \psi d\psi d\phi. \quad (\text{D.18})$$

and finally, the total ionization rate (identical to the ADK result, as expected, for ionization of the s states):

$$w_c = \frac{4Z^5}{E_0} \exp \left[-\frac{2Z^3}{3E_0} \left(1 - \frac{\gamma^2}{15} \right) \right]. \quad (\text{D.19})$$

The presence of the Keldysh factor γ in (D.19) is often referred to as an adiabatic correction to the static field ionization rate.

Appendix E

Computational methods

E.1 Statement of the problem

In order to calculate quantities such as ionization probabilities (for short pulses) and ionization rates (for stationary pulses) in the framework of the SFA (strong field approximation), one has to deal, up to a numerical factor, with integrals of the form:

$$L = \int_0^{T_p} dt \frac{\exp[iS(\mathbf{p}, t)]}{S'(t)}, \quad (\text{E.1})$$

or

$$V = \int_0^{T_p} dt \exp[iS(\mathbf{p}, t)], \quad (\text{E.2})$$

where T_p is the duration of the laser pulse.

The two expressions represent the Keldysh-like transition amplitudes in length gauge (E.1) and velocity gauge (E.2). The latter is identical (again up to a numerical factor) to the Krainov Coulomb corrected ionization amplitude (which is the same in both the length gauge and velocity gauge).

One common feature of the two forms is the presence of the oscillatory term $\exp[iS(\mathbf{p}, t)]$, where $S(\mathbf{p}, t) = \int_0^t \{[\mathbf{p} + A(t')]^2/2 + I_p\} dt'$ is the modified classical action of an electron with final canonical momentum (or the field-averaged value of the kinetic momentum) \mathbf{p} , in a linearly polarized electromagnetic field

within the dipole approximation. The atom/ion ionization potential is I_p .

Because $|S(\mathbf{p}, t)| \gg 1$, we can apply the saddle point method to obtain numerical estimates for the integrals. The advantage of the saddle point method is that once the saddle points are calculated, the integrals can be written as a sum over just a few saddle points. A short description of the saddle method is given in the next section.

The higher the values of the classical action, the higher the accuracy of the saddle point estimate and the more difficult the calculation of the integral along the real axis is. This makes the saddle point method best suited for our task, from the point of view of accuracy and duration of the calculation.

E.2 Saddle point method

E.2.1 General introduction

The theory behind the saddle point method relies on the possibility of changing the path of integration in the complex plane taking into account the possible singularities of the integrand inside the contour, according to the Cauchy residue theorem. The path is deformed such as to go through the so-called critical points of the integrand (in our case the end points of integration and the points where the derivative of the action is zero). A second important detail is that in the vicinity of the saddle point, the exponential can decay or increase, depending on the orientation of the path in the complex plane crossing the saddle or its vicinity. Choosing the path on which the integrand decays exponentially assures that the main contribution to the integral will come from the vicinity of the saddle. All contributing saddles must be summed over.

For the integrals (E.1) and (E.2), we can write the asymptotic expansions (only

the leading terms are given):

$$V = \sum_{n_s=1,2,\dots} \exp[iS(t_s)] \sqrt{\frac{2\pi i}{S''(t_s)}} + \text{boundary terms}, \quad (\text{E.3})$$

and

$$L = \sum_{n_s=1,2,\dots} \pi i \frac{\exp[iS(t_s)]}{S''(t_s)} + \text{boundary terms}. \quad (\text{E.4})$$

The momentum \mathbf{p} is still present in the expression of the action, but we choose not to write it for simplicity.

The boundary terms are the asymptotic contributions to the integral coming from the endpoints of the integration interval (the beginning and the end of the laser pulse). In the case of an ultrashort pulse, the manipulation of these terms proves to be of great importance for calculating physical quantities.

E.2.2 Boundary terms

The existence of boundary terms comes from the fact that in theory the laser pulse is represented as having a finite temporal duration, while in reality the laser pulse is very slowly turned on and off such that the boundary effects, if present, should be negligible. In actual calculations, including the boundary terms can affect the results (such as energy spectrum of ejected electrons) by introducing spurious oscillations, which cannot be physically correct.

There are two contributions to the amplitude of ionization: one comes from the boundaries of the integration interval and the second one comes from the vicinity of the saddle points [see Subsection (E.5.1) for an intuitive picture]. In view of the comments above, we make the ansatz that the physically correct result is given by the saddle point contribution only. To see that, we point out that in some cases the magnitude of the boundary contribution can be much bigger than the saddle contribution. The particular form of the boundary term can be responsible under such circumstances for an oscillatory pattern in the result, as we will prove in the following.

The boundary terms are given by a simple procedure (see [39], p.8), which consists of forcing an integration by parts after re-writing the integrand:

$$\begin{aligned} \int_a^b f(x) e^{iS(x)} dx &= \int_a^b dx \frac{f(x)}{iS'(x)} [e^{iS(x)}]' \\ &= \frac{f(x)}{iS'(x)} e^{iS(x)} \Big|_a^b - \int_a^b dx \left[\frac{f(x)}{iS'(x)} \right]' e^{iS(x)}. \end{aligned} \quad (\text{E.5})$$

The procedure can be repeated in order to obtain higher order boundary terms.

Our model integrals now read:

$$V = \sum_{n_s=1,2,\dots} \exp[iS(t_s)] \sqrt{\frac{2\pi i}{S''(t_s)}} + \frac{\exp[iS(t)]}{iS'(t)} \Big|_0^{T_p} + \dots \quad (\text{E.6})$$

and

$$L = \sum_{n_s=1,2,\dots} \pi i \frac{\exp[iS(t_s)]}{S''(t_s)} + \frac{\exp[iS(t)]}{iS'(t)^2} \Big|_0^{T_p} + \dots \quad (\text{E.7})$$

Let us analyze the boundary term for the (V) form of the integral [Eq. (E.6)]:

$$\frac{\exp[iS(T_p)]}{iS'(T_p)} - \frac{\exp[iS(0)]}{iS'(0)} = 2 \frac{\cos[S(T_p)/2]}{i(p^2/2 + I_p)} \exp[iS(T_p)/2].$$

We have assumed that the vector potential satisfies the condition $A(0) = A(T_p) = 0$.

One can see that the magnitude of this term decreases for higher electron energies, so the boundary terms are expected to be more influential in the low energy part of the electron spectra. The presence of the cosine factor will cause oscillations in the spectrum, with minima at electron energies given by the condition $S(\mathbf{p}, T_p) = k\pi$, with k an integer number. It is interesting to note that for the case of a stationary field, this condition is automatically fulfilled, as it is nothing else but the condition of conservation of energy for the ejected electron. Actually, it can be shown that because of the energy conservation, the boundary terms are zero to *all* orders.

As an example, we show in Fig. E.1 the differential ionization probability in the laser polarization direction. The differential ionization probability is defined

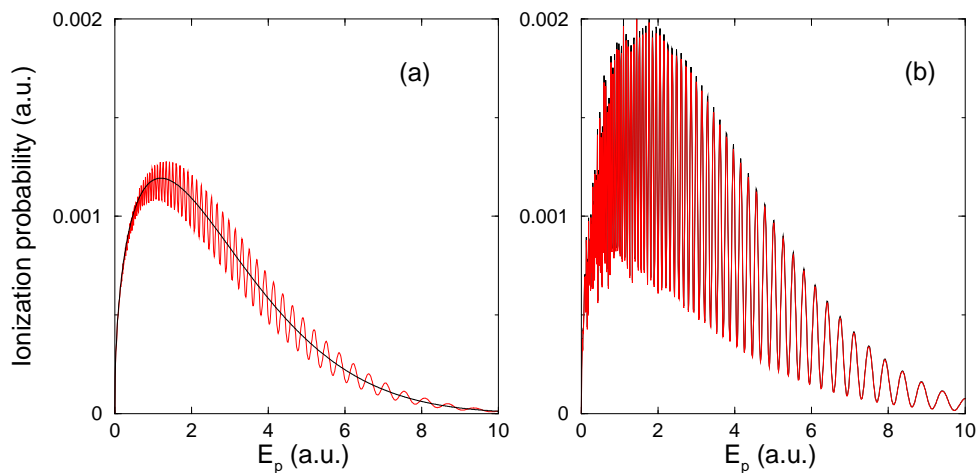


Figure E.1: Angle-resolved ATI energy spectrum generated by a 2-cycle \sin^2 pulse (left panel) and a 4-cycle one (right panel) with zero absolute phase, $\lambda=800$ nm and intensity $I = 5 \times 10^{15}$ W/cm² in He⁺. The electron is emitted along the laser polarization direction. Panel (a): the smooth curve (black) represents the saddle point result and the oscillating curve (red) the exact calculation from which the first order boundary term contribution has been subtracted. Panel (b): the two results are almost indistinguishable on the scale of the graph.

as:

$$w = \frac{|M_p|^2 d^3 \mathbf{P}}{d\Omega_p dE_p} = p |M_p|^2. \quad (\text{E.8})$$

The amplitude of ionization M_p is calculated with the Krainov Coulomb corrected formula and the absolute phase is defined as the carrier-envelope relative phase for the laser pulse. In panel (a), the difference between the smooth saddle result and the exact one from which the first order boundary contribution has been subtracted [see Eq. (E.6)] is attenuated at high electron energies due to next order boundary terms. According to our ansatz, these contributions have to be further subtracted from the integral in order to get correct predictions for the physical quantities of interest.

In panel (b), the same results are shown for a 4-cycle pulse. Because the pulse is longer, the higher order boundary terms become negligible and the agreement with the saddle calculation is very good. The oscillations in panel (b) are physical characteristics of the electron spectra, while in panel (a), the

oscillations in the red curve are due solely to the interference pattern coming from boundary terms, which is un-physical as explained at the beginning of this section.

In general, the next order boundary terms depend on the electric field and its derivatives. Thus, the boundary contribution will be negligible for sufficiently smooth vanishing electric fields at the beginning and the end of the pulse or for very long pulses.

E.2.3 Comparison with exact results

If the asymptotic expansion is straightforward to obtain for the velocity gauge form [Eq. (E.2)], it is more difficult for the length gauge form [Eq. (E.1)] because the saddle points are also poles of the integrand. Nonetheless, the corresponding asymptotic formula can be found in the literature (see [105], p.308, Problem 7.12 and for the general case of algebraic singularity Section 9.4 in the same book). A simple way of deducing the leading asymptotic contribution in such cases is given by Gribakin and Kuchiev [68].

Comparing the exact numerical results to the results obtained by using the saddle method, good agreement is obtained for regular saddle points as seen in panel (b) of Fig. E.1. For the case of singular saddle points, showed in Fig. E.2, the agreement is good qualitatively. However, the results differ by apparently a constant factor.

The overall agreement is good and given that the saddle point method is fast, it allows for satisfactory qualitative and quantitative predictions, especially when calculating the total ionization probabilities, which require a large number of integrals to be evaluated.

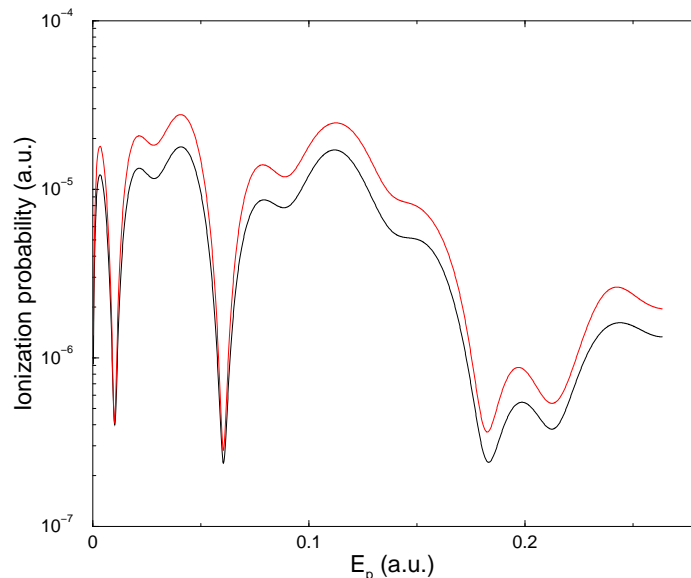


Figure E.2: Angle-resolved ATI energy spectrum calculated in the length gauge, generated by a 4-cycle \sin^2 pulse with zero absolute phase, $\lambda=800$ nm and intensity $I = 6 \times 10^{13}$ W/cm² in krypton ($I_p = 14$ eV). The electron is emitted along the laser polarization direction. The lower (black) curve shows the saddle results and the upper (red) curve shows the exact results.

E.3 Finding the saddle points

E.3.1 General considerations

The principal difficulty when applying the saddle point method is to find the saddle points, which means that one has to solve the nonlinear equation:

$$\frac{dS(t_s)}{dt} \equiv \frac{[p_{\parallel} + A(t_s)]^2}{2} + \left(\frac{p_{\perp}^2}{2} + I_p \right) = 0. \quad (\text{E.9})$$

For physical reasons, we look for solutions t_s with the real part in the temporal interval of the pulse ($0 < \text{Re}(t_s) < T_p$).

Because the equation has real coefficients, its solutions come in complex conjugate pairs. Only one solution of the pair contributes to the integral, as the exponential might ‘explode’ in some of them. As we ask for these integrals at a series of increasing electron momenta, the calculation could use a good initial guess for the saddle points (for example at $\mathbf{p} = 0$) and then increase p_{\parallel}

and p_{\perp} by a small step, using the values of t_s obtained at each step as guesses for the next step.

To calculate this solution numerically, one needs a good initial guess which is then refined by a specialized subroutine, until convergence is achieved, provided the two roots are sufficiently separated in the complex plane. If the solutions are close, the routine might get ‘confused’ when trying to converge to one of the roots. To avoid this, in practice we factorize the equation (E.9) and calculate the solutions for only one of the following factors:

$$\left(p_{\parallel} + A(t_s) + i\sqrt{p_{\perp}^2 + 2I_p}\right) \left(p_{\parallel} + A(t_s) - i\sqrt{p_{\perp}^2 + 2I_p}\right) = 0. \quad (\text{E.10})$$

The solutions for either of the factors in Eq. (E.10) can have both positive and negative imaginary parts. As it will be shown later, the relevant solution is the one with positive imaginary part.

E.3.2 Approximate saddle points

An approximate solution for the saddle times can be obtained by making use of the Simpleman’s model, where the approximate ‘birth time’ t_0 of the electron is obtained by solving the equation $p_{\parallel} + A(t_0) = 0$, numerically.

To find the saddle point close to t_0 , we choose to write the first terms of a Taylor expansion for (E.9) around t_0 and obtain

$$\frac{dS(t_s)}{dt} = I_p + \frac{p_{\perp}^2}{2} + \frac{E(t_0)^2}{2}(t_s - t_0)^2 = 0, \quad (\text{E.11})$$

from which it follows a pair of solutions :

$$t_s - t_0 = \pm i \frac{\sqrt{2I_p + p_{\perp}^2}}{|E(t_0)|}. \quad (\text{E.12})$$

The approximation is good only if the electric field is not zero at $t = t_0$ and if the transversal momentum p_{\perp} is small compared to the ionization potential I_p . In practice, we ask that $|E(t_0)| \geq 0.5 \max[E(t)]$. Knowing the position of

the saddle point and the Taylor expansion of the action first order derivative, we can approximate the action at the saddle point

$$S(t_s) = S(t_0) + \int_{t_0}^{t_s} dt \frac{dS(t)}{dt}$$

and its derivatives as

$$S(t_s) = S(t_0) + i \frac{1}{3} \frac{(2I_p + p_\perp^2)^{3/2}}{|E(t_0)|}, \quad (\text{E.13a})$$

$$S''(t_s) = i(2I_p + p_\perp^2)^{1/2} |E(t_0)|, \quad (\text{E.13b})$$

$$S'''(t_s) = E(t_0)^2, \quad (\text{E.13c})$$

where the saddle point with positive imaginary part was used. From here we see that using the solution with negative imaginary part would make $\exp[iS(t_s)]$ ‘explode’ because the exponent is positive.

In conclusion, we can find approximate solutions to the saddle equation, close to the real times t_0 . Using only the approximate saddles gives rise to a simplified version of the saddle point method, allowing for good qualitative calculations.

To summarize, we present an easier version of the saddle point method that doesn’t require finding the exact saddle points in the complex plane, but uses an approximate expression [see (E.12)]. The method follows the steps below:

- Find real solutions for the equation $p_\parallel + A(t_0) = 0$, such that $|E(t_0)| \geq 0.5 \max |E(t)|$. The solutions exist only if $|p_\parallel|$ is at most equal to the amplitude of the magnetic vector potential. This implies that we can only describe the spectrum up to a certain (high) electron energy.
- Write the model integrals (without the boundary terms) as

$$L = \sum_{n_0=1,2,\dots} \frac{\pi \exp[iS(t_0)]}{(2I_p + p_\perp^2)^{1/2} |E(t_0)|} \exp \left[- \frac{1}{3} \frac{(2I_p + p_\perp^2)^{3/2}}{|E(t_0)|} \right] \quad (\text{E.14})$$

and

$$V = \sum_{n_0=1,2,\dots} \frac{\sqrt{2\pi} \exp[iS(t_0)]}{\sqrt{(2I_p + p_\perp^2)^{1/2} |E(t_0)|}} \exp \left[-\frac{1}{3} \frac{(2I_p + p_\perp^2)^{3/2}}{|E(t_0)|} \right]. \quad (\text{E.15})$$

This simplified version of the saddle point method has the advantage that it doesn't require the exact saddle points, which makes it easy to implement as described above. One should note that the saddle points are estimated by using a simple quadratic expansion around the birth times of the electron.

The error of the estimates has to be as low as possible as they appear in the exponent in the saddle point formula. It turns out that the quadratic estimates give a fairly accurate result in the range of low electron energies for which the imaginary parts of the saddle points are small [the low energy electrons tunnel out when the laser electric field is close to the maximum, thus the imaginary part of the saddle solutions is small, see Eq. (E.12)]. An example is given in Fig. E.3.

The departure of the simplified saddle results from the saddle point estimate increases with electron energy. The difference is both in magnitude and relative phase. Higher order estimates of the saddle points [see Eq. (E.11) for a quadratic estimate] would improve the result, but the extra difficulties may not justify their use over the full saddle method.

E.3.3 Exact saddle points

For finding the exact saddles, one needs to find all the solutions for the non-linear equation (E.9) or for one of the factorized branches (E.10) in a finite region of the complex plane. Such a problem has been addressed intensively in the literature of numerical methods and in the case of only one unknown, algorithms are available to isolate the roots in a certain interval and then use a Newton-like method to refine the solution.

A reliable method is discussed in [106] and it is based on the property that the

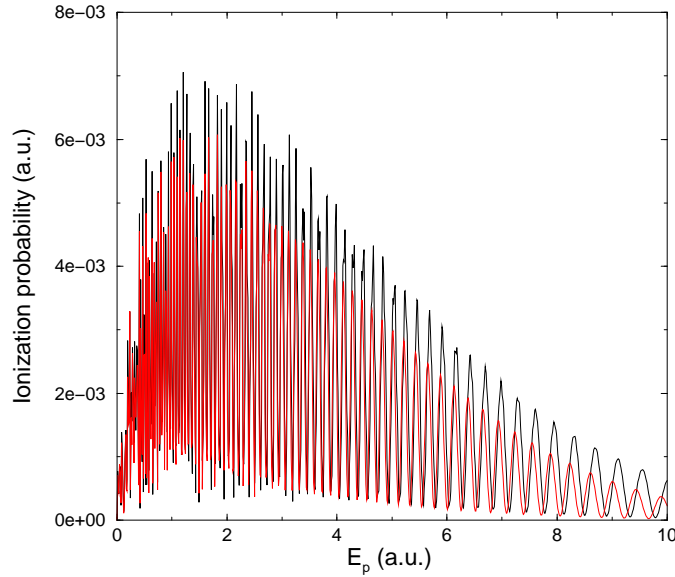


Figure E.3: Angle-resolved ATI energy spectrum calculated by using the Krainov Coulomb corrected ionization amplitude, generated by a 4-cycle \sin^2 pulse with zero absolute phase, $\lambda=800$ nm and intensity $I = 5.6 \times 10^{15}$ W/cm² in He⁺. The electron is emitted along the laser polarization direction. The upper (black) curve shows the saddle results and the lower (red) curve shows the saddle simplified version results.

integral $1/(2\pi) \oint dz f'(z)/f(z)$ on a contour encircling the region of interest is equal to the number of zeros (including multiplicities) of $f(z)$ interior to the contour considered. Then the contour is divided in smaller regions, containing only one root. The algorithm gives all roots in the region considered.

A more direct approach to find the saddle points is to use the Mathematica package [77] and its `ContourPlot` command. For example

$$\text{ContourPlot}[\text{Log}[\text{Abs}[\frac{dS(\mathbf{p}=0, x+Iy)}{dt}]]], \{x, 0, T_p\}, \{y, 0, 5\}],$$

which draws a density plot of the absolute value of the action derivative for all times with the real part in the interval when the pulse is acting and the imaginary part chosen such that the saddle points would become visible (the ‘Log’ function is used to increase contrast). An example is shown in Fig. E.4 for a 4-cycle laser pulse with wavelength of 800 nm described by the magnetic vector potential with zero phase $\mathbf{A}(t) = \mathbf{E}_0/\omega \sin t \sin^2(t/8)$ interacting with a He⁺ ion. The saddle points can now be read directly from the graph.

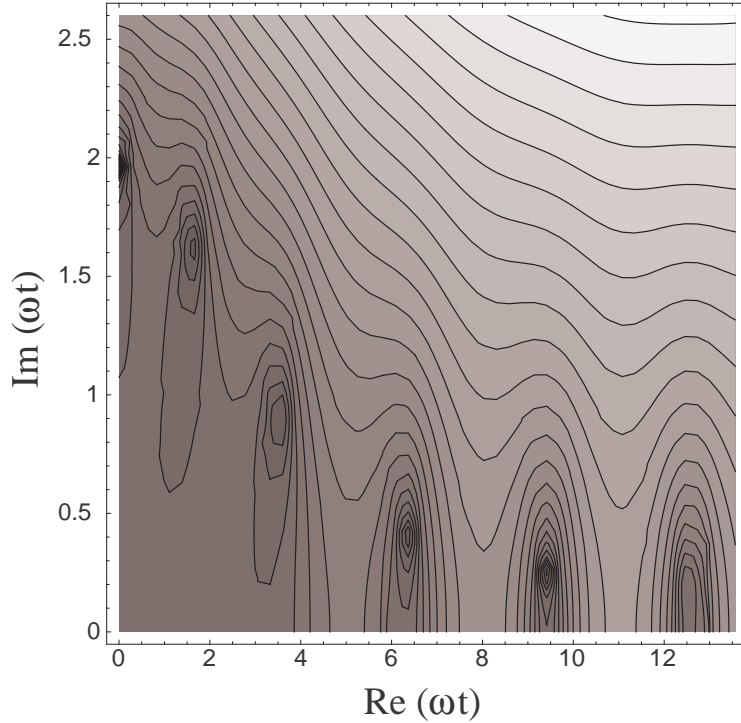


Figure E.4: Some of the saddle points for the case of a He^+ ion irradiated by a 4-cycle laser, at an intensity of 10^{16} W/cm² and wavelength 800 nm. The laser pulse is described by a \sin^2 envelope with zero absolute phase.

One other possibility is to start with the birth times t_0 from the Simpleman's model (the solutions of $p_{\parallel} + A(t_0) = 0$) and then use them as guesses for either equation in (E.10). The solution is propagated while increasing the imaginary term from zero up to the actual value in small steps. One has to be careful not to choose a step so large that the solution at the next step would depart too much from the solution at the previous step and the numerical routine would not be able to find it. We found that a suitable step is $|E(t_0)|/20$. As the contribution of a certain birth time t_0 to the integral depends exponentially on the electric field magnitude $|E(t_0)|$ [see Eqs. (E.15) or (E.14) where the electric field is present in the exponential], only those points with non-negligible electric field should be considered (i.e., in practice we use the condition $|E(t_0)| \geq 0.6E_0$).

E.4 Improved saddle point method - the high intensity case

It is expected that with increasing intensity, and therefore with increasing action (roughly in proportion to both the laser intensity and the temporal length of the pulse), the saddle point method would give more accurate results. Unfortunately, this is not the case. The reason for this is revealed by analyzing the behaviour of the exponential, when crossing the saddle point along the saddle axis and taking into account the third order derivative of the action at the saddle point (remember that only the quadratic variation is included when deducing the saddle point formula).

The model integral looks like

$$\int dx \exp\left(-\frac{a}{2}x^2 + i\frac{b}{6}x^3\right) \quad \text{with } a < 0, \text{Im}(b) = 0. \quad (\text{E.16})$$

Following the simple version of the saddle point method, we can estimate the values of $a = [d^2S(t_s)/dt^2]/i$ and $b = d^3S(t_s)/dt^3$ from (E.13b) and (E.13c):

$$a = (2I_p + p_\perp^2)^{1/2}|E(t_0)| \quad (\text{E.17a})$$

$$b = E(t_0)^2. \quad (\text{E.17b})$$

Therefore, with increasing electric field, the third derivative increases, causing oscillations in the quadratic decaying of the exponential (see Fig. E.4). This makes the gaussian integral representing the saddle point formula ineffective and to account for the oscillations we need to treat the cubic term explicitly. Fortunately, this can be done analytically using the Airy function:

$$\int_{-\infty}^{\infty} dx \exp\left(-\frac{a}{2}x^2 + i\frac{b}{6}x^3\right) = 2^{4/3}\sqrt{\pi}/b^{1/3} \exp\left(\frac{a^3}{3b^2}\right) \text{Ai}\left(\frac{a^2}{2^{2/3}b^{4/3}}\right) \quad (\text{E.18})$$

A more accurate way to define the range of applicability of the usual saddle point formula is to follow the general techniques from the asymptotic theory. Namely, for the usual saddle formula to be valid, the magnitude of the cubic term has to be much smaller than that of the quadratic term, within the range

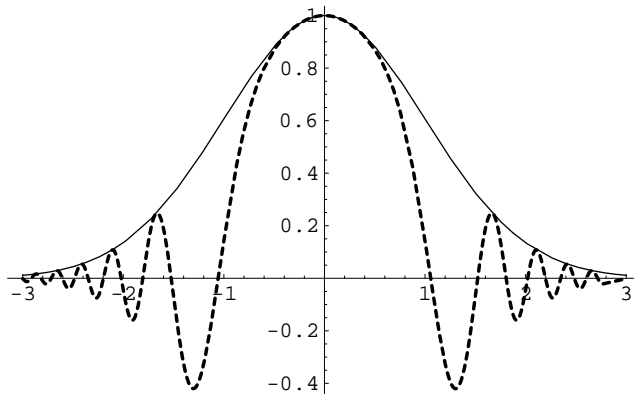


Figure E.5: Exponential decay (gaussian) and gaussian with cubic oscillatory factor [see (E.18)].

of the saddle point. With the coefficients of the quadratic and cubic terms approximated by (E.17), we arrive at the condition:

$$E_0 \ll \frac{9}{2}Z^3, \quad (\text{E.19})$$

with E_0 the amplitude of the electric field. The condition of validity found in [107] for a stationary field, but using exact expressions for the derivatives a and b , is $E_0 \ll 9Z^3$.

The formula (E.18) can be used with a , b either given by (E.17) in the simpler version of the saddle point method or with a and b calculated by using the exact second and third derivative of the action at the saddle point. Then, we simply replace the term $\sqrt{2\pi i/S''(t_s)}$ from the classical saddle point formula by the expression given in (E.18). This is to be used in integrals of the form (E.2), when no singularity is present. For the integrals of type (E.1), a similar formula can be written but it involves more complicated functions.

This issue has been also addressed by Ortner and Rylyuk in [108]. Contrary to what we found, these authors concluded that the approach described above wouldn't work. The reason given is that integrals containing cubic terms would be divergent anywhere in the complex plane. As seen from the simple version of the saddle method, the coefficient of the cubic term [see Eq. (E.17b)] in this approximation is real, meaning that the contribution of the cubic term to the

integrand is purely oscillatory and therefore poses no difficulties. The exact value of the cubic coefficient (obtained by taking the third derivative of the action at the exact saddle point) has a very small imaginary part which makes the calculation presented here still possible, with no divergence, even for the full saddle point method where the exact saddle points are used.

As an example, we analyze the error made by using the standard saddle point method in the case of a He^+ ion irradiated by a 800 nm, 4-cycle laser pulse, at an intensity of $8.8 \times 10^{15} \text{ W/cm}^2$ for detachment in the direction of polarization.

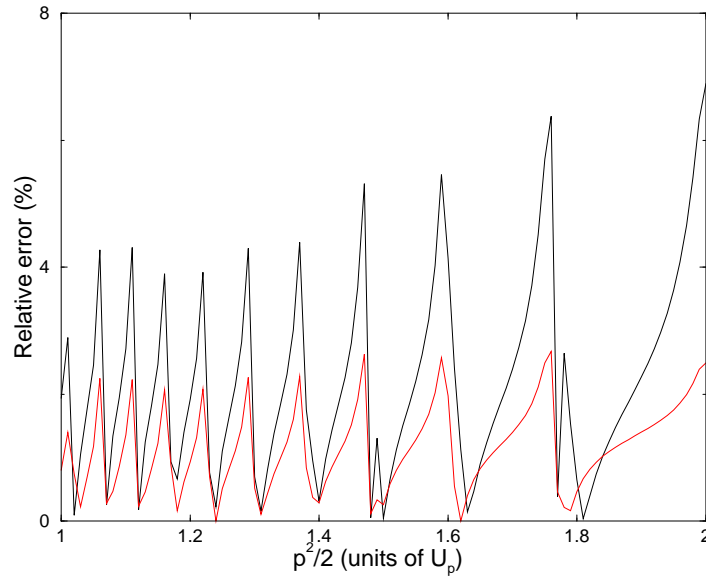


Figure E.6: The relative error of the differential ionization probability for emission along the polarization direction, in the case of a He^+ ion irradiated by a 800 nm, 4-cycle laser pulse, at an intensity of $8.8 \times 10^{15} \text{ W/cm}^2$ and zero absolute phase. The black curve shows the error made by using the usual saddle method and the red curve shows the resulting error when using the improved saddle method.

We found that the relative error in the high energy region of the spectrum close to cutoff is of the order of 6% with an increasing trend, while for the improved saddle method, the relative error is 2% and doesn't increase with increasing electron energy.

Because the effect of the cubic term increases with intensity of the external field, making the usual saddle formula inapplicable, the advantage of the im-

proved saddle method is that it extends the domain of applicability for the usual saddle point method to higher values of the laser intensity.

E.5 Numerical integration

In order to directly integrate (E.1) and (E.2), special methods have to be used due to the highly oscillatory nature of the integrand. Classical methods such as Gauss quadratures or the Simpson method converge, but at the cost of a large number of sample points required to resolve the oscillations, which make them time consuming and thus inefficient. An exact calculation can also be useful for assessing the validity of the saddle approximation.

We propose two methods: one is based on integration in the complex plane, using the properties of the saddle points and the second one uses a novel technique recently developed in the literature. They are comparable in performance and, although slightly slower, the latter is simpler and more general as it doesn't require to calculate the saddle points of the integrand.

E.5.1 Method I - using the saddle points

A fast method can use the basic ideas of the saddle method, namely that the integrand decreases exponentially in the vicinity of the saddle points. This requires the knowledge of the positions of the saddle points, which presents no difficulty as shown in the previous section. Once they are calculated, we choose the one with the lowest (positive) imaginary part and instead of integrating along the real axis, we deform the contour as presented in Fig. E.7.

To illustrate the advantage of the method, we show in Fig. E.8 the real part of the integrand as in the Krainov Coulomb corrected amplitude [see Eq. (E.2)], for the same parameters as in Fig. E.4, but for an intensity $I = 5 \times 10^{15}$ W/cm² and emission along the laser polarization direction. The energy of the emitted electron is $0.2U_p$. The letters define the path in the complex plane, as pictured

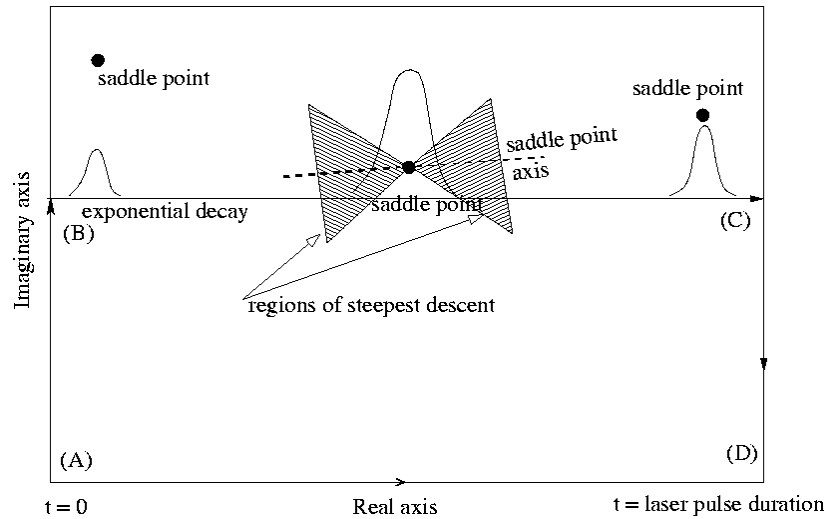


Figure E.7: The deformation of the integration contour in the complex plane to avoid strong oscillatory behaviour along the real axis. The full curves represent the exponential decay of the integrand in the vicinity of the saddle points.

in Fig. E.7. The exponential decrease in the vicinity of the end points (A) and (D) is related to the boundary term contribution [see Subsection E.2.2]. In our particular case, their magnitude is much higher than the contribution of the saddle points (red curve). The peaks on the red curve are located near the saddle points and their height is in proportion to how close the saddle points are to the integration path (BC).

The upper panel shows the real part of the integrand along the real axis. We choose to show only one tenth of real axis, otherwise it is difficult to see the details due to rapid oscillations.

It now becomes easy to integrate the function, as the oscillatory behaviour has been changed to an exponential decay.

The way the integration contour must cross the lowest saddle point is related to the directions of the steepest descent (pictured in Fig. E.7) and steepest ascent axes (the paths on which the absolute value of the integrand decreases respectively increases exponentially). The integration contour must be chosen such as to be as close as possible to the steepest descent path which can be

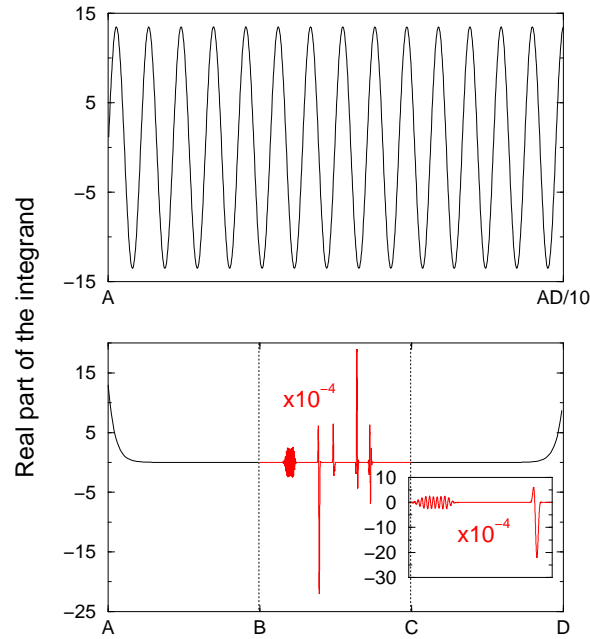


Figure E.8: The integrand behaviour in the complex plane (lower panel) and along the real axis (upper panel). The letters correspond to the integration path in Fig. E.7. For simplicity, only a part of the real axis has been represented. The inset in the lower panel shows the integrand along the beginning of the BC path.

approximated with the axis of the saddle point. The latter contains all x such that $\text{Re}\left[i\frac{S''(t_s)}{2}(x - t_s)^2\right] \leq 0$ (for more details see [109], p.84). For all cases of interest this has been found to be almost parallel to the real axis, so that the integration path can go through the saddle point parallel to the real axis, as shown in figure. For the case of the integral (E.1), the height of the contour is chosen smaller than the imaginary part of the saddle point closest to the real axis, because of the singularity. For practical purposes, a value of $0.9 \text{Im}(t_s)$ was taken.

E.5.2 Method II - integration along real axis

The second method is based on an approach proposed by Levin [110] and further developed by Evans and Webster [111].

Levin's idea is to write

$$\int f(x)e^{iq(x)}dx = y(x)\exp[iq(x)]. \quad (\text{E.20})$$

By differentiating the equation he obtains a differential equation for the unknown function $y(x)$. Levin shows that there is a solution to this equation which is not oscillatory and he solves it by using collocation method with a non-oscillatory function basis (polynomials) in order to eliminate the (other) oscillatory solution. To get more precision, more and more functions have to be used and the method becomes unstable (the linear system to be solved becomes ill-conditioned). Evans and Webster improved the method by using Chebyshev polynomials to form the collocation basis set, and the problem is no longer ill-conditioned. But for long integration intervals, it becomes more and more time demanding to solve linear systems of equations with a large number of variables due to a larger number of basis functions.

To avoid those difficulties, we adapted their method by writing a recursive procedure which in practice is fast and reliable. Our method uses a small number of Chebyshev polynomials (between 10 and 20) to reduce the dimensions for the linear system to be solved. It begins by calculating the integral for a given interval with the initial function basis (containing for example the first 15 Chebyshev polynomials) and then re-calculates it by adding to the basis the next order polynomial. If the accuracy test is passed, the routine picks the next interval to analyze, if not, the current interval is divided in half and it begins again with each of them, until the whole integration interval is covered.

The novelty of the algorithm consists in devising a suitable strategy to integrate an oscillatory function over a long interval. For such intervals, just by increasing the polynomial base as suggested by the authors, although numerically stable and convergent, the execution time increases beyond practical use. In our method, the number of polynomials is kept as low as possible to the exchange of dividing the integration interval in manageable parts.

When applied to our model integrals, the integration time is considerably

smaller compared to an integration using the trapezoidal method and a high accuracy can be achieved. This way, it can be applied successfully to deal with similar integrals, as encountered in atomic physics.

E.6 Conclusions

We analyzed ways to calculate the ionization amplitudes within the SFA. The most direct approach that is suitable given the characteristic of the problem at hand (strongly oscillatory behaviour of the integrand) is the saddle point method which gives relatively accurate numerical results for a reasonably short computational time. It only requires an efficient way to calculate the complex saddle points. Methods to do that were presented along with an easier version of the saddle point method which avoids using the exact saddle points in exchange of slightly less accuracy but still in good qualitative agreement with the exact calculation. The simplified version has the advantage that it is straightforward to implement and allows for a quick evaluation of the results which then can be further studied by using the full saddle point method or the exact integration.

For high intensities, we found that the saddle method gives less good agreement, contrary to what one could expect. We proposed a modified version of the saddle point formula, which takes into account the third order derivative, responsible for the poorer results given by the usual saddle method and checked this assumptions in practical cases, obtaining good agreement in spite of the high intensities used in calculation.

We also found that it is possible to perform the exact integration either by deforming the integration contour such as to go through a vicinity of the saddle point closest to the real axis, though taking advantage of the exponential decay of the integrand in that region or by using a special method based on Chebyshev collocation (Evans and Webster method). For the collocation case, we used the basic algorithm proposed by Evans and Webster and adapted it to

successfully deal with SFA model integrals for which the collocation method is not practical because of long integration intervals. We propose a recursive version of it which with reasonable accuracy requirements can be as fast or even faster than the method of changing the integration path.

In practice, to calculate angle integrated ionization probabilities or rates, a large number of such integrals have to be calculated, so the saddle point method gives the best computational time for such a task. The exact methods can be used to compare in certain cases the approximate results to the exact ones.

Bibliography

- [1] D B Milošević, S X Hu, and W Becker. *Phys. Rev. A*, 63:011403R, 2001.
- [2] M J Nandor, M A Walker, L D Van Woerkom, and H G Muller. *Phys. Rev. A*, 60, 1999.
- [3] B Piraux, personal communication.
- [4] A de Bohan, B Piraux, L Ponce, R Taïeb, V Véniard, and A Maquet. *Physical Review Letters*, 89(11):113002, 2002.
- [5] T Brabec and F Krausz. *Rev. Mod. Phys.*, 72:545, 2000.
- [6] D J Jones, S A Diddams, J K Ranka, A Stentz, R S Windeler, J L Hall, and S T Cundiff. *Science*, 288(5466):635, 2000.
- [7] A Baltuška, Takao Fuji, and Takayoshi Kobayashi. *Phys. Rev. Lett.*, 88:133901 (1–4), 2002.
- [8] S T Cundiff. *J. Phys. D*, 35:R43, 2002.
- [9] P Salières, A L’Huillier, P Antoine, and M Lewenstein. *Advances in Atomic, Molecular and Optical Physics*, 41:83, 1999.
- [10] P M Paul, E S Toma, P Berger, G Mullot, F Augé, P Balcou, H G Muller, and P Agostini. *Science*, 292(5522):1689, 2001.
- [11] P Salières, B Carré, L Le Déroff, F Grasbon, G G Paulus, H Walther, R Kopold, W Becker, D B Milošević, A Sanpera, and M Lewenstein. *Science*, 292(5518):902, 2001.

-
- [12] R A Bartels, A Paul, H Green, H C Kapteyn, M M Murnane, S Backus, I P Christov, Y Liu, D Attwood, and C Jacobsen. *Science*, 297(5580):376, 2002.
- [13] J L Krause, K J Schafer, and K C Kulander. *Phys. Rev. Lett.*, 68:3535, 1992.
- [14] K C Kulander and K J Schafer. In D K Evans, editor, *Proc. Int. Conf. Multi Photon Processes VI*. World Scientific, Singapore, 1993.
- [15] P B Corkum. *Phys. Rev. Lett.*, 71:1994, 1993.
- [16] M Lewenstein, P Balcou, M Y Ivanov, A L’Huillier, and P Corkum. *Phys. Rev. A*, 49:2117, 1994.
- [17] W Becker, S Long, and J K McIver. *Phys. Rev. A*, 50:1540, 1994.
- [18] M Y Kuchiev. *JETP Lett.*, 45:404, 1987.
- [19] N Milošević, A Scrinzi, and T Brabec. *Phys. Rev. Lett.*, 88:093905, 2002.
- [20] V D Taranukhin. *Laser Physics*, 10:330, 2000.
- [21] M W Walser, C H Keitel, A Scrinzi, and T Brabec. *Phys. Rev. Lett.*, 85:5082, 2000.
- [22] N J Kylstra, R M Potvliege, and C J Joachain. Photon emission by ions interacting with short intense laser pulses: beyond the dipole approximation. *J. Phys. B: At. Mol. Opt. Phys.*, 34:L55–L61, February 2001.
- [23] V D Taranukhin and N Y Shubin. *Quantum Electron.*, 31:179, 2001.
- [24] D B Milošević, S X Hu, and W Becker. *Laser Physics*, 12:389, 2002.
- [25] N J Kylstra, R M Potvliege, and C J Joachain. *Laser Physics*, 12:409, 2002.

- [26] A Baltuška, T Udem, M Uiberacker, M Hentschel, E Goulielmakis, C Gohle, R Holzwarth, A Scrinzi V S Yakovlev, T W Hänsch, and F Krausz. *Nature*, 421:611, 2003.
- [27] E Cormier and P Lambropoulos. *Eur. Phys. J. D*, 2:15, 1998.
- [28] I P Christov. *Opt. Lett.*, 24:1425, 1999.
- [29] P Dietrich, F Krausz, and P B Corkum. *Opt. Lett.*, 25:16, 2000.
- [30] S Chelkowski and A D Bandrauk. *Phys. Rev. A*, 65:061802(R)(1–4), 2002.
- [31] G G Paulus, F Grasbon, H Walther, P Villorresi, M Nisoli, S Stagira, E Priori, and S De Silvestri. *Nature*, 414:182, 2001.
- [32] D B Milošević, G G Paulus, and W Becker. *Phys. Rev. Lett.*, 89:153001, 2002.
- [33] D B Milošević, G G Paulus, and W Becker. *Laser Physics*, 13:948, 2003.
- [34] D B Milošević, G G Paulus, and W Becker. *Optics Express*, 11:1418, 2003.
- [35] R Reichle, H Helm, and I Y Kiyan. *Phys. Rev. Lett.*, 87(24):243001, 2001.
- [36] D B Milošević, A G Busuladžić, and W Becker. *Phys. Rev. A*, 68(5):050702, 2003.
- [37] M V Ammosov, D B Delone, and V P Krainov. *Sov. Phys. JETP*, 64:1191, 1986.
- [38] D B Milošević. In B Piraux and K Rzażewski, editors, *Super-Intense Laser-Atom Physics*, page 229. Kluwer Academic, Dordrecht, 2001.
- [39] V A Borovikov. *Uniform stationary phase method*. The Institution of Electric Engineers, 1994.

-
- [40] M Y Ivanov, T Brabec, and N Burnett. *Phys. Rev. A*, 54:742, 1996.
- [41] R M Potvliege, N J Kylstra, and C J Joachain. *J. Phys. B: At. Mol. Opt. Phys.*, 33:L743, 2000.
- [42] K J Schafer and K J Kulander. *Phys. Rev. Lett.*, 78:638, 1997.
- [43] D Gabor. *J. IEEE*, 93:429, 1946.
- [44] P B Corkum, N H Burnett, and M Y Ivanov. *Opt. Lett.*, 19:1870, 1994.
- [45] M Dammasch, M Dörr, U Eichmann, E Lenz, and W Sandner. *Phys. Rev. A*, 64:061402(R), 2001.
- [46] C C Chirilă, C J Joachain, N J Kylstra, and R M Potvliege. *Laser Physics*, 14:190, 2004.
- [47] M Protopapas, C H Keitel, and P L Knight. *Rep. Prog. Phys.*, 60:389, 1997.
- [48] C J Joachain, M Dörr, and N J Kylstra. *Advances in Atomic and Molecular Physics*, 42:225, 2000.
- [49] W Becker, F Grasbon, R Kopold, D B Milošević, G G Paulus, and H Walther. *Advances in Atomic, Molecular, and Optical Physics*, 48:35, 2002.
- [50] G S Voronov and N B Delone. *JETP Letters*, 1:66, 1965.
- [51] F Fabre, G Petite, P Agostini, and M Clement. *J. Phys. B: At. Mol. Opt. Phys.*, 15:1353, 1982.
- [52] G Petite, F Fabre, P Agostini, M Crance, and M Aymar. *Phys. Rev. A*, 29:2677, 1984.
- [53] P Agostini, F Fabre, G Mainfray, G Petite, and N Rahman. *Phys. Rev. Lett.*, 42:1127, 1979.

- [54] B Young, K J Schafer, B Walker, K C Kulander, P Agostini, and L F Di Mauro. *Phys. Rev. Lett.*, 71:3770, 1993.
- [55] D Feldmann. In D K Evans, editor, *Proc. Int. Conf. Multiphoton Processes VI*. World Scientific, Singapore, 1993.
- [56] G G Paulus, W Nicklich, H Xu, P Lambropoulos, and H Walther. *Europhys. Lett.*, 27:267, 1994.
- [57] M Lewenstein, K C Kulander, K J Schafer, and P H Bucksbaum. *Phys. Rev. A*, 51:1495, 1995.
- [58] G G Paulus, W Nicklich, H Xu, P Lambropoulos, and H Walther. *Phys. Rev. Lett.*, 72:2851, 1994.
- [59] H B van Linden van den Heuvell and H G Muller. *Multiphoton Processes, Studies in Modern Optics*, 8:25, 1988. Cambridge.
- [60] T F Gallagher and T J Scholz. *Phys. Rev. A*, 40:2762, 1989.
- [61] D M Volkov. *Z. Phys.*, 94:250, 1935.
- [62] L V Keldysh. *Zh. Éksp. Teor. Fiz.*, 47:1945, 1964. [Sov. Phys. JETP 20:1307, 1965].
- [63] F H M Faisal. *J. Phys. B: At. Mol. Opt. Phys.*, 6, 1993.
- [64] H R Reiss. *Phys. Rev. A*, 22:1786, 1980.
- [65] C Figueira de Morisson Faria, H Schomerus, and W Becker. *Phys. Rev. A*, 66:043413, 2002.
- [66] P Dietrich, F Krausz, and P B Corkum. *Opt. Lett.*, 25:16, 2000.
- [67] N B Delone and V P Krainov. *J. Opt. Soc. Am. B*, 8:1207, 1991.
- [68] G F Gribakin and M Yu Kuchiev. *Phys. Rev. A*, 55:3760, 1997.
- [69] A Lohr, M Kleber, and W Becker. *Phys. Rev. A*, 55, 1997.

- [70] D B Milošević and F Ehlotzky. *Phys. Rev. A*, 57:5002, 1998.
- [71] D B Milošević and F Ehlotzky. *Phys. Rev. A*, 58:3124, 1998.
- [72] S P Goreslavskii and S V Popruzhenko. *Phys. Lett. A*, 249:477, 1998.
- [73] S P Goreslavskii and S V Popruzhenko. *J. Phys. B: At. Mol. Opt. Phys.*, 32, 1999.
- [74] S P Goreslavskii and S V Popruzhenko. *Journal of Experimental and Theoretical Physics*, 90:778, 2000.
- [75] G G Paulus, W Becker, W Nicklich, and H Walther. *J. Phys. B: At. Mol. Opt. Phys.*, 27, 1994.
- [76] R Kopold, W Becker, and M Kleber. *Optics Communications*, 179:39, 2000.
- [77] Stephen Wolfram. *The Mathematica Book, Fourth Edition*. Wolfram Media, Cambridge University Press, 1999.
- [78] D B Milošević and W Becker. *Phys. Rev. A*, 66:063417, 2002.
- [79] R Kopold and W Becker. Quantum paths in above-threshold ionization for elliptical polarization. In L F DiMauro, R R Freeman, and K C Kulander, editors, *Multiphoton Processes: ICOMP VIII, 8th International Conference*, volume 525, page 11. American Institute of Physics Conference Proceedings, 2000.
- [80] G G Paulus, F Grasbon, A Dreischuh, and H Walther. In L F DiMauro, R R Freeman, and K C Kulander, editors, *Multiphoton Processes: ICOMP VIII, 8th International Conference*, volume 525, page 24. American Institute of Physics Conference Proceedings, 2000.
- [81] C Figueira de Morisson Faria, M Dörr, W Becker, and W Sandner. *Phys. Rev. A*, 60:1377, 1999.

- [82] U Mohideen, M H Sher, H W K Tom, G D Aumiller, O R Wood, II, R R Freeman, J Boker, and P H Bucksbaum. *Phys. Rev. Lett.*, 71:509, 1993.
- [83] B Walker, B Sheehy, L F DiMauro, P Agostini, K J Schafer, and K C Kulander. *Phys. Rev. Lett.*, 73:1227, 1994.
- [84] B Walker, B Sheehy, K C Kulander, and L F DiMauro. *Phys. Rev. Lett.*, 77:5031, 1996.
- [85] V P Krainov. *J. Opt. Soc. Am. B*, 14:425, 1997.
- [86] P Antoine, A L'Huillier, M Lewenstein, P Salières, and B Carré. *Phys. Rev. A*, 53:1725, 1996.
- [87] A Becker, L Plaja, P Moreno, M Nurhuda, and F H M Faisal. *Phys. Rev. A*, 64:023408, 2001.
- [88] H S Antunes Neto and L Davidovich. *Phys. Rev. Lett.*, 23:2238, 1984.
- [89] A M Perelomov and V S Popov. *Sov. Phys. JETP*, 25:336, 1967.
- [90] M V Ammosov, N B Delone, and V P Krainov. *JETP*, 64:1191, 1986.
- [91] F A Ilkov, J E Decker, and S L Chin. *Laser Physics*, 3:298, 1993.
- [92] H R Reiss. *Phys. Rev. A*, 65:055405, 2002.
- [93] R Shakeshaft, R M Potvliege, M Dörr, and W E Cooke. Multiphoton processes in an intense laser field. iv. the static-field limit. *Phys. Rev. A*, 42:1656, 1990.
- [94] A de Bohan, P Antoine, D B Milošević, and B Piraux. *Phys. Rev. Lett.*, 81:1837, 1998.
- [95] A de Bohan, P Antoine, D B Milošević, GL Kamta, and B Piraux. *Laser Physics*, 9:175, 1999.
- [96] A M Perelomov, V S Popov, and V P Kuznetsov. *Sov. Phys. JETP*, 27:451, 1968.

-
- [97] P H Bucksbaum, M Bashkansky, and D W Schumacher. *Phys. Rev. A*, 37:3615, 1988.
- [98] S Chelkowski and A D Bandrauk. *Phys. Rev. A*, 65:061802(R), 2002.
- [99] S Chelkowski, A D Bandrauk, and A Apolonski. *Optics Letters*, 29:1557, 2004.
- [100] J Bergou and S Varró. *J. Phys. A: Math. Gen.*, 13:3553, 1980.
- [101] Kai Drühl and J K McIver. *J. Math. Phys.*, 24:705, 1983.
- [102] W Gordon. *Z. Phys.*, 40:117, 1926.
- [103] H R Reiss and V P Krainov. *J. Phys. A: Math. Gen.*, 36:5575, 2003.
- [104] P B Corkum, N H Burnett, and F. Brunel. *Phys. Rev. Lett.*, 62:1259, 1989.
- [105] Norman Bleistein and Richard A Handelsman. *Asymptotic expansions of integrals*. Dover Publications, Inc., New York, 1986.
- [106] P Kravanja, M Van Barel, O Ragos, M N Vrahatis, and F A Zafiroopoulos. Zeal: A mathematical software package for computing zeros of analytic functions. *Comput. Phys. Comm.*, 124:212, 2000.
- [107] H S Brandi, L Davidovich, and N Zagury. *Phys. Rev. A*, 24:2044, 1981.
- [108] J Ortner and V M Rylyuk. *J. Phys. B: At. Mol. Opt. Phys.*, 34:3251, 2001.
- [109] N G de Bruijn. *Asymptotic Methods in Analysis*. Dover Publications, Inc., New York, 1981.
- [110] D Levin. *Mathematics of Computation*, 38:531, 1982.
- [111] G A Evans and J R Webster. *Applied Numerical Mathematics*, 23:205, 1997.